

Investigation of functionalized graphene, hexagonal boron nitride and their hybrids from first principles and mean-field Hubbard model in search of controlled magnetism and chemical activation

By

Rita Maji

PHYS11201204014

National Institute of Science Education and Research

Jatni, Odisha - 752050, India

A thesis submitted to the

Board of Studies in Physical Sciences

In partial fulfillment of requirements

for the Degree of

DOCTOR OF PHILOSOPHY

of

HOMI BHABHA NATIONAL INSTITUTE

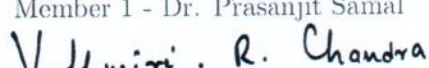


July, 2019

Homi Bhabha National Institute

Recommendations of the Viva Voce Committee

As members of the Viva Voce Committee, we certify that we have read the dissertation prepared by **Rita Maji** entitled **“Investigation of functionalized graphene, hexagonal boron nitride and their hybrids from first principles and mean-field Hubbard model in search of controlled magnetism and chemical activation”** and recommend that it may be accepted as fulfilling the thesis requirement for the award of Degree of Doctor of Philosophy.

Chairman - Prof. Bedangadas Mohanty		Date 5/7/2019
Guide / Convener - Dr. Joydeep Bhattacharjee		Date 05/07/2019
 External Examiner - Prof. Priya Mahadevan		Date 5-7-19
 Member 1 - Dr. Prasanjit Samal		Date 5-7-19
 Member 2 - Dr. V. Ravi Chandra		Date 5-7-2019
 External Member - Prof. Saroj Kumar Nayak		Date 5-7-2019

Final approval and acceptance of this thesis is contingent upon the candidate's submission of the final copies of the thesis to HBNI.

I hereby certify that I have read this thesis prepared under my direction and recommend that it may be accepted as fulfilling the thesis requirement.

Date: 05/07/19
Place: NISER.


Dr. Joydeep Bhattacharjee

STATEMENT BY AUTHOR

This dissertation has been submitted in partial fulfillment of requirements for an advanced degree at Homi Bhabha National Institute (HBNI) and is deposited in the Library to be made available to borrowers under rules of the HBNI.

Brief quotations from this dissertation are allowable without special permission, provided that accurate acknowledgement of source is made. Requests for permission for extended quotation from or reproduction of this manuscript in whole or in part may be granted by the Competent Authority of HBNI when in his or her judgment the proposed use of the material is in the interests of scholarship. In all other instances, however, permission must be obtained from the author.

Rita Maji
Rita Maji

DECLARATION

I, Rita Maji, hereby declare that the investigation presented in the thesis has been carried out by me. The work is original and has not been submitted earlier as a whole or in part for a degree/diploma at this or any other Institution/University.

Rita Maji
Rita Maji

List of publications arising from the thesis

Journal

Published

1. Bias induced ferromagnetism and half-metallicity in graphene nano-ribbons, Rita Maji, Joydeep Bhattacharjee, Scientific Reports **7**, Article number: 17094 (2017).
2. Hybrid superlattices of graphene and hexagonal boron nitride: A ferromagnetic semiconductor at room temperature, Rita Maji, Joydeep Bhattacharjee, Phys. Rev. B **99**, 125409, (2019).

Accepted

1. A Synergistic View of Magnetism, Chemical Activation, and ORR as Well as OER Catalysis of Carbon Doped Hexagonal Boron Nitride from First-Principles, Rita Maji and Joydeep Bhattacharjee, J. Phys. Chem. C 2019. (<https://doi.org/10.1021/acs.jpcc.9b03229>).

Communicated

1. Quantitative estimation of chemical activation from first principles and model Hamiltonian demonstrated in hybrid structures of graphene and hexagonal boron nitride, Rita Maji and Joydeep Bhattacharjee.

Under preparation

1. Catalytic activity of multi-boron doped Graphene from First-principle, Rita Maji, Joydeep Bhattacharjee.

2. Reduction of NO_x ($x=1,2$) through hydrogenation, a new route in graphene and h-BN based substrate ($\text{B}_x\text{C}_y\text{N}_z$). Rita Maji, Joydeep Bhattacharjee.
3. Manipulating space charge towards new realms in spintronics, Rita Maji, Joydeep Bhattacharjee.
4. Electrically induced magnetism in 2D bipartite lattices, Rita Maji, Joydeep Bhattacharjee.

Symposium and conference

1. “Electronic structure and magnetism in gated armchair graphene nanoribbon”, Rita Maji, Joydeep Bhattacharjee, Indo-Japan Workshop on Magnetism at Nanoscale (IJWMN-2015), 09-12 January 2015, NISER, Bhubaneswar, India.
2. “Electronic structure and magnetism in partially gated graphene nanoribbon”, Rita Maji, Joydeep Bhattacharjee, APS March meeting 2016, 14-18 March 2016, Baltimore, MD (United States).
3. “Room temperature ferromagnetism in carbon doped hexagonal boron-nitride”, Rita Maji, Joydeep Bhattacharjee, Annual Condensed Matter Physics Meeting, 26-27th February, 2018, NISER, Bhubaneswar and Institute of Physics, Bhubaneswar, India.

School and Discussion meeting

1. “Strongly correlated systems: From models to materials”, 6-17th January, 2014, International Center for Theoretical Sciences (ICTS) at the Indian Institute of Science, Bangalore, India.

2. "MASTANI: Summer School on MAterials Simulation Theory And NumerIcs",
30th June-12th July, 2014 , Jointly Abdus Salam International Center for Theoretical Physics, Italy & IISER Pune, India.

Rita Maji
Name and signature
of the student -

*Dedicated
to
My Mother*

Acknowledgements

Here I would like to acknowledge all those peoples who have supported me in several ways, without which the completion of the doctoral dissertation might not be possible.

First and foremost, I would like to express my sincere gratitude to my supervisor Dr. Joydeep Bhattacharjee for the unfailing support, unending encouragement and unfathomable patience throughout my doctoral project. I am deeply grateful to Dr. Bhattacharjee for the numerous helpful discussions and valuable suggestions I had at each and every step of my Ph.D. life. Being the first doctoral student of him, I had the privilege of learning most of the basic tools directly from him. I wholeheartedly thank him for giving me the opportunity to work with him.

I express my special thanks to the faculty of School of Physical Sciences, NISER, who taught me in pre-doctoral coursework and afterward giving me the opportunity to attend various courses, which were and will be really helpful in my research career. I would like to thank the HPC support team of NISER for their endless and generous help, particularly in emergency situations, which helped me a lot in computational works throughout my Ph.D. I am also grateful to my doctoral committee members for the valuable comments and suggestions during annual reviews.

I would also like to thank some of my close friends for their endless support, motivational words, and faith on me, which really boosted my confidence in my distressed moments. I am also thankful to my lab members for their personal and professional support.

All my teachers at various stages of my academic life supported me a lot with their valuable guidance, as a result of which I have reached this stage. I am indebted to all of them for their blessings and good wishes.

Finally, I would like to thank my lovely parents, my brother, my little princes Pihu and all other family members for the consistent support and unconditional love.

As a special thanks in this acknowledgment, I am truly delighted to mention my mother Mrs. Rekha Maji, who is eagerly waiting to see this achievement come true, only due to whose persistent encouragement and firm belief that I am here today.

Rita Maji

July, 2019

Contents

Synopsis	xxv
List of Abbreviations	xxiv
List of Figures	xxv
1 Introduction	1
1.1 Thesis outline	4
2 Calculation of Electronic structures	10
2.1 Introduction	10
2.2 Single particle approximation	11
2.2.1 Hartree & Hartree Fock	12
2.2.2 Overview of density functional theory	14
2.2.2.1 Exchange and Correlation	17
2.2.2.2 Pseudopotential Method	19
2.2.3 Computation based on DFT	21
2.2.3.1 Phonon calculation	22
2.2.3.2 Van der Waals correction	24
2.3 Simple models for electronic structure	26
2.3.1 Electrons in periodic potential	27

2.3.2	Tight-Binding model	28
2.3.3	Description of interacting electrons : second quantization	30
2.3.3.1	Second quantized description of electrons in periodic potential	32
2.3.3.2	Two body interaction	33
2.3.4	Hubbard Model	34
2.3.4.1	Mean Field approximation	36
2.3.4.2	Self-consistent approach	38
2.4	Wannier Function	39
2.4.1	Wannier function from Kohn-Sham basis	42
2.4.1.1	Isolated system	43
2.4.1.2	Periodic system	45
3	Electronic and magnetic properties of 2p-block elements in low dimension	51
3.1	Introduction	51
3.1.1	Graphene	52
3.1.2	Graphene Nanoribbon	54
3.2	p-electron driven magnetism in graphenic systems	55
3.2.1	Ferromagnetism in bipartite system	57
4	Partial Bias Induced Magnetism	62
4.1	Introduction	62
4.2	Inhomogeneous bias on graphene nanoribbon	63
4.2.1	Inhomogeneously biased armchair graphene nanoribbon	64
4.2.1.1	Indirect band gap	65

4.2.1.2	Metallic phases	66
4.2.2	Inhomogeneously biased zigzag graphene nanoribbon	67
4.2.3	First principles calculation for zigzag graphene	
	nanoribbon	71
4.2.4	Mechanism & analysis with minimal model	72
4.2.4.1	Nearest neighbor FM order in simple model	73
4.3	Possible experimental realization	79
5	Magnetism in graphene-hexagonal boron nitride hybrids	83
5.1	Introduction	83
5.2	Calculation details	85
5.2.1	Estimation of mean-field parameters	85
5.3	Interaction between magnetic graphene islands in hBN	87
5.3.1	Isolated pair of graphene islands	88
5.3.2	Honeycomb super-lattice of C4 islands	89
5.3.3	Mechanism of mediation of magnetic ordering	90
5.3.3.1	Microscopic model	92
5.3.3.2	Switching of anti-ferromagnetic to ferromagnetic order	93
5.4	Ferromagnetic ordering in honeycomb-Kagome double-lattice	94
5.4.1	Different phases due to ferromagnetic ordering	96
5.4.2	Confirmation with improved exchange-correlation functional	99
5.5	Hybrid super-lattices with bigger graphene island	100
5.6	Effect of additional hBN layer	103
5.7	Possible experimental realization	104
6	Electrocatalysis with hybrid layers made of 2p-block elements	108
6.1	Introduction	108

6.2 Calculation details	110
6.2.1 Bond order calculation	111
6.3 Carbon doped hexagonal boron nitride	114
6.3.1 Energetics of substitution	115
6.3.2 Chemical activation	116
6.3.2.1 Average bond order(ABO) as a measure of activation	118
6.3.2.2 Activation as a function of electronegativity	120
6.3.2.3 Correlation between chemical activation and magnetism	
	120
6.3.2.4 Orbital view of chemical activation	123
6.3.3 Catalytic activity	127
6.3.3.1 Adsorption of O₂	127
6.3.3.2 Oxygen Reduction Reaction(ORR)	130
6.3.3.3 Oxygen Evolution Reaction(OER)	133
6.3.3.4 Non-magnetic graphene island	135
6.3.4 Transferability of electrons	137
Conclusions	142
Future Scope	145



Homi Bhabha National Institute

SYNOPSIS OF Ph. D THESIS

1. **Name of the student** : Rita Maji
2. **Name of the Constituent Institution** : National Institute of Science Education and Research
3. **Enrolment No.** : PHYS11201204014
4. **Title of the Thesis** : Investigation of functionalized graphene, hexagonal boron nitride and their hybrids from first principles and mean-field Hubbard model in search of controlled magnetism and chemical activation.
5. **Board of Studies** : Physical Sciences

SYNOPSIS

Before the isolation of graphene in 2004^[1], it was long believed that 2D materials are thermodynamically unstable unless grown on a suitable substrate. The perception changed in 2004, followed by a great surge in interest in not only graphene but also in a variety of 2D materials which emerged in quick succession, like single layer of hexagonal boron-nitride(hBN), MoS₂, WS₂, g-C₃N₄ etc.^[2] New physics in these systems are rooted at the confinement of electron in one of the degrees of freedom, leading to an additional layer of quantization and increased level of correlation among electrons due to localization, which led to substantial enrichment of their electronic structure^[3]. Study of quantum phenomena in reduced dimension has thus led to a new direction of research, which is often referred as mesoscopic physics, where the

interplay of electron-electron interactions, events of scattering and confinement manifests many exotic phenomena[3]. However, it is not only rich physics, but also great promises of their application in devices, which have fuelled interest in these materials for almost last two decades, and still going strong, in fact stronger, with the advent of new promises. Historically almost, one key promise which fuelled interest in graphene is the high mobility of electrons in it, which is rooted at the linear dispersion of its $2p_z$ electrons at Fermi energy, and has long been perceived as an answer to the problem of increased Joule heating due to reduction in cross-section of electrical contacts in devices of shrinking size. It was also anticipated that, not only passive contacts, but also active elements like diodes and transistors[4, 5] could be made of tailored graphene and graphene-hBN hybrids, as a substitute to silicon. In more recent years, they have been shown sustain ferro-magnetism at room temperature[6] upon appropriate functionalization, which has opened up a new direction in pursuit of magnetic materials, which are lighter and thinner than those made of metals, have large spin relaxation time due to small spin-orbit coupling compared to the metals, and yet magnetically as well as structurally stable at room temperature. Such atomically thin magnetic layer will be ideal for use in high density integration of data storage and reading units. In the series of 2D materials proposed and synthesized, the lightest ones are made of the elements of the 2p-block, namely, boron(B), carbon(c) and nitrogen(N), constituting graphene, hexagonal boron nitride(hBN) and their hybrids[7, 8], which show remarkable structural resilience on account of the strong covalent bonds made by the sp^2 hybridized orbitals of B, C and N. Electronic structure of valence electrons of these bipartite systems are determined primarily by their $2p_z$ electrons which are exposed to competition between (A): inter-sub-lattice delocalization, which reduces kinetic energy, (B): inter-sub-lattice spin separation, which reduces Coulomb potential energy of occupied orbitals, and (C): localization due to inhomogeneous

distribution of electron-negativity or applied bias, both of which determines the on-site term (orbital energy) in a tight-binding(TB) framework. In pristine graphene A wins over B to result into a non-magnetic semi-metallic ground state. However, their electronic structure can be tuned from their inherent semi-metallic nature to semiconducting as well as metallic, by cutting them into ribbons or rolling them into tubes in different directions. Magnetism in these half-filled bipartite systems can be attributed to such scenarios of functionalization[9] which impacts the two sub-lattices unequally, so that the increased kinetic energy due to impeded inter-sub-lattice hopping, allows lowering of total energy through inter-sub-lattice spin separation in the vicinity of functionalization. The sub-lattices thus become ferri-magnetically(FeM) ordered, leading to a net non-zero magnetic moment associated with the functionalization. hBN on the other hands is an insulator, as the difference in electronegativity of the two sub-lattices opens up a gap about Fermi energy. Thus in a graphene-hBN hybrids the properties of the localized $2p_z$ electrons at the graphene-hBN interface remain largely unaltered by the bulk hBN.

In this thesis, we have investigated inhomogeneously biased graphene ribbons as an example of reversible physical functionalization, and graphene-hBN hybrids, which can also be described as C doped hBN, implying chemical functionalization. We anticipated new physics as well as their possible applications in some of the contemporary problems in materials science. Through calculation of electronic structure from first principles[10, 11] and mean-field Hubbard model[12], we have revealed new properties and proposed new materials, broadly in two classes of studies and applications, one belongs to a group of the correlation driven interplay of charge and spin degrees of freedom for application involving switchable magnetism at nanoscale, while the other set of problems are mainly based on chemical activation due to chemical inhomogeneity and thus relevant of catalysis. Studies of magnetism and chemical

activation in these there coordinated systems are synergistic, since the same set of electrons which localize to render magnetic moment, also leads to chemical activation due to their unpaired nature which undermines completeness of sub-shell filling of their host carbon atom.

In my first work, we have tried to explore deep into the relation between localization and formation of local moment. Upon chemical functionalization or at defects, localization of the $2p_z$ electron due to lack of scope of coordination, constitutes a local moment. We asked whether there exists a critical level of localization, as possible due to external bias which is incorporated as an on-site term in a tight-binding framework, at which spin separation can occur irrespective of lack of coordination. We find that indeed localization due to inhomogeneous biasing can exclusively result into spin separation between biased and unbiased region. Within mean-field Hubbard model, results suggest bias driven robust evolution of pristine graphene nano-ribbons into a ferromagnetic semiconductor, metal or a half metal, irrespective of their edge configurations. Further analysis proposed that such evolution is a result of ferromagnetic(FM) ordering at nearest neighboring(n-n) sites[13] in positively biased regions. The trend on the onset of the n-n FM order[13] is more enhanced if the biased region is narrow and located nearer to the ribbon edges. In zig-zag graphene nano-ribbon(ZGNR) the onset of the n-n FM order contests the inherent AFM ordering[9] between the two zigzag edges and turns it to FM leading to net nonzero magnetic moment. These consequences of inhomogeneous biasing have been confirmed[13] from first principles calculation. Analysis suggests that, the onset of n-n FM order can be understood as an attempt to cooperatively minimize the on-site Coulomb repulsion and the kinetic energy, while favoring the maximum localization of electrons at the positively biased sites. Such cooperative mechanism has been verified through semi-analytical model in simpler systems[13] which also establishes the n-n FM order to

be a general property of inhomogeneously biased bipartite systems.

Magnetic moment in islands of graphene arises due to unequal coverage of the two sub-lattices, [14]. Large moments are possible from triangular graphene chunk since all its zigzag edges are in one sublattice. On the other hand, substitution by C in hBN is known to form patches of graphene in hBN, and preferred shape of such patches are known to be triangular or like ribbons [15, 16]. Magnetic graphene islands embedded in hBN is thus an experimentally accessible scenario. Motivated by recent experimental observation of room temperature ferromagnetism in C doped hBN [17], we have undertaken a systematic study of super-lattices of triangular carbon-islands embedded in the hBN matrix [18]. It is reported [19] that magnetic carbon island embedded in hBN in proximity favor anti-ferromagnetic (AFM) coupling, although the mechanism was yet to be fully understood. Accordingly, we began this work with deriving an atomically resolved understanding of the mechanism of -B-N- mediated AFM ordering between magnetic carbon islands, and subsequently proposed possibilities to switch to FM ordering and stabilize a non-zero magnetic moment. Spin-resolved first principles calculation and orbital(p_z) resolved Wannier analysis [20] both shows a spatial spin separation of back transferred electrons at N and B as the source of the AFM ordering between islands [18]. Such spin separation also implied spin dependent hopping, which we find to be a necessary criteria for emergence of the AFM order in the ground state, within the mean-field approximation of Hubbard model. The AFM ordering switch to FM order in presence of another local moment on or in the vicinity of the -B-N- pathway connecting two magnetic islands. With such local moment, which can be due to an isolated substitution or another magnetic islands, the system essentially becomes an interpenetrating hexagonal-Kagome double super-lattice. The Kagome lattice determines the strength of FM ordering in the hexagonal lattice and the consequent degree of ferromagnetic semiconductor or half-metallic nature [18]. Effective

strength of the exchange interaction suggests that the ferromagnetic semiconducting phase may sustain at room temperature.

Since localization of electrons also plays an important role in its chemical activation, 2D materials has become a good platform in various electrocatalytic processes[21]. Among them, carbon doped hBN has been reported as an efficient catalyst towards oxygen reduction reaction [22] which is the key process in an acid based fuel-cell. Since substitution by C leads to patches of graphene in hBN, and the degree of activation of C atoms in patches are different than that of an isolated C atom due to a single substitution, we set out to draw a comprehensive map of activation of C atoms substituted in hBN, in order to be able to find the suitable sites for efficient catalysis, which requires calibrated activation of sites. As a measure of the level of activation of carbon atoms in patches, we calculate the average of the bond orders of the three in-plane bonds around each atom in the three coordinated networks, and identify the quantity as the “average bond order (ABO)” around the atom. We calculate ABO from the bond orders obtained by projecting the effective TB electronic structure on bonding and anti-bonding states. Reduction in ABOs for C atoms in the island from their bulk value in graphene, present a comparative picture of activation in agreement with results from first principles. Difference of ABOs before and after an event of adsorption, estimated within a TB set up where the on-site term reflect electronegativity, appears to provide a more detailed picture of activation specific to the adsorbed atom. With increasing patch size, ABOs indicate that the activation of C at B site moderates to desired levels for optimal catalysis, whereas the activation of C at N site reduces below the desired levels. Thus, in contrast to isolated C atoms or smaller patches, bigger patches covering more B sites will be more suitable for optimum ORR catalysis, which is also convenient in terms of availability of active sites, since, patches covering more B atoms are energetically more favorable compared to

their counterparts covering more N site.

In summary, we have studied functionalized graphene, hBN and their hybrids from first principles and mean-field model, to explore possible routes to spin polarized localization of electrons which leads to magnetism as well as chemical activation and catalysis. We have proposed the possibility of bias induced localization of spin, amounting to n-n FM order, as a general property of inhomogeneously biased bipartite system, accompanied by spin polarized transport. In another work we have shown how FM order can be established between magnetic graphene islands in hBN to render FM semiconductor at room temperature. We next show that these magnetic islands are also chemically active and are potentially good candidate for catalysis relevant to fuel-cells. With this we hope that the work presented in this thesis will brighten and sharpen the focus on inhomogeneous three coordinated networks as a versatile material for contemporary and future applications.

Bibliography

- [1] K. S. Novoselov *et al.*, *Science* 306, 666, **(2004)**.
- [2] Sheneve Z. Butler *et al.*, *ACS Nano*, 7 (4), 2898-2926, **(2013)**.
- [3] Michael R. Geller, arXiv:cond-mat/0106256.
- [4] Gianluca Fiori *et al.*, *Nature Nanotechnology* 9, 768-779, **(2014)**.
- [5] Matthew J. Allen, Vincent C. Tung and Richard B. Kaner, *Chem. Rev.*, 110(1), 132-145, **(2010)**.
- [6] Yan Wang *et al.*, *Nano Lett.*, 9 (1), 220-224, **(2009)**.
- [7] A. H. Castro Neto, F. Guinea, N. M. R. Peres, K. S. Novoselov, & A. K. Geim, *Rev. Mod. Phys.* 81, 109, **(2009)**.
- [8] L. Song, H. Ci, P.B. Sorokin, J. Jin, A.G. Kvashnin, J. Kvashnin, B.I. Yakobson, P.M. Ajayan, *Nano Lett.*, 10(8), 3209-3215, **(2010)**.
- [9] O. V. Yazyev, *Reports on Progress in Physics* 73, 056501, **(2010)**.
- [10] W. Kohn, L. J. Sham, *Physical Review*. 140(4A), A1133-A1138, **(1965)**.
- [11] P. Giannozzi, S. Baroni, N. Bonini, M. Calandra, R. Car, C. Cavazzoni, D. Ceresoli, G., L. Chiarotti, M. Cococcioni, I. Dabo, *et al.*, *J. Phys. Cond. Mat.* 21, 395502(1-20), **(2009)**.

- [12] V. Bach, E. H. Lieb, J. P. Solovej, *Journal of Statistical Physics*. 76: 3, (1994).
- [13] Rita Maji & Joydeep Bhattacharjee, *Scientific Reports* 7, Article number: 17094, (2017).
- [14] E. H. Lieb, *Phys. Rev. Lett.* 62, 1201, (1989).
- [15] Zheng Liu *et al.*, *Nature Nanotechnology* 8, 119-124, (2013).
- [16] X. Wei, M.-S. Wang, Y. Bando, D. Golberg, *ACS Nano*, 5, 2916-2922, (2011).
- [17] Chong Zhao *et al.*, *Adv. Funct. Mater.* 24, 5985-5992, (2014).
- [18] Rita Maji & Joydeep Bhattacharjee, Hybrid super-lattices of graphene and hexagonal boron nitride: Ferromagnetism with non-metals at room temperature(submitted).
- [19] Ashwin Ramasubramaniam, Doron Naveh, *Phys. Rev. B* 84, 075405, (2011).
- [20] J. Bhattacharjee, U. V. Waghmare, *Phys. rev. B(R)* 73, 121102(1-4), (2006).
- [21] Dehui Deng, K. S. Novoselov, Qiang Fu, Nanfeng Zheng, Zhongqun Tian & Xinhe Bao, *Nature Nanotechnology*, 11, 218-230, (2016).
- [22] J. Zhao, Z. Chen, *J. Phys. Chem. C*, 119(47), 26348-26354, (2015).

List of Abbreviations

<i>2D</i>	Two Dimensional
<i>BZ</i>	Brillouin zone
<i>KS</i>	Kohn-Sham
<i>VDW</i>	Van der Waals
<i>ZGNRs</i>	Zig-zag graphene nanoribbons
<i>AGNRs</i>	Armchair graphene nanoribbons
<i>DFT</i>	Density Functional Theory
<i>hBN</i>	hexagonal Boron Nitride
<i>C</i>	Carbon
<i>B</i>	Boron
<i>N</i>	Nitrogen
<i>Gr – patch/island</i>	Graphene-patch/Graphene-island
<i>WFs</i>	Wannier Functions
<i>WCs</i>	Wannier Centers
<i>ORR</i>	Oxygen Reduction Reaction
<i>OER</i>	Oxygen Evolution Reaction
<i>n – n</i>	nearest neighbour

List of Figures

1.1	Representation of two atom basis primitive cell(dotted line) of graphene and hexagonal boron nitride. Few representative in-plane hybrids with graphene and hexagonal boron nitride.	3
2.1	Schematic representation of Hohenberg-Kohn(left) and Kohn-Sham(right) formalism. $E[n]$ is energy functional and $F_{HK}[n(r)]$ is H-K universal functional, variational minimization of which gives the exact ground state energy and density $n_0(r)$. $\psi_i(r)$ are fictitious K-S states including ground state wave function $\psi_0(r)$ and ground state density $n_0(r)$	15
2.2	Wave function(blue) in real Coulomb potential(blue) and representation of pseudopotential(red) and pseudo wave function(red)	20
2.3	Self consistent scheme for Kohn-Sham equations	21
2.4	self-consistent loop of DFPT for phonon mode calculation	24
2.5	Self consistent scheme for mean-field Hubbard model	38

2.6	Transformation from Bloch functions to WFs. Left: Real-space representation of three of the Bloch functions $e^{ikx}u_k(x)$ associated with a single band in one dimension, for three different values of the wave vector k . Filled circles indicate lattice vectors, and thin (green) lines the envelopes of each Bloch function. Right: WFs associated with the same band, forming periodic images of one another. The two sets of Bloch functions at every k in the Brillouin zone (BZ) and WFs at every lattice vector span the same Hilbert space. Image © Ref. [48]	41
2.7	Scheme of construction of Wannier function using K-S basis for (a) isolated system and (b) periodic system.	42
2.8	Wannier function using K-S basis for isolated system considering a hydrogen passivated finite system of (a) graphene, (b) hexagonal boron nitride and for periodic system representing (c) p_z atomic orbital and (d) bonding orbital for a planar p_z electron system. Big and small circles are equivalent to $2e^-$ and $1e^-$ respectively.	43
3.1	(a) Representation of bipartite Graphene with two sub-lattices A (filled circle) and B (hollow circle), real space basis vectors \vec{a}_1, \vec{a}_2 and the vectors $(\vec{\delta}_1, \vec{\delta}_2, \vec{\delta}_3)$ connecting nearest neighbor site. shaded region corresponds to primitive cell of bipartite lattice. (b) First Brillouin Zone with reciprocal lattice vectors \vec{a}_1^*, \vec{a}_2^* Dirac point K, K' and high symmetry k-point Γ and M. (c) Band structure of graphene using Eq. 3.4 with $t = -2.7$ eV.	53

3.2	(a)Representation of graphene nanoribbon for zigzag and armchair edges with periodic direction and unit cell as shown by solid and dotted rectangle respectively for ZGNR and AGNR. Band structure from TB model with various width of (b)AGNR for $N_A=5$ and $N_A=10$ and (d)ZGNR for $N_Z=4$ and $N_Z=8$. (e)Charge density for a selected region of $N_Z=8$. Band structure and density profile for HOMO and LUMO from mean-field Hubbard model for (c)AGNR for $N_A=10$, (f)ZGNR for $N_Z=6$	56
4.1	spin-correlation(positive & negative) plot as a function of U & V_g for different bias coverages: AGNR($N_A=6$)(a,b,c); AGNR($N_A=8$)(d,e,f). Here gray shade represents the bias coverage	65
4.2	Band structure and spin density(inset) from mean-field Hubbard model at $U=4.0$ eV for different gate voltages V_g with different bias coverage of AGNR: (a,b) $N_A=6$ and (c) $N_A=9$. Here gray shade represents the biased region	66
4.3	spin correlation(positive & negative) plot as a function of U and V_g with gate coverage of zigzag C-C bond for(a,b) $N_z = 9$, (c) $N_z = 8$. and with gate coverage of transverse C-C bond for(d,e) $N_z = 8$, (f) $N_z = 9$. unit-cell and bias coverage is shown here with solid line and gray shade respectively.	68
4.4	Band structure and spin density(inset) from mean-field Hubbard model for $U=4.0$ eV at different gate voltages V_g of ZGNR:(a,b) $N_z = 8$ with gate coverage of transverse C-C bond, and (c,d) $N_z = 9$ with gate coverage of zigzag C-C bond. unit-cell and bias coverage is shown here with a solid line and gray shade respectively.	69

4.5	For gated configuration of Fig.4.4(c), projected band structure corresponding to the edge sites with majority and minority spin both. This shows a clear evolution of band edges with the emergence of n-n and inter-edge FM ordering (spin density :inset).	70
4.6	Schematic band diagram(above) and spin density(below). The migration of electrons with spin-2(\downarrow)from edge-2 towards edge-1, owing to n-n FM order with spin-1(\uparrow) at biased region, C(V)BE : conduction(valence)band edge.	70
4.7	ZGNR in presence of sawtooth potential: (a) potential profile ; (b) band structure (above) & spin density(below). DFT results are qualitatively similar to their counterparts [Fig.4.4] based on mean-field Hubbard model.	71
4.8	(a)4-site model with n-n gate coverage. Bias site spin-correlation plot with (b)mean-field Hubbard model and (c)model Wannier function.	74
4.9	Density(up,down) and band structure of 4-site system[Fig.4.8(a)] from mean-field Hubbard model for $U=15.0$ eV with: (a,b) $V_g=10.0$ eV; (c,d) $V_g=15.0$ eV and (e,f) $V_g=20.0$ eV.	75
4.10	Different energy contributions for $U=15.0$ eV from : mean-field Hubbard model(a,c,e,g) & model WFs calculation(b,d,f,h). for a range of applied bias V_g to focus at three different regime : FEM, FM and NM along the dotted line of Fig.4.8(b,c).	76

4.11 (A)6.5 nm HfO₂ local back gate[Ref. 31], (B)a, Schematic view of a top-gated graphene r.f. transistor on DLC substrate. b, SEM image of a typical top-gated dual-channel r.f. device. Scale bar, 3μm. c, Cross-section TEM image of a graphene transistor with a gate length of 40nm. Scale bar, 40nm. d, SEM image of the 40-nm device. Scale bar, 400nm.[Ref. 30], (C) c. Electrostatic doping in graphene with P(VDF-TrFE) at the +Pr state. The green particles in graphene represent the initial p-type charged impurities doping, d.(c) Electrostatic doping in graphene with P(VDF-TrFE) at the +Pr state. The green particles in graphene represent the initial p-type charged impurities doping [Ref. 32], (D)a. Polar molecules at graphene edges in micrometer-scaled gated devices, Inset shows the two collectively aligned molecular configurations existing at graphene edges: above and below the graphene plane, b. SEM of one of our devices. Scale bar is 5 μm.[Ref. 33]

79

5.1 Density of states for pristine hexagonal boron nitride from(a) DFT and (b)MFH model. Projected density of states of the C-site for different C-substituted hBN from DFT and MFH calculation (c,d)1C@1N, (e,f)1B@1C, (g,h)C@N site for 3N1B island and (i,j)C@B site for 3B1N island respectively. Valence band edge has been adjusted to E=0 for better comparison in both cases. 86

5.2 For C4 island within a hydrogen passivated hBN chunk: (a)energy difference($E_{FM} - E_{AFM}$) for different island separation d (Inset: C4a island in hBN chunk for $d=0$ and the separation d) and spin density with single site separation($d=0$) for (b)C4a-N-C4a, (c)C4b-B-C4b. $E_{FM} - E_{AFM} > (<) 0$ favors AFM(FM) ordering. 88

5.3	LSDA Spin density of a pair of (a)C4a(3B1N) and (d) C4b(3N1B) as a part of a honeycomb super-lattices in hBN sheet are shown Planar projection of Wannier functions representing $2p_z$ orbital of C along (b) C-N and (e) C-B bonds for honeycomb super-lattices made of C4a and C4b islands respectively. Spin-resolved Wannier function of $2p_z$ orbital of (c)the bridging N atoms between C4b islands and (f) of the outer C atoms of the C4a islands connected through a B atom.	89
5.4	(a)Schematic representation of spin dependent hopping mechanism. Contour plot of total magnetization of the ground state calculated as a function of $(t-t')$ and onsite energy $E_{on-site}$ for a pair of (b)C4a(3B1N) and (c)C4b(3N1B) islands with $d = 0$ in a finite hBN segment at three different U values(2.0, 3.0 and 4.0) eV. For $U=4.0$ eV and $U=2.0$ eV the FM-AFM boundary is shown by black dotted line.	92
5.5	Schematic model of (a) AFM ordered C4a(3B1N) islands with spin dependent hopping. (b) Inherent AFM order between two local moment shown by C. (c) FM ordered C4a(3B1N) islands due to the extra local moment(C) at B site between the C4a islands. LSDA spin density plot of honeycomb super-lattice of C4a islands with $d = 1$ in (c) absence and (d) presence of C in the intermediate B sites. Wannier function representing the $2p_z$ orbitals of (e) the two N atoms back transferring to the C in the middle.	93
5.6	Wannier function representing the $2p_z$ orbitals of (e)the two N atoms back transferring to the C in the middle, and (f)of the C atom itself, in the -N-C-N- zigzag pathway between C4a islands.	94

5.7	(a) Representation of inter-penetrating C4a-X honeycomb-Kagome super-lattices for various intermediated substitution by C at X (B or N) sites for $d = 3$. Energy difference ($E_{FM}-E_{AFM}$) for different X with different separations of C4a islands,(b) $d=1$ (c) $d=2$ (d) $d=3$ and (e) $d=4$. $E_{FM}-E_{AFM} < 0$ implies FM order in honeycomb super-lattice.	96
5.8	Projected density of states of $2p_z$ orbital for some of the inequivalent atomic sites(shown in inset)for C4a honeycomb super-lattice with X at (a)0B and (b)3N location of Fig.5.7(a). The estimated coupling strength J is written in the inset.	97
5.9	Schematic DOS to understand the evolution with different choices of Gr-islands and X (a)C4a-X:N (b)C4a-X:B (c)C4b-X:N and (d)C4b-X:B for representative study.	98
5.10	Occupancy of spin due to $2p_z$ electrons at sites along the C-N-C-N-C zigzag path due -N-C-N- connectivity between C4a islands calculated using PBE, HSE and from MFH at $U=3.0$ eV and 6.0 eV.	99
5.11	Schematic presentation of C9(6B3N) islands(upper row) with different X-location and island separation d . This a part of full interpenetrating H-K super-lattices. Energy difference ($E_{FM}-E_{AFM}$) for different X with different separations of C9 islands, (a) $d=1$ (b) $d=2$ (c) $d=3$, $E_{FM}-E_{AFM} < 0$ implies FM order in honeycomb super-lattice.	101
5.12	(a)Spin density and spin polarized(b)DOS, (c)PDOS($2p_z$ only) for C9-X:B H-K super-lattice with Gr-island separation $d=3$. DOS for honeycomb super-lattice is shown in the inset of (b) and all the inequivalent atomic sites for PDOS plot shown in the inset of (c).	102

5.13 Spin density and spin-polarized DOS for hybrid super-lattice, consists of (a)3N1B(H); 3B1N(K), (b)3N1B(H); 3B1N(K), (c)6B3N(H); 3B1N(K), (d)6B3N(H); 3N1B(K), (e)7B6N(H); 3B1N(K) graphene islands at honeycomb(H) and Kagome(K) site respectively, (f)energy difference($E_{FM}-E_{AFM}$) and total magnetization of the lower energy configuration for all hybrid super-lattices as marked by a-e. $E_{FM}-E_{AFM} > (<)0$ corresponds to AFM(FM) ground state.	102
5.14 Energy difference($E_{FM}-E_{AFM}$) and total magnetization of the lower energy configuration for bilayer hybrid super-lattices as marked by 1-4 . $E_{FM}-E_{AFM} > (<)0$ corresponds to AFM(FM) ground state.	103
5.15 Bilayer hybrid super-lattices and spin density for (a,b)d=1 and (d,e)d=2 with d as mentioned in Fig.5.7, spin-polarized DOS with(2,4 of Fig.5.14) and without C(1,3 of Fig.5.14) at intermediate(Kagome) sites for (c)d=1 and (f)d=3. Red and blue line corresponds to 1 and 3 configuration of Fig.5.14, filled color represents the configuration 2 and 4 of Fig.5.14.	104

5.16 (A)(a) Schematic diagram of the patching growth. (b) SEM morphol-

ogy of hybridized domains. (c) XPS spectra of B, N, C 1s core levels.

(d,e)(VT = -0.002 V, IT = 23.00 nA; -0.011 V, 6.30 nA) Atomically

resolved STM images of pure h-BN and graphene on Rh(111), respec-

tively. (f)(-0.200 V, 33.30 nA) Zoomed-in STM image at the bound-

ary linking h-BN and graphene. (g) Cross-sectional profiles along L1

and L2 in (f)showing the apparent corrugations spanning over two

analogues.[Ref. 25], (B)(a) DFT calculations of the binding energies

(Eb) of graphene, h-BN, and BNC hybrids. (b) Two typical BNC

hybrids of BN@G and G@BN. (c) (VT = 0.800 V, IT = 0.02 nA)

Large-scale STM images showing the preferred linking of graphene to

preexisting h-BN domains. (d) (0.700 V, 0.02 nA) and (e) (0.400 V,

0.02 nA) Sequential zoomed-in of (c)[Ref. 25], (C)(a) Schematic illus-

tration of the temperature-triggered switching growth between in-plane

h-BN-G and stacked G/h-BN heterostructures, defined as Route 1 and

Route 2, respectively.(b)SEM image of a sample synthesized by Route

1, showing discrete hexagonal graphene islands embedded in h-BN.

(d)AFM height images of h-BN-G after being transferred onto 300-

nm-thick SiO2 substrates, with corresponding height histograms and

line sections shown in (f)The scale bars in d is 1[Ref. 28], (D)d-f, SEM

image, optical image and Raman mapping of a graphene/h-BN array of

circles, with graphene circles embedded in an h-BN matrix. Scale bars,

50 m (d), 50 m (e) and 10 m (f). g,h, SEM images of graphene/h-BN

stripes. Scale bars, 50 m (g) and 10 m (h).i, SEM image of graphene/h-

BN strip structure with graded strip dimensions, fabricated by FIB

etching of h-BN and subsequent graphene growth. The widths of each

strip, from top to bottom, are 1 μ m, 500 nm, 200 nm and 100 nm,

respectively. Scale bar, 1 μ m. [Ref. 11]

6.1	Average bond order(ABO) for isolated C-island starting from C=3 to C=33 atoms and graphene sheet. Color scheme represents a different order of sharing of electrons between the neighboring sites. The arrow shows the ABO variation from edge towards the middle(bulk) region.	113
6.2	Representative variety of configurations with substitution by carbon in hexagonal boron nitride.	114
6.3	Formation energy (per C atoms) of C substituted hBN configurations shown in Fig.6.2. The dashes and solid arrows show the variation in average formation energy with increasing number of N and B atoms respectively for the fixed number of B and N atoms.	115
6.4	Adsorption energy of H-atom at inequivalent sites(gray filled circle) of (a)1C and 13C, (b)22C, (c)6C and 16C Gr-island embedded within hBN.	118
6.5	Average bond order(ABO) values at different sites in reference of pristine graphene(for C-site) and hBN(B,N-sites). ABO values at different sites for different C-substitution(gray circle) configurations: (a)single C(1C), (b)3C, (c)4C, (d)13C, (e)22C and (f)33C, where red(black)circles represents the N-site rich(B-site rich) substitution and blue dotted line define the sites as written in x-axis of all plots.	119
6.6	Variation of in-plane ABO with respect to different onsite energies for representation of adsorbed species at that site and ABO of that adsorbed species(inset) with (a)1C@1B and 1C@1N, (b)22C@12B10N and @10B12N. Here red(black) color represent N-site rich(B-site rich) configuration.	121
6.7	(a)Representation of inequivalent sites for PDOS plot, (b)PDOS for up(red) and down(blue) spin for all sites mentioned in (a). Gray shade corresponds to total DOS of pristine hBN.	122

6.8	Contour plot of : ABO difference w.r.t pristine graphene and hBN for N-site rich and B-site rich configurations, spin-density from MFH calculation and DFT for N-site rich configurations respectively for (a)13C, (b)22C, and (c)33C Gr-island embedded within hBN.	123
6.9	Planar projection of Wannier centers in hydrogen passivated patch of hBN with: (a)no doping, with substitution by C of (b-c)single N, (d-e)single B, (f)neighboring BN-pair. The smaller(bigger) translucent circle represents one(two) WC(s) each representing one electron.	124
6.10	Scheme of BO calculation.	126
6.11	Adsorption energy of O ₂ for different doping configurations mentioned consistently with Fig.6.3. A site(s) of adsorption is mentioned in parenthesis. Three classes of O ₂ adsorption configurations have shown.	128
6.12	In-plane(C doped hBN) and out of plane(associated with O ₂) Wannier centers, represented by brown translucent spheres for O ₂ adsorbed on: (a)1N(C@N), (b)3B1N(C@B,B), (c)1B3N(C@N,C@N), (d)1B(B). The smaller(bigger) sphere represents one(two) WC(s) each representing one electron.	129
6.13	Free energy diagram of ORR in acidic condition on different configurations of substitution by C(inset): C@N for (a)1N, (b)1B2N, (c)10B12N and C@B for (d)1B, (e)2B1N, (f)12B10N. Blue boxes pointing out the rate limiting steps and red circle represents the catalytic site. Free energy pathway for maximum operating voltage(U _{ORR}) is shown here in red.	130

6.14	(a)Free energy diagram of OER in acidic condition for the configuration with least overpotential and (b)Volcano plot for OER w.r.t descriptor $\Delta G(O^*)-\Delta G(OH^*)$ [44]. Red dotted line in (a) corresponds to optimum operating voltage U and the red circle pointing out the catalytic site. Bigger Gr-islands have been highlighted in bold at plot (b)	134
6.15	Free energy diagram of ORR in acidic condition on different non-magnetic configurations of substitution by C(inset): C@N for (a)3B3N(C@N), (b)8B8N(C@B). Dotted boxes pointing out the rate limiting steps and red circle represents the catalytic site. Free energy pathway for maximum operating voltage is shown here in red.	136
6.16	Overpotential of all C-substituted hBN configurations (a)for ORR and (b) for OER. For magnetic Gr-islands, \diamond and \diamond represents the N-site rich and B-site rich configurations with catalytic site as mentioned within the parenthesis. For non-magnetic islands, \square and \square respectively represents C@N and C@B catalytic site. Bigger magnetic islands are highlighted in bold.	137
6.17	(a)Graphene-hBN hexagonal-Kagome hybrid system with ^{13}C Gr-island at hexagonal site and single C@B at Kagome sites. Dotted line represents the hexagonal-Kagome supercell, (b)spin-polarized DOS for the same.	138

Chapter 1

Introduction

The dimensionality of a system plays an important role in condensed matter physics since the majority of properties involving the ground states and low energy excitations can be understood from the electronic density of states about Fermi energy, which is related to the phase space dimension as we learn from our basic course of solid state physics[1].

Before the realization of realistic low dimensional materials, the notion of reduced dimension was seen to be an abstract concept where the microscopic degrees of freedom becomes restricted along one, two or all directions in three-dimensional configuration space, leading to two, one and zero-dimensional systems respectively. Insight from basic quantum mechanics can largely describe the properties of such confined systems often in sharp contrast with their bulk. The quantum mechanics of few electrons in reduce dimension leads to various exotic phenomena[2] which threw often a new field of research known as mesoscopic physics[3]. Study of electron correlation, effects of disorders, impurities etc. and their combined effect in this low dimensional systems thus became the main challenge in understanding properties of mesoscopic system[4]. Historically due to the unavailability of fabrication techniques, the onset

of research in low dimensional system was relatively slow till the end of the twentieth century. However, with the advent of exfoliation processes, the breakthrough which came in 2004[5] opened up a new era in the field of research in low dimensional, especially in two dimension(2D). After 2004 many experimental techniques have been evolved for the cleaner synthesis of layered structure with improving control of shape and size[6, 7, 8].

In the paradigm of low dimensional materials, carbon nanostructures[9, 10] such as C_{60} (buckyball), carbon nanotube, graphene nanoribbon[11] have been studied mostly due to their enormous potential as replacement of silicon for passive and active electronics[12], owing to the high and tunable mobility of electrons in these systems. Beyond carbon based materials as we go down in the periodic table many more promising layered materials[13] from insulating, semi-conducting to metallic and even superconducting [14, 15, 16] properties have been evolved in recent years. These 2D materials primarily consist of transition-metal dichalcogenides(TMDs)[15] like MoS_2 , WS_2 etc. as well as layered structure made of 2p block elements like silicene, phosphorene, germanen [17], hexagonal boron nitride(hBN), BCN systems[18, 19]. Their unique electronic structure is rooted in the spatial confinement[20]of their valence electrons and their electronic configuration of the constituents elements leading to their applications in nanotechnology like opto-electronics[21], thermoelectrics[22], ultrafast detectors and sensors[23], renewable energy resources[24, 25] etc. and more recently in materials with topologically protected states[26].

In the series of 2D materials proposed and synthesized, the lightest ones are due to the lightest elements of 2p-block, namely, boron(B), carbon(C) and nitrogen(N), constituting graphene, hexagonal boron nitride and their hybrids[Fig.1.1], which show remarkable structural resilience on account of the strong covalent bonds made by the sp^2 hybridized orbitals of B, C, and N. These systems are unique in terms of their

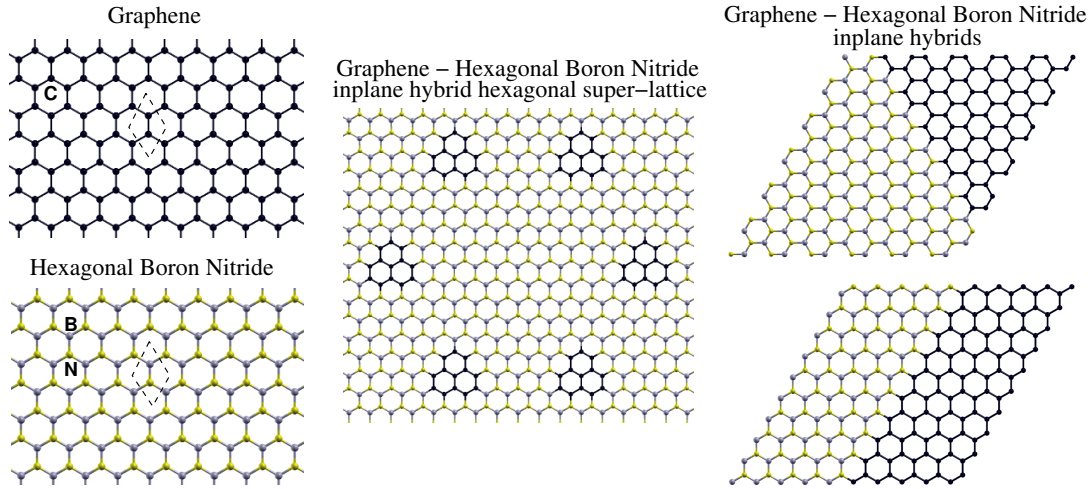


Figure 1.1: Representation of two atom basis primitive cell (dotted line) of graphene and hexagonal boron nitride. Few representative in-plane hybrids with graphene and hexagonal boron nitride.

three coordinated bipartite network structure. Electronic structure of the valence electrons in these systems is primarily determined by the $2p_z$ electrons, which on one hand, would like to delocalize from one to the other sub-lattice in order to reduce kinetic energy, while on the other hand, would also tend to localize in different sub-lattices with opposite spins in order to reduce the Coulomb potential energy. It is the competition between such inter sub-lattice localization and delocalization which determine the electronic structure of these group of materials.

In pristine graphene, the lowering of kinetic energy due to delocalization dominates over the increasing Coulomb potential leading to a non-magnetic semi-metallic ground state. In case of heteroatomic bipartite systems, the difference in electronegativities in two sub-lattices influences the competition between inter sub-lattice delocalization and localization. It is possible to suppress delocalization and stabilize a magnetic ground state with anti-ferromagnetic or ferrimagnetic order between the sub-lattices due to local or global sub-lattice asymmetry. Accordingly, electronic and magnetic properties of three coordinated bipartite nanostructure can be tuned by cutting them

into flakes, ribbons or rolling them into tubes in different directions[9] or through physical and chemical functionalization[6, 7]. Magnetic ground states established in this modified bipartite nanostructure thus opens up a new field of p-electron based magnetic materials made of non-metals. In recent years possibilities of ferromagnetism in modified graphene[27, 28] and graphene-hBN hybrid systems [29, 30], have inspired search for controllable and sustainable ferromagnetism in these three coordinated layered structures. Such atomically thin magnetic materials with large spin relaxation time[31] due to small spin-orbit coupling typical of these systems will be ideal for use in data storage and in spintronic devices[32].

Incidentally, localization of p_z electrons due to the onset of magnetism in these materials also render graphene, hBN hybrid systems chemically active opening up the possibility for these hybrid layer structures to support catalysis[33]. Carbon atoms substituting in hBN are known to form graphene island in hBN and different carbon atoms within the island are expected to have different level of chemical activation. For optimal catalysis, different reactions require different level of activation as explained by *Sabatier principle*[34]. Graphene islands in hBN with different level of activations can thus offer a catalytic platform for a range of electrochemical reactions.

1.1 Thesis outline

In this thesis, we have investigated 2D nanostructures made of 2p-block elements mainly graphene, hBN and their hybrid structures from the perspective of their possible applications in some of the contemporary problems in materials science. Through the calculation of electronic structure from first principles and simple mean-field model Hamiltonian, we have revealed new properties and proposed new materials which promise new realms of controllable magnetism and catalysis at the nanoscale.

The outline of the rest of the thesis is as follows:

In Chapter 2, I have discussed the methods and models that I have used throughout my thesis work for calculation of electronic structure. I have used density functional theory for calculation of electronic structure from first principles and have constructed Wannier functions to study chemical bonding and charge transfer processes. I have also considered mean-field Hubbard model within the tight-binding framework to study magnetism in half-filled ground states.

In Chapter 3, a brief introduction about the electronic structure of graphene and graphene nanoribbon within the tight-binding framework have been discussed. In addition, it also includes a small survey on magnetism of 2p-block element based low dimensional systems and mechanism of magnetic ordering on bipartite lattices.

In Chapter 4, I have described our studies^[35] of onset of nearest neighbor ferromagnetism in graphene nanoribbon through inhomogeneous application of bias as a proposal of electrically controlled ferromagnetism and half-metallicity at the nanoscale. In this work, we have proposed the possibility of localization induced nearest neighbor ferromagnetic order in bipartite system.

In Chapter 5, I have presented our studies^[36] on various graphene-hBN hybrid super-lattices in search of a non-metal route of ferromagnet at room temperature. We have argued about possible modifications of tight-binding model for correct representation of ground state in bipartite lattice with dissimilar on-sites energies. In this chapter, I have described the mechanism of propagation of magnetic order between local moments through hBN and a general possibility to stabilize ferromagnetic ordering of local moments at room temperature.

In Chapter 6, I have focused on the mechanistic understanding of chemical activation of carbon substituted hBN through mean-field analysis and first principles calculation. We have introduced a new parameter which can be computed from

mean-field model derived from first principles to quantify activation of sites. I have also proposed a family of non-metal candidate for cathodes in acidic fuel-cells. This chapter is a detailed description of the work which is under review [\[37\]](#).

Finally, including all the new perspective and understanding I have concluded my thesis. However, some of the work presented in the thesis are continuing further towards new directions as summarized in the last chapter, titled Future scope.

Bibliography

- [1] C. Kittel, Introduction to Solid State Physics.
- [2] Michael R. Geller, arXiv:cond-mat/0106256
- [3] Felix A. Buot, *Physics Reports*, 234, **(1993)**.
- [4] Quantum Phenomena in Mesoscopic Systems, Proceedings of the International School of Physics "Enrico Fermi", IOS Press, **(2003)**.
- [5] K. S. Novoselov *et al.*, *Science*, (Washington, DC, U. S.), 306, **(2004)**.
- [6] Mingsheng Xu, Tao Liang, Minmin Shi, and Hongzheng Chen, *Chem. Rev.*, 113, **(2013)**.
- [7] S. J. Kim, K. Choi, B. Lee, Y. Kim, B. H. Hong, *Annual Review of Materials Research*, 45, **(2015)**.
- [8] Andrew J. Mannix, Brian Kiraly, Mark C. Hersam & Nathan P. Guisinger, *Nature Reviews Chemistry*, 1, 0014, **(2017)**.
- [9] A. H. Castro Neto, F. Guinea, N. M. R. Peres, K. S. Novoselov, A. K. Geim, *Rev. Mod. Phys.*, 81, 109, **(2009)**.
- [10] A. K. Geim, *Science*, 324(5934), **(2009)**.

- [11] A. K. Geim, K. S. Novoselov, *Nat. Mater.* 6, 183, (2007).
- [12] R. M. Westervelt, *Science*, 320, 5874, (2008).
- [13] Ganesh R. Bhimanapati *et al.*, *ACS Nano*, 9(12), (2015).
- [14] N. Hamada, Si Sawada, A. Oshiyama, *Phys Rev Lett.*, 68(10), (1992).
- [15] Lei Yang *et al.*, *Nanomaterials*, 8(7), 463, (2018).
- [16] S. Uji *et al.*, *Nature*, 410, (2001).
- [17] Seymour Cahangirov, Mehmet Topsakal, Ethem Akturk, Hasan Sahin, Salim Ciraci, *Phys. Rev. Lett.*, 102, 236804, (2009).
- [18] Dmitri Golberg *et al.*, *ACS Nano*, 4(6), (2010).
- [19] M. Kawaguchi, *Adv. Mater.*, 9, (1997).
- [20] K. F. Mak, C. Lee, J. Hone, J. Shan, T. F. Heinz, *Phys. Rev. Lett.*, 105, 136805, (2010).
- [21] Qing Hua Wang, Kouros Kalantar-Zadeh, Andras Kis, Jonathan N. Coleman & Michael S. Strano, *Nature Nanotechnology*, 7, (2012).
- [22] M.S. Dresselhaus *et al.*, *Adv. Mater.*, 19(8), (2007).
- [23] F. H. L. Koppens, T. Mueller, Ph. Avouris, A. C. Ferrari, M. S. Vitiello & M. Polini, *Nature Nanotechnology*, 9, (2014).
- [24] Jingjing Duan, Sheng Chen, Mietek Jaroniec, and Shi Zhang Qiao, *ACS Catal.*, 5(9), (2015).
- [25] Hong Bin Yang *et al.*, *Science Advances*, 2(4), (2016).

- [26] Yafei Ren, Zhenhua Qiao and Qian Niu, *Reports on Progress in Physics*, 79, 6, (2016).
- [27] Yan Wang *et al.*, *Nano Lett.*, 9(1), (2009).
- [28] Zhiyong Wang, Chi Tang, Raymond Sachs, Yafis Barlas, and Jing Shi, *Phys Rev Lett.* 114, 016603, (2015).
- [29] Ru-Fen Liu, Ching Cheng, *Phys. Rev. B*, 76, 014405, (2007).
- [30] Yi Lin and John W. Connel, *Nanoscale*, 4, (2012).
- [31] Marc Drögeler *et al.*, *Nano Lett.*, 14(11), (2014).
- [32] John R. Schaibley *et al.*, *Nature Reviews Materials*, 1, 16055, (2016).
- [33] Dehui Deng, K. S. Novoselov, Qiang Fu, Nanfeng Zheng, Zhongqun Tian & Xinhe Bao, *Nature Nanotechnology*, 11, (2016).
- [34] P. Sabatier, *Ber. Deutsch. Chem. Gesellschaft*, 44. 1984. (1911).
- [35] Rita Maji, Joydeep Bhattacharjee, *Scientific Reports*, 7, Article number:17094 (2017).
- [36] Rita Maji, Joydeep Bhattacharjee, *Phys. Rev. B*, 99, 125409, (2019).
- [37] Rita Maji, Joydeep Bhattacharjee, *J. Phys. Chem. C*, (2019):(<https://pubs.acs.org/doi/10.1021/acs.jpcc.9b03229>).

Chapter 2

Calculation of Electronic structures

2.1 Introduction

Description of electronic structures enables estimation of properties of matter from first principles. Computation of general properties involves realistic estimation of ground as well excited states which require accurate incorporation of quasi-particle nature of electrons and their coupling to bosonic degrees of freedom like phonons, magnons etc., which are often prohibiting computationally. However, realistic approximations of interactions among charge, spin and vibrational degrees of freedom have led to computationally feasible paradigms for exploration of known as well as anticipated properties of existing and new materials designed for specific applications.

In this chapter, I present the computational aspects of electronic structure calculated in this thesis. Most of the analysis is done using density functional theory(DFT) based first principles calculation [1]. Besides DFT, for pedagogical purposes we have focused on simple model Hamiltonians which provide further understanding of correlated behavior of the electrons contributing to the basic phenomenology. Electronic structures of systems made of these 2p-block elements namely, Boron(B), Carbon(C)

and Nitrogen(N), are well explained from single orbital tight-binding framework owing to the fact that the band edges in these systems are described by $2p_z$ electrons, one per atom on the average. For studying magnetic properties of these systems[2] the single band mean-field Hubbard model is commonly used which matches with DFT as well as with other more accurate theoretical approaches[3] at weak to moderate coupling. To derive microscopic details of the underlying mechanism through an orbital resolved description of electronic structure we have constructed spatially localized Wannier functions from first principles[4, 5].

2.2 Single particle approximation

Within the Born-Oppenheimer approximation, solution of the exact electronic Hamiltonian[Eq.2.1] gives the complete description of electronic structure.

$$H = - \sum_i \frac{\hbar^2 \nabla_{\mathbf{r}_i}^2}{2m_e} + V_{ext}(\mathbf{r}) + \frac{e^2}{2} \sum_{i \neq j} \frac{1}{|\mathbf{r}_i - \mathbf{r}_j|}. \quad (2.1)$$

where $V_{ext}(\mathbf{r})$ is the ionic potential and last term represents the electron-electron interaction.

However, in a many electron environment exact solution of Schrödinger equation is a prohibitively challenging task given the complexity of the problem. The first challenge that we face is to describe the wave functions which is essentially a function of all the spatial and spin degrees of freedom of all the electrons. Within single particle approximation the many electron wave function is written as a combination of products of single particle orbitals $\{\phi_i(\mathbf{r}_i)\}$.

2.2.1 Hartree & Hartree Fock

The simplest ansatz is to write the many particle wave function as a product (Hartree product) of independent single particle orbitals which is known as Hartree approximation.

$$\psi_H(\{\mathbf{r}_i\}) = \phi_1(\mathbf{r}_1)\phi_2(\mathbf{r}_2)\dots\phi_N(\mathbf{r}_N). \quad (2.2)$$

where, $\{\mathbf{r}_i\}, i = 1..N$ represents position of isolated N-electrons. From variational minimization of the energy expectation value $[\langle\psi_H|H|\psi_H\rangle]$ [Eq.2.1,2.2] with respect to single particle orbitals leads to a system of Schrödinger like equations for each orbital

$$\left[-\frac{\hbar^2\nabla_{\mathbf{r}_i}^2}{2m_e} + V_{ext}(\mathbf{r}) + V_H^i(\mathbf{r})\right]\phi_i(\mathbf{r}) = \epsilon_i\phi_i(\mathbf{r}). \quad (2.3)$$

where an effective potential (Hartree potential) incorporates electron-electron interactions

$$V_H^i(\mathbf{r}) = e^2 \sum_{i \neq j} \langle \phi_j | \frac{1}{|\mathbf{r}_i - \mathbf{r}_j|} | \phi_j \rangle. \quad (2.4)$$

In terms of orbital density, $\rho_i(\mathbf{r}) = |\phi_i(\mathbf{r})|^2$ and $\rho(\mathbf{r}) = \sum_i \rho_i(\mathbf{r})$, Hartree potential can be written as

$$V_H^i(\mathbf{r}) = e^2 \sum_{i \neq j} \int \frac{\rho_j(\mathbf{r}')}{|\mathbf{r} - \mathbf{r}'|} d\mathbf{r}' = e^2 \int \frac{\rho(\mathbf{r}') - \rho_i(\mathbf{r}')}{|\mathbf{r} - \mathbf{r}'|} d\mathbf{r}'. \quad (2.5)$$

Eq.2.3,2.5 suggests that this set of equations can be solved self-consistently starting from a trial orthogonal set of orbitals $\{\phi\}$. However in Hartree approximation the antisymmetric nature of fermionic wave function has not been considered.

Subsequently representing the many electron wave function [Eq.2.2] by an antisymmetric combination of product of single particle orbitals constructed in terms of

Slater determinant constitute the Hartree-Fock approximation.

$$\psi_{HF}(\{\mathbf{r}_i\}) = \sum_i^{N!} (-1)^{P(i)} \phi_{i1}(\mathbf{r}_1) \phi_{i2}(\mathbf{r}_2) \dots \phi_{iN}(\mathbf{r}_N). \quad (2.6)$$

where P is a permutation operator and i runs over N! sequences of permutation. After variational minimization of energy expectation value with respect to many electron Hartree-Fock(HF) wave function[Eq.2.6] it leads to a set of simultaneous equation[Eq.2.7].

$$\left[-\frac{\hbar^2 \nabla_{\mathbf{r}}^2}{2m_e} + V_{ext}(\mathbf{r}) + V_H^i(\mathbf{r}) + V_{EX}^i(\mathbf{r}) \right] \phi_i(\mathbf{r}) = \epsilon_i \phi_i(\mathbf{r}). \quad (2.7)$$

with the exchange potential,

$$V_{EX}^i(\mathbf{r}) = -e^2 \int \frac{\rho_{EX}^i(\mathbf{r}, \mathbf{r}')}{|\mathbf{r} - \mathbf{r}'|} d\mathbf{r}'. \quad (2.8)$$

where single particle exchange density,

$$\rho_{EX}^i(\mathbf{r}, \mathbf{r}') = \sum_{i \neq j} \frac{\phi_i(\mathbf{r}') \phi_i^*(\mathbf{r}) \phi_j(\mathbf{r}) \phi_j^*(\mathbf{r}')}{\phi_i(\mathbf{r}) \phi_i^*(\mathbf{r})}. \quad (2.9)$$

HF potential in terms of density[Eq.2.5,2.8] can be written as ,

$$\begin{aligned} V_{HF}^i(\mathbf{r}) &= V_H^i(\mathbf{r}) + V_{EX}^i(\mathbf{r}) \\ &= e^2 \int \frac{\rho(\mathbf{r}') - \rho_i(\mathbf{r}')}{|\mathbf{r} - \mathbf{r}'|} d\mathbf{r}' - e^2 \int \frac{\rho_{EX}^i(\mathbf{r}, \mathbf{r}')}{|\mathbf{r} - \mathbf{r}'|} d\mathbf{r}' \\ &= e^2 \int \frac{\rho(\mathbf{r}')}{|\mathbf{r} - \mathbf{r}'|} d\mathbf{r}' - e^2 \int \frac{\rho_i(\mathbf{r}') + \rho_{EX}^i(\mathbf{r}, \mathbf{r}')}{|\mathbf{r} - \mathbf{r}'|} d\mathbf{r}' \\ &= e^2 \int \frac{\rho(\mathbf{r}') - \rho_{HF}^i(\mathbf{r}, \mathbf{r}')}{|\mathbf{r} - \mathbf{r}'|} d\mathbf{r}'. \end{aligned} \quad (2.10)$$

We note here that unlike the Hartree equations HF equation can not be cast as eigen-

value problem as is and hence it is more complicated to solve. Nevertheless, HF formalism also presents a more accurate self-consistent framework for calculation of single particle orbitals which describe the electronic structure. HF approximation treats the fermionic exchange exactly, but consideration of single Slater determinant as the HF basis does not incorporate the effect of primarily the dynamic correlations which can be brought in if we expand the HF basis as a combination of Slater determinants made of single particle orbitals in different levels of excitations. Although this approach, which is known as configuration interaction(CI), provides the most accurate description of electronic structure, it is computationally very expensive and applicable realistically only to small molecules given the standard sizes of available computational resources.

To our rescue alternate approaches have been evolved over the years to describe many electron systems with reasonable approximations for electron-electron interactions. The key approach so far in this direction is due to density functional theory(DFT), where, instead of single particle orbitals it is the single particle density of the ground state which is the key ingredient.

2.2.2 Overview of density functional theory

Density functional theory(DFT) is an exact theory for many electron systems based on Hohenberg-Kohn(H-K)(1964)[\[6\]](#) and Kohn-Sham(K-S)(1965)[\[7\]](#) theorems. As schematically shown in Fig.[2.1](#) first H-K theorem corresponds to the unique mapping of external potential V_{ext} to the electron density $n(\mathbf{r})$ and the second H-K theorem provide the energy variational principle similar to HF method. $F_{HK}[n]$ is the universal functional of the ground state density $n_0(\mathbf{r})$ which incorporates all electron-electron interactions namely the appropriately screened exchange and correlation.

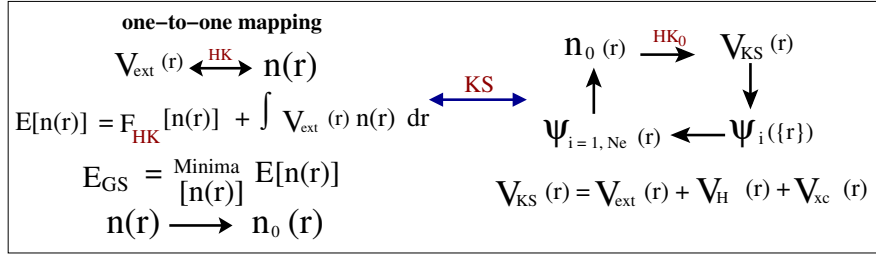


Figure 2.1: Schematic representation of Hohenberg-Kohn(left) and Kohn-Sham(right) formalism. $E[n]$ is energy functional and $F_{HK}[n(\mathbf{r})]$ is H-K universal functional, variational minimization of which gives the exact ground state energy and density $n_0(\mathbf{r})$. $\psi_i(\mathbf{r})$ are fictitious K-S states including ground state wave function $\psi_0(\mathbf{r})$ and ground state density $n_0(\mathbf{r})$

Based on H-K theorems, in K-S approach many body interacting Hamiltonian has been replaced by an auxiliary system with an ansatz that the ground state density of the actual interacting system is equal to that of some chosen non-interacting system. Hence, utilizing the H-K theorems, the total energy functional in terms of N K-S orbitals $\psi_i(\mathbf{r})$ can be written as,

$$\begin{aligned}
 E_{KS}[n] &= T[n] + E_{xc}[n] + E_H[n] + E_{ext}[n] \\
 &= \sum_i^N \int d\mathbf{r} \psi_i^*(\mathbf{r}) \left(-\frac{1}{2} \nabla^2 \right) \psi_i(\mathbf{r}) + E_{xc}[n] + \frac{e^2}{2} \int \frac{n(\mathbf{r})n(\mathbf{r}')}{|\mathbf{r} - \mathbf{r}'|} d\mathbf{r}d\mathbf{r}' + \int V_{ext}(\mathbf{r})n(\mathbf{r})d\mathbf{r}.
 \end{aligned} \tag{2.11}$$

where electron density,

$$n(\mathbf{r}) = \sum_{i=1}^N |\psi_i(\mathbf{r})|^2.$$

$T[n]$ is the kinetic energy, $E_H[n]$ is Hartree term, E_{xc} is exchange-correlation energy and E_{ext} is energy corresponding to external potential. From variational minimization of K-S energy functional within their orthogonality constraint,

$$\delta E_{KS}[n] - \sum_i^N \sum_j^N \varepsilon_{ij} \int \delta \psi_i^* \psi_j d\mathbf{r} = 0. \tag{2.12}$$

leads to

$$\sum_i^N \int \delta\psi_i^* \left[\left(-\frac{1}{2} \nabla^2 + V_{eff}(\mathbf{r}) \right) \psi_i - \sum_j^N \varepsilon_{ij} \psi_j \right] d\mathbf{r} = 0. \quad (2.13)$$

As, ψ_i^* are independent hence from above equation,

$$\left(-\frac{1}{2} \nabla^2 + V_{eff}(\mathbf{r}) \right) \psi_i = \sum_j^N \varepsilon_{ij} \psi_j. \quad (2.14)$$

Since ε_{ij} is hermitian so it can be diagonalized by a unitary transformation of the K-S orbitals which leaves the density and hence the Hamiltonian invariant. Hence, the K-S equation becomes

$$H_{KS} \psi_i(r) = \left(-\frac{1}{2} \nabla^2 + V_{eff}(\mathbf{r}) \right) \psi_i = \varepsilon_i \psi_i. \quad (2.15)$$

where,

$$V_{eff}(\mathbf{r}) = V_{ext}(\mathbf{r}) + V_H(\mathbf{r}) + V_{xc}(\mathbf{r}). \quad (2.16)$$

where,

$$V_{xc}(\mathbf{r}) = \frac{\delta E_{xc}[n(\mathbf{r})]}{\delta n(\mathbf{r})}. \quad (2.17)$$

V_H is Hartree potential, V_{ext} is external potential experienced by the electrons due to nuclei and V_{xc} is exchange-correlation potential. This equation can be cast as an eigenvalue problem like in Hartree approach but unlike Hartree or Hartree-Fock we have a single equation instead of a set of equations which can be solved self-consistently from a suitable initial guess wave function. The exact information about a physical system from the solution of K-S equation[Eq.2.15] is mainly limited by the accuracy of exchange-correlation term. Nonetheless, DFT provides a computationally efficient approach for calculation of electronic structure from first principles(*ab-initio*) with the input of atomic position and valence configurations of atoms. Throughout this

thesis, all first principles calculations are based on DFT.

DFT also provides scope for not only computation of electronic structure of a given configuration of atoms but also enables estimation of minimum energy configuration of materials. Hellmann-Feynman theorem enables computation of forces on atoms from the electronic structure of ground state. Atoms can be moved under the action of these forces to minimize total energy as per the Broyden-Fletcher-Goldfarb-Shanno (BFGS) scheme [8]. Through successive computation of electronic structure and evolution of atomic configurations structure of materials can be optimized towards the minimum energy configuration starting from a reasonable guess. Total energy as a parameter of unit cell volume is further fit to Murnaghan [9] equation of state to estimate the size of the unit cell which minimizes the total energy.

2.2.2.1 Exchange and Correlation

The key problem for electronic structure calculation is the correct accounting of many body interactions. Exchange and correlation energy are the combined contribution of an interplay of charge and spin degrees of freedom. Exchange energy is due to Pauli's exclusion principle which lowers the total energy by keeping the similar spin apart which reduces their Coulomb repulsion. Correlation is a collective behavior of electrons amounting to re-organization of charge density which leads to screening of Coulomb and exchange interactions. In effect, these quantum mechanical interactions reduce the electron density at \mathbf{r} due to an instantaneous occurrence of the second electron located at \mathbf{r}' . Therefore each electron creates a depletion region around it or a hole which is known as exchange-correlation hole. So, the exchange-correlation energy (E_{xc}) together can be viewed as the energy resulting from the interaction between an electron and its exchange-correlation hole [10].

In K-S theory exchange-correlation energy is included as energy functional of

density $[n(\mathbf{r})]$. The local potential, $V_{xc}(\mathbf{r})$ which incorporates these electron correlation is then derived from functional derivative of the exchange-correlation energy functional[Eq.2.17]. Since, the exact form of exchange-Correlation energy functional is not known the key approximation within DFT is of $E_{xc}[n]$ in the total energy functional[Eq.2.12]. The simplest approximation is based on density of homogeneous electron gas and the corresponding functional can be expressed as,

$$E_{xc}[n^\sigma] = \int d\mathbf{r} n(\mathbf{r}) \epsilon_{xc}([n^\sigma], \mathbf{r}). \quad (2.18)$$

where $\epsilon_{xc}([n^\sigma], \mathbf{r})$ is an energy per electron at a position \mathbf{r} based on density $n^\sigma(\mathbf{r})$ at neighborhood of \mathbf{r} and σ represents the spin assuming the quantization of spin to be same at all points in space. This is known as local(spin) density approximation (**L(S)DA**)[\[11\]](#). Beyond this, in the next level of improved functional along with L(S)DA, the inclusion of the gradient of density for first $|\nabla n^\sigma|$ or higher orders is known as generalised gradient approximation(**GGA**)[\[11\]](#). This approximate functionals (LDA, GGAs) are remarkably accurate for wide band gap (group IV & II-V) semiconductors, molecules with covalent, ionic bonding and even for transition metals. However, in the case of strongly correlated materials, this functional has some discrepancies[\[12\]](#).

Since the above mentioned functional has an approximate exchange as well as correlation and the next level of improvement is possible through incorporation of exact exchange[\[12\]](#). These new functionals are known as hybrid functional which adds corrections due to H-F exchange to LDA, GGAs functionals as Eq.2.19. The coefficients are empirically adjusted for atoms and molecules to capture the features

of local and non-local effects. The most general form of hybrid functionals [12] are :

$$E_{xc}^{hybrid} = E_{xc}^{LDA/GGA} + a_0(E_X^{HF} - E_{xc}^{LDA,GGA}) + \dots \quad (2.19)$$

till now these are known to be the best accurate functionals for a description of excitation energy and realistic band gap with feasible computational resources.

2.2.2.2 Pseudopotential Method

In many electron systems, the core electrons and valence electrons have different contributions to its electronic structure. The core electrons are more bound to the nuclei while the valence electrons are relatively free due to the screening of the nuclei potential by the core electrons. The core electron wave functions have less contribution in low energy properties such as chemical bonding, conductivity, optical excitation etc. and also they remain effectively unchanged irrespective of chemical environment. The valence wave functions, in general, have complex nature in the core region ($r < R_c$) due to the presence of nodes which demands a large set of plane wave basis and hence a large kinetic energy cut-off (E_{cutoff}) [Eq. 2.20].

$$\frac{1}{2}G^2 \leq E_{cutoff}. \quad (2.20)$$

where G is reciprocal lattice vector.

In standard DFT calculation like ours, we considered the valence electrons in an effective smooth pseudopotential. This way the valence wave functions becomes smooth enough within the core region to be described by a reasonably small set of plane waves. These pseudopotentials are generated from all electron calculations of atoms such that the pseudo wave functions satisfy the properties of valence electrons

outside the cut-off radius R_c [Fig. 2.2]. Depending on the choice of certain constraints and division of core/semi-core and valence shell of electronic configurations there are different types of pseudopotentials[11]. The accuracy of the pseudopotentials depends on their ‘transferability’ such that the same pseudopotential for a given element can be used in various chemical environment and maximally reproduce scattering properties of the true potential. Therefore, the pseudopotentials should be accurate as well as smooth which requires less no of basis sets in order to reduce the computational cost.

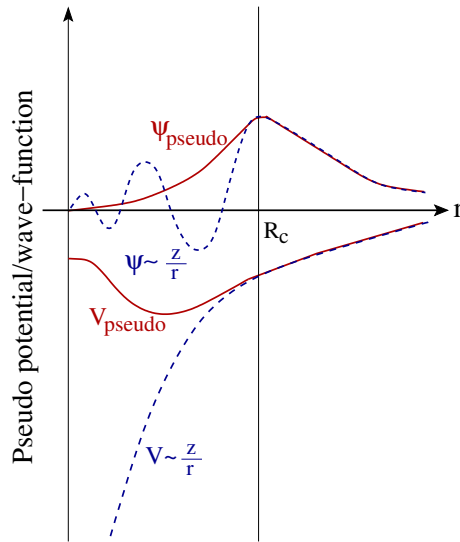


Figure 2.2: Wave function(blue) in real Coulomb potential(blue) and representation of pseudopotential(red) and pseudo wave function(red)

Norm-conserving ones[13] are the most commonly used pseudopotential which, as the name suggests conserve the normalization of the pseudo wave function inside R_c so that the total charge within the core region remain preserved. Ultrasoft[14] ones constitute the other set of commonly used variant of pseudopotentials, which maximally smoothen(delocalizes) the pseudo wave functions inside the core region at the cost of nonconservation of total charge, leading to requirement of additional correction term, namely, the augmented charges.

2.2.3 Computation based on DFT

Plane waves are the most popular choice as a basis for the electronic structure calculation within the periodic boundary condition. In the DFT based electronic structure calculation schemes, the primary solution of K-S equation follows the iterative loop as shown in Fig. 2.3. Its primary outcomes are total energy and some related quantities such as forces, stresses, density in the given configuration. As the K-S equation

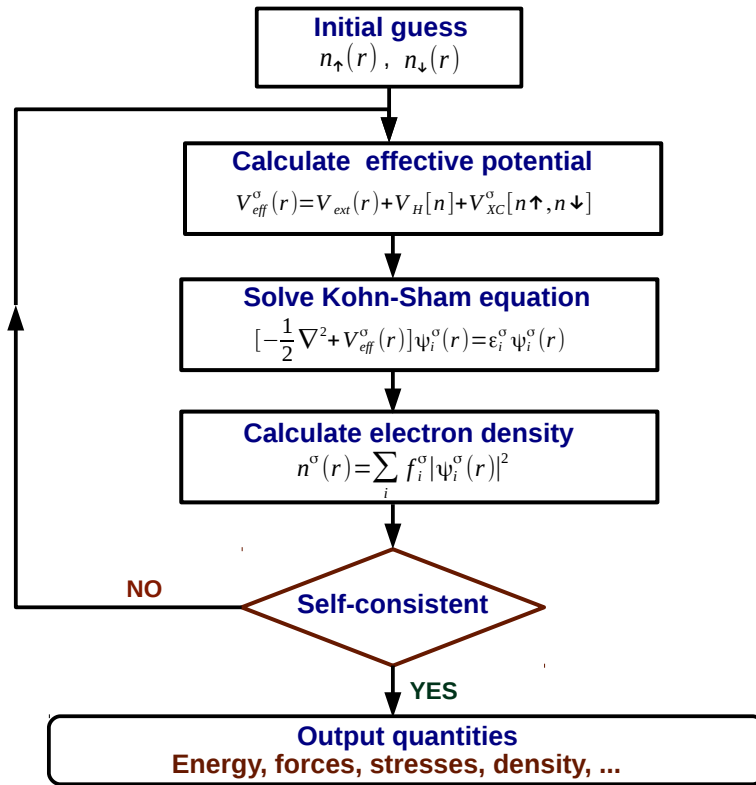


Figure 2.3: Self consistent scheme for Kohn-Sham equations

need to be solved in a self-consistent approach on some suitable basis sets and grids, this turns the DFT into a problem of multi-variable minimization and single particle K-S equation into a non-linear eigenvalue equation for its dependencies. I have used *Quantum open-Source Package for Research in Electronic Structure, Simulation, and Optimization* which is commonly known as “Quantum ESPRESSO(QE)” [15]. This

is an integrated software package for atomistic simulations based on electronic structure, using DFT in a plane wave basis set using both normconserving and ultrasoft pseudopotentials with several exchange-correlation functionals. QE is a suite of Fortran codes which can be easily modified as per post processing(pp) requirements. QE offers a wide range of pp module which enables calculation of phonon spectra, self-energy correction, ballistic conductance etc. Although not used in this thesis there exists a suit of DFT codes(SIESTA, LMTO etc.) which uses localized orbitals as a basis which can be more effective for isolated systems like molecules or clusters compare to plane waves.

2.2.3.1 Phonon calculation

Many important properties of crystalline materials such as thermal properties, mechanical properties, optical properties, and superconductivity etc. depend on lattice dynamics and its coupling with electronic degrees of freedom. In general lattice vibrations are the displacement fluctuations around the equilibrium position of an atom within the lattice due to thermal energy and it becomes more pronounced at higher temperature. In quantum mechanical description, these collective atomic vibrations are quantized in energy as $\hbar\omega = h\nu$ with $\nu = \omega/2\pi$ being the frequency of vibration and this quanta of lattice vibrations are known as phonon. The nature of phonon modes and distribution of frequencies depends on dynamical properties[16] of the crystal which can be obtained from electronic structure.

Within first principles framework, the calculations of phonon modes are possible either due to frozen phonon method[17] or with the linear response approximation of density functional perturbation theory(DFPT)[17]. Forces are estimated from finite displacement method in the former and direct calculation of second-order derivatives of the energy obtained from DFT in the later. A schematic theoretical background of

DFPT along with DFT in a plane wave basis has been described here, which we have used for calculation of phonon modes using Quantum espresso[15]. Due to the adiabatic approximation of Born and Oppenheimer, ionic degrees of freedom can be decoupled from electronic degrees of freedom and let $E(\mathbf{R})$ is the ground state energy within an effective field distribution $\{R\}$, then Born-Oppenheimer Hamiltonian can be written as,

$$\begin{aligned}
H(R) = & -\frac{\hbar^2}{2m} \sum_i \frac{\partial^2}{\partial \mathbf{r}_i^2} + \frac{e^2}{2} \sum_{i \neq j} \frac{1}{|\mathbf{r}_i - \mathbf{r}_j|} \\
& - \sum_{Ii} \frac{Z_I e^2}{|\mathbf{r}_i - \mathbf{R}_I|} + \frac{e^2}{2} \sum_{I \neq J} \frac{Z_I Z_J}{|\mathbf{R}_I - \mathbf{R}_J|},
\end{aligned} \tag{2.21}$$

where, Z_I, Z_J are charges of nuclei at $\mathbf{R}_I, \mathbf{R}_J$ respectively, $-e$ is electronic charge. First two terms represents electronic kinetic and potential energy contribution, third term is electron-nucleus interaction($V_{\mathbf{R}}$) and last term is electrostatic interaction(E_N) between the nuclei. Forces(\mathbf{F}_I) acting on each nuclei can be calculated from Hellmann-Feynman[10] forces. Within the harmonic approximation vibrational frequencies(ω) are determined from eigenvalues as,

$$\det \left| \frac{1}{\sqrt{M_I M_J}} \frac{\partial \mathbf{F}_I}{\partial \mathbf{R}_J} - \omega^2 \right| = 0 \tag{2.22}$$

From Hellmann-Feynman theorem,

$$\mathbf{F}_I = - \int n_{\mathbf{R}}(\mathbf{r}) \frac{\partial V_{\mathbf{R}}(\mathbf{r})}{\partial \mathbf{R}_I} d\mathbf{r} - \frac{\partial E_N(\mathbf{R})}{\partial \mathbf{R}_I}. \tag{2.23}$$

Where,

$$\frac{\partial^2 E(\mathbf{R})}{\partial \mathbf{R}_I \partial \mathbf{R}_J} = - \int \frac{\partial n_{\mathbf{R}}(\mathbf{r})}{\partial \mathbf{R}_J} \frac{\partial V_{\mathbf{R}}(\mathbf{r})}{\partial \mathbf{R}_I} d\mathbf{r} + \int n_{\mathbf{R}}(\mathbf{r}) \frac{\partial^2 V_{\mathbf{R}}(\mathbf{r})}{\partial \mathbf{R}_I \partial \mathbf{R}_J} d\mathbf{r} + \frac{\partial^2 E_N(\mathbf{R})}{\partial \mathbf{R}_I \partial \mathbf{R}_J}. \quad (2.24)$$

Ground state charge density $n_{\mathbf{R}}(\mathbf{r})$ for a fixed nuclei position \mathbf{R} and its linear distribution $\frac{\partial n_{\mathbf{R}}(\mathbf{r})}{\partial \mathbf{R}_J}$ is obtained from DFPT, where the ‘perturbing potential’ is the deformation of nuclear potential due to displacement. Below a schematic description of DFPT approach[Fig. 2.4].

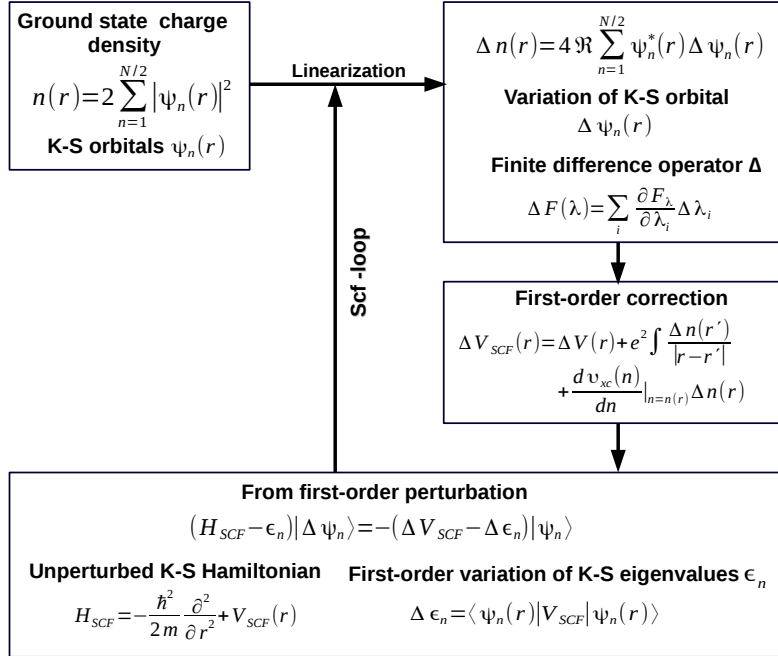


Figure 2.4: self-consistent loop of DFPT for phonon mode calculation

2.2.3.2 Van der Waals correction

Van der Waals interactions are short-ranged and it contains attractive as well as repulsive part, where the attractive part represents the actual short range properties

acting between atoms, molecules, and interfaces while the repulsive part is basically the quantum mechanical prevention of closest approach obeying Pauli exclusion principles and electrostatic repulsion between the interacting species. The attractive part of Van der Waals interaction primarily occurs due to an interaction between fluctuating charge densities around atoms [18]. These fluctuations can be sourced at variation of electronegativity of atoms whose oscillations causes an oscillatory electronic charge density known as induced moment and an attractive interaction happen between these two. Similar attractive interaction happens between two permanent dipoles that exist in case of polar systems and also between induce dipoles in neutral systems due to instantaneous fluctuation in charge densities. The latter is known as London dispersion interaction [19] which is understood as the generic source on dispersion interaction. Although in some scenario the amplitude of van der Waals interaction is weak this is not the case always partially if the interacting species contain localized or unpaired electrons and it is often difficult to quantify.

From the aforementioned interactions, London dispersion term has a significant impact on physical observables. In general, the first principles calculations does not include this dispersion correction within local or semi-local exchange-correlation functionals [12, 20]. Several methods have been evolved to treat van der Waals interactions ranging from derivation of new non-local functionals within first principles to empirical fitting to the energy functionals [18]. The most popular approach to account for dispersion correction in DFT is by addition of extra energy proposed by Grimme and co-workers [21, 22, 23] as,

$$E_{dis} = -S_6 \sum_{I=1}^{N-1} \sum_{J=I+1}^N \frac{C_6^{IJ}}{R_{IJ}^6} f_{dmp}(R_{IJ}), \quad (2.25)$$

where S_6 is a scaling parameter that depends on the exchange-correlation functional

and C_6^{IJ} is dispersion coefficient for the atom pair IJ, N is the number of atoms, and R_{IJ} being the distance between atomic site I and J. The repulsive interaction between the nuclei for very small R_{IJ} is taken into account by the damping function f_{dmp} [24]. This approach is known as DFT-D correction with which, depending on Eq. 2.25 three different parametric corrections have been proposed as $DFT - D_n$ for (n=1,2,3). In case of n=1,2 attractive part of the form R^{-6} [21, 22] is considered with predefined scaling factor. In case of n=3 an additional R^{-8} term also considered recursively. It is important to calculate the coefficients by taking into account the environment effect [23]. DFT-D correction contains some error due to overestimation of correlation which may have been already accounted for exchange-correlation potential in the functional, nevertheless it shows high accuracy in estimation of atomization energies, electron affinities, self-interaction error-related problems, barrier heights, reaction energy pathway, various inter and intra-molecular non-covalent interactions etc. [24].

2.3 Simple models for electronic structure

Weakly correlated electrons in a periodic potential are realistically described by band theory [sec. 2.3.1]. However, model Hamiltonians have been evolved to probe primarily the dominant many particle interactions. Depending on the complexity of materials and physics involved model Hamiltonians are used to study the key driving interactions in place of the more complicated total Hamiltonian with all possible interactions. Band structure calculations from model Hamiltonians provides us a scope to study the interplay of delocalization due to hopping and localization due to applied potential and electron-electron Coulomb interactions. This we will discuss in detail in the following.

2.3.1 Electrons in periodic potential

In treating periodic solids the wave function from Born-von Karman periodic boundary condition can be written as :

$$\psi(\mathbf{r}) = \psi(\mathbf{r} + N_1\mathbf{a}_1 + N_2\mathbf{a}_2 + N_3\mathbf{a}_3), \quad (2.26)$$

where $N_1 \times N_2 \times N_3$ is the no of unit cells constituting the crystal and \mathbf{a}_i ($i=1,2,3$) are three lattice vectors. For a cell periodic Hamiltonian :

$$H(\mathbf{r}) = H(\mathbf{r} + \mathbf{R}), \quad (2.27)$$

where $\mathbf{R} = n_1\mathbf{a}_1 + n_2\mathbf{a}_2 + n_3\mathbf{a}_3$ is real space lattice vector and $\{n_i\} \rightarrow \mathbb{Z}$. Bloch's theorem results into :

$$\psi_{n\mathbf{k}}(\mathbf{r}) = u_{n\mathbf{k}}(\mathbf{r})e^{i\mathbf{k}\cdot\mathbf{r}}, \quad (2.28)$$

where $u_{n\mathbf{k}}(\mathbf{r})$ has the cell periodicity of the Hamiltonian, n is the band index and within Born-von Karman boundary condition the allowed values of \mathbf{k} , also known as crystal momentum are given by :

$$\mathbf{k} = \sum_{i=1}^3 \frac{m_i}{N_i} \mathbf{b}_i, \quad (2.29)$$

where m_i is integer and \mathbf{b}_i ($i=1,2,3$) are reciprocal lattice vectors. The cell periodic wave functions $u_{n\mathbf{k}}(\mathbf{r})$ can be obtained as eigen function of the Bloch Hamiltonian

$$H(k) = -\frac{(p + \hbar k)^2}{2m_e} + v(r), \quad (2.30)$$

where $v(\mathbf{r} + \mathbf{R}) = v(\mathbf{r})$. The eigenvalues and eigenstates of $H(k)$ provides the description of energy levels and charge density of an electron in a periodic potential which is leading to electronic structure of periodic system in terms of band structure.

The Bloch function $\psi_{n\mathbf{k}}(\mathbf{r})$ can be expanded in the basis of Wannier functions $\phi_n(\mathbf{r} - \mathbf{R})$ as

$$\psi_{n\mathbf{k}}(\mathbf{r}) = \sum_{\mathbf{R}} e^{i\mathbf{k}\cdot\mathbf{R}} \phi_n(\mathbf{r} - \mathbf{R}). \quad (2.31)$$

Hence,

$$\phi_n(\mathbf{r} - \mathbf{R}) = \sum_{\mathbf{k}} e^{-i\mathbf{k}\cdot\mathbf{R}} \psi_{n\mathbf{k}}(\mathbf{r}). \quad (2.32)$$

With proper gauge transformation, Wannier functions can be constructed to be maximally localized primarily within a unit cell thus constituting an ideal set of localized orthogonal basis. We will discuss the construction of Wannier function in more detail in sec. [2.4](#).

2.3.2 Tight-Binding model

Tight-binding model is the simplest single particle approach for calculation of electronic structure primarily of periodic solids. Tight-Binding(TB) model considers an approximate set of wave functions constructed from the superposition of wave functions for isolated atoms located at each atomic sites. This model is particularly very instructive since a fairly accurate description of electronic structure near the Fermi energy can be obtained with minimal input parameters which can be tuned to match experimental results. Within the TB Hamiltonian wave function of a system of atoms is considered to be a linear combination of atomic orbitals $\{\phi(\mathbf{r})\}(\mathbf{R}=0)$,

$$H_{at}\phi_j(\mathbf{r}) = E_j\phi_j(\mathbf{r}). \quad (2.33)$$

H_{at} being the atomic Hamiltonian and E_j being the energy levels of a single atom. Recalling Eq.2.27 and Eq.2.31 the Schrödinger equation for the crystal can be written as,

$$H\psi_{m\mathbf{k}}(\mathbf{r}) = (H_{at} + \Delta V)\psi_{m\mathbf{k}}(\mathbf{r}) = \varepsilon_m(\mathbf{k})\psi_{m\mathbf{k}}(\mathbf{r}), \quad (2.34)$$

where, H is the crystal Hamiltonian and ΔV contains the corrections to reproduce the full periodic potential of the crystal. Now multiplying Eq.2.34 by $\phi_m^*(\mathbf{r})$ and using Eq.2.33

$$(\varepsilon_m(\mathbf{k}) - E_m) \int \phi_m^*(\mathbf{r})\psi_{m\mathbf{k}}(\mathbf{r})d^3r = \int \phi_m^*(\mathbf{r})\Delta V\psi_{m\mathbf{k}}(\mathbf{r})d^3r. \quad (2.35)$$

Simplifying Eq.2.35 and imposing the orthonormality for atomic wave function the Bloch energy of a state,

$$\begin{aligned} (\varepsilon_m(\mathbf{k}) - E_m) \sum_n \sum_{\mathbf{R}} \int d^3r \phi_m^*(\mathbf{r})\phi_n(\mathbf{r} - \mathbf{R})e^{i\mathbf{k}\cdot\mathbf{R}} &= \sum_n \int d^3r \phi_m^*(\mathbf{r})\Delta V\phi_n(\mathbf{r}) \\ &+ \sum_n \sum_{\mathbf{R}} \int d^3r \phi_m^*(\mathbf{r})\Delta V\phi_n(\mathbf{r} - \mathbf{R})e^{i\mathbf{k}\cdot\mathbf{R}} \\ (\varepsilon_m(\mathbf{k}) - E_m)(1 + \sum_n \sum_{\mathbf{R}} \int d^3r \phi_m^*(\mathbf{r})\phi_n(\mathbf{r} - \mathbf{R})e^{i\mathbf{k}\cdot\mathbf{R}}) &= \int d^3r \phi_m^*(\mathbf{r})\Delta V\phi_m(\mathbf{r}) \\ &+ \sum_n \sum_{\mathbf{R}} \int d^3r \phi_m^*(\mathbf{r})\Delta V\phi_n(\mathbf{r} - \mathbf{R})e^{i\mathbf{k}\cdot\mathbf{R}}. \end{aligned}$$

Therefore, the energy in terms of TB-matrix elements $\beta_m, \alpha_{m,n}$ and $\gamma_{m,n}$

$$\varepsilon_m(\mathbf{k}) = E_m - \frac{\beta_m + \sum_{\mathbf{R}} \sum_n \gamma_{m,n}(\mathbf{R})e^{i\mathbf{k}\cdot\mathbf{R}}}{1 + \sum_{\mathbf{R}} \sum_n \alpha_{m,n}(\mathbf{R})e^{i\mathbf{k}\cdot\mathbf{R}}}. \quad (2.36)$$

where E_m is onsite energy of the m-th atomic orbital.

$$\beta_m = - \int d^3r \Delta V |\phi_m(\mathbf{r})|^2 \quad (2.37)$$

$$\alpha_{m,n}(\mathbf{R}) = \int d^3r \phi_m^*(\mathbf{r}) \phi_n(\mathbf{r} - \mathbf{R}) \quad (2.38)$$

$$\gamma_{m,n}(\mathbf{R}) = - \int d^3r \phi_m^*(\mathbf{r}) \Delta V \phi_n(\mathbf{r} - \mathbf{R}). \quad (2.39)$$

β_m [Eq.2.37] represents the change in atomic energy due to the presence of periodic potential and this gives a small correction within TB-formalism. $\alpha_{m,n}$ [Eq.2.38] is the overlap of atomic orbitals located at different sites which is negligible within TB approximation. The most important parameter is $\gamma_{m,n}$ [Eq.2.39], the inter-atomic overlap integral between two atomic sites which is also known as ‘hopping’ parameter. The hopping parameter will be different for nearest or next-nearest neighbor overlap and its sign will be positive or negative depending on the degree of overlap and orientation of the orbitals in neighboring sites as described in detail by Slater-Koster[25] approach.

2.3.3 Description of interacting electrons : second quantization

In second quantization formalism considering the vacuum state $|\Omega\rangle$ and field operators $a_\lambda, a_\lambda^\dagger$ the N particle many-body state can be written as,

$$\frac{1}{\sqrt{\prod_\lambda n_\lambda!}} a_{\lambda_N}^\dagger \dots a_{\lambda_1}^\dagger |\Omega\rangle = |\lambda_1, \lambda_2, \dots, \lambda_N\rangle, \quad (2.40)$$

where the field operators satisfies the following anticommutation relations

$$\{a_\lambda, a_\mu^\dagger\} = \delta_{\lambda\mu}, \quad \{a_\lambda, a_\mu\} = \{a_\lambda^\dagger, a_\mu^\dagger\} = 0. \quad (2.41)$$

Single particle or one-body operators \hat{O}_1 acting on a N particle Hilbert space [Eq.2.40] in general can be written as

$$\hat{O}_1 = \sum_{m=1}^N \hat{o}_m, \quad (2.42)$$

where \hat{o}_m is a single particle operator acting on m-th particle. The same in terms of field operators in any general basis can be written as

$$\hat{O}_1 = \sum_{\mu\nu} \langle \mu | \hat{o}_1 | \nu \rangle a_{\mu}^{\dagger} a_{\nu}. \quad (2.43)$$

Two body operator (\hat{O}_2) in which represent the pairwise interaction between two particles are considered can be written as

$$\hat{O}_2 = \sum_{\mu\mu'\nu\nu'} \langle \mu\mu' | \hat{o}_2 | \nu\nu' \rangle a_{\mu'}^{\dagger} a_{\mu}^{\dagger} a_{\nu} a_{\nu'}. \quad (2.44)$$

Starting with a generic interacting Hamiltonian for N particle systems,

$$H = H_0 + V_{e-e} = \sum_{i=1}^N \left(\frac{p_i^2}{2m_e} + V_{ext}(\mathbf{r}_i) \right) + \frac{1}{2} \sum_{i \neq j}^N V_{ee}(\mathbf{r}_i - \mathbf{r}_j), \quad (2.45)$$

we can express this in terms of field operators $c_{i\sigma}$ and $c_{i\sigma}^{\dagger}$ which can be defined on the basis of localized orbitals $\phi_i(\mathbf{r})$ as

$$| \phi_i \rangle = \int_0^V d\mathbf{r} | r_{\sigma} \rangle \langle r_{\sigma} | \phi_{i\sigma} \rangle \quad (2.46)$$

where $| \phi_i \rangle = c_{i\sigma}^{\dagger} | \Omega \rangle$ and $| r_{\sigma} \rangle = c_{\sigma}^{\dagger}(\mathbf{r}) | \Omega \rangle$ leads to

$$c_{i\sigma}^{\dagger} = \int_0^V d\mathbf{r} c_{\sigma}^{\dagger}(\mathbf{r}) \phi_i^*(\mathbf{r}), \quad (2.47)$$

where $c_{i\sigma}^{\dagger}$ can be interpreted as a creation operator which create an electron with spin

σ at site i and they obey fermionic commutation relations.

Therefore, with respect to this operators, the one body operator takes the following form

$$\hat{h}_1 = \sum_{ii,\sigma} \epsilon_i c_{i\sigma}^\dagger c_{i\sigma} + \sum_{i \neq j} \sum_{\sigma} t_{ij} c_{i\sigma}^\dagger c_{j\sigma}, \quad (2.48)$$

where, $\epsilon_i = \langle i | H_0 | i \rangle$ and $t_{ij} = \langle i | H_0 | j \rangle$ represents onsite and hopping term respectively. $t_{ij} < 0$ for bound states. This \hat{h}_1 describes non-interacting Hamiltonian in second quantized notation.

2.3.3.1 Second quantized description of electrons in periodic potential

Here we make a small digression to derive a second quantized description of an electron in a periodic potential. Therefore recalling the TB Hamiltonian in presence of a periodic potential $V(\mathbf{r}) = \sum_{\mathbf{K}} V_{\mathbf{K}} e^{i\mathbf{K} \cdot \mathbf{r}}$ and using

$$c_i = \frac{1}{\sqrt{N}} \sum_{\mathbf{k}} c_{\mathbf{k}} e^{i\mathbf{k} \cdot \mathbf{R}_i}, \quad (2.49)$$

which annihilate an electron at lattice site \mathbf{R}_i . Hence, $H = H_0 + V(\mathbf{r})$ in Fourier space leads to

$$H = \sum_{\mathbf{k}} \epsilon(\mathbf{k}) c_{\mathbf{k}}^\dagger c_{\mathbf{k}} + \sum_{\mathbf{k}, \mathbf{K}} V_{\mathbf{K}} c_{\mathbf{k}+\mathbf{K}}^\dagger c_{\mathbf{k}}. \quad (2.50)$$

where $c_{\mathbf{k}}^\dagger (c_{\mathbf{k}})$ is creation(annihilation) operator.

As a further example the Hamiltonian for two sites (c,d) per unit cell using Eq.2.48 can be written as,

$$H = t \sum_i (c_i^\dagger d_i + d_i^\dagger c_{i+1} + h.c.) + \sum_i \epsilon_c c_i^\dagger c_i + \sum_i \epsilon_d d_i^\dagger d_i. \quad (2.51)$$

Position of the two sites in j-th unit cell can be define as, $r = a * j + r_c$ for c-site and for d-site $r = a * j + r_d$ where a is unit cell parameter. Now, considering discrete Fourier transform of this operators and simplifying we can write,

$$\sum_i c_i^\dagger d_i = \sum_k c_k^\dagger d_k e^{ik(r_d - r_c)}, \quad \sum_i d_i^\dagger c_{i+1} = \sum_k d_k^\dagger c_k e^{ik(r_c - r_d)} \quad (2.52)$$

Hence the final Hamiltonian,

$$H = t \sum_k (c_k^\dagger d_k e^{ik(r_d - r_c)} + d_k^\dagger c_k e^{ik(r_c - r_d)} + h.c.) + \sum_k \varepsilon_c c_k^\dagger c_k + \sum_k \varepsilon_d d_k^\dagger d_k. \quad (2.53)$$

which implies,

$$H = \sum_k \begin{pmatrix} c_k^\dagger & d_k^\dagger \end{pmatrix} \begin{pmatrix} \varepsilon_c & 2t \cos(kr_{cd}) \\ 2t \cos(kr_{cd}) & \varepsilon_d \end{pmatrix} \begin{pmatrix} c_k \\ d_k \end{pmatrix}$$

$$H = \sum_k \begin{pmatrix} c_k^\dagger & d_k^\dagger \end{pmatrix} H_k \begin{pmatrix} c_k \\ d_k \end{pmatrix}. \quad (2.54)$$

Therefore for N-sites per unit cell, this H_k will be $N \times N$ matrix and diagonalization of which gives eigenvalues and eigenfunctions.

2.3.3.2 Two body interaction

We now return to our discussion of interacting electrons in second quantized notation.

Two body interaction term can be written as,

$$\hat{h}_2 = \sum_{ijkl} \sum_{\sigma, \sigma'} V_{ijkl} c_{i\sigma}^\dagger c_{j\sigma'}^\dagger c_{k\sigma'} c_{l\sigma}, \quad (2.55)$$

where the interaction parameter,

$$V_{ijkl} = \frac{1}{2} \int \int d\mathbf{r} d\mathbf{r}' \phi_i^\dagger(\mathbf{r}) \phi_j^\dagger(\mathbf{r}') \frac{e^2}{|\mathbf{r} - \mathbf{r}'|} \phi_k(\mathbf{r}') \phi_l(\mathbf{r}). \quad (2.56)$$

Thus the generalized Hamiltonian combining Eq.2.48 and Eq.2.55 in second quantization,

$$H = \sum_{i,\sigma} \epsilon_i c_{i\sigma}^\dagger c_{i\sigma} - \sum_{i,j} \sum_{\sigma} t_{ij} c_{i\sigma}^\dagger c_{j\sigma} + \sum_{ijkl} \sum_{\sigma\sigma'} V_{ijkl} c_{i\sigma}^\dagger c_{j\sigma'}^\dagger c_{k\sigma'} c_{l\sigma}. \quad (2.57)$$

Interaction term V_{ijkl} has two important contributions which can be written in terms of its indices i, j, k and l as :

1. For i=l and j=k, $V_{ijkl} = V_{ijji} \equiv V_{ij}$

is known as direct term which couples with the density operator $\hat{n}_i = \sum_{\sigma} c_{i\sigma}^\dagger c_{i\sigma}$ at different site as,

$$\sum_{i,j} V_{ij} \hat{n}_i \hat{n}_j. \quad (2.58)$$

2. For i=k and j=l, $V_{ijkl} = V_{ijij} \equiv J_{ij}$ is known as exchange term. Using the completeness relation $\sigma_{\alpha\beta} \cdot \sigma_{\gamma\delta} = 2\delta_{\alpha\delta} \delta_{\beta\gamma} - \delta_{\alpha\beta} \delta_{\gamma\delta}$,

$$\sum_{i,j} \sum_{\sigma,\sigma'} V_{ijij} c_{i\sigma}^\dagger c_{j\sigma'}^\dagger c_{i\sigma'} c_{j\sigma} = -2 \sum_{i,j} J_{ij} (\hat{\mathbf{S}}_i \hat{\mathbf{S}}_j + \frac{1}{4} \hat{n}_i \hat{n}_j), \quad (2.59)$$

where $\hat{\mathbf{S}}$ is spin operator.

2.3.4 Hubbard Model

In the atomic limit, the most important interaction considered is the Coulomb interaction term which is maximum between the two electrons residing on the same site(atom). The electrostatic energy of two intra-site electrons which is also known

as onsite Coulomb interaction from Eq.2.55 can be written as

$$\sum_i \sum_{\sigma, \sigma'} V_{iiii} c_{i\sigma}^\dagger c_{i\sigma'}^\dagger c_{i\sigma'} c_{i\sigma} = U \sum_i \hat{n}_{i\uparrow} \hat{n}_{i\downarrow} \quad (2.60)$$

Hence from Eq.2.57

$$H = H_t + H_{int} = \sum_{i, \sigma} \epsilon_i c_{i\sigma}^\dagger c_{i\sigma} - \sum_{i, j} \sum_{\sigma} t_{ij} c_{i\sigma}^\dagger c_{j\sigma} + U \sum_i n_{i\uparrow} n_{i\downarrow}. \quad (2.61)$$

This simple interacting Hamiltonian with the inclusion of onsite Coulomb interaction obeying Pauli's exclusion principle was first introduced by *John Hubbard* [26] in 1963 is known as Hubbard model where $U \equiv V_{iiii}$ is known as Hubbard U . The first term is scaling the local single particle energy which can be put to zero.

Although the simplest, it can substantially capture correlated behavior of electrons in materials leading to multiple facets of magnetism and superconductivity [27, 28, 29]. In general, the inter-site Coulomb interaction is considered to be screened and have a negligible impact however since Coulomb interaction is long range so a proper estimation of U for different system is an important aspect of this model. Depending on the degree of localization of the orbitals in some scenarios it is necessary to include nearest, next nearest Coulomb interactions leading to extended Hubbard model [30].

An exact analytical solution of the Hubbard model in any arbitrary dimension (>1) is yet unsolved. Single band Hubbard model [Eq.2.61] can be solved exactly only in limiting cases where either $U = 0$, which is the non-interacting limit and kinetic energy operator is diagonal in momentum space, or $t = 0$ which implies the atomic limit where all sites are isolated and the interaction term is diagonal on position space like in Wannier basis [30]. Besides this there is another exception based on lattice coordination number (z) where it can be solved exactly for $z=2$ [31] (one dimensional chain)

and $z \rightarrow \infty$ [32]. Thus in any intermediate scenario, various numerical techniques have been evolved in the last few decades such as Lanczos algorithm, auxiliary-field Monte Carlo, density-matrix renormalization group etc [33, 34, 35] to study strongly correlated systems. Also various generalization of Hubbard model such as perturbation theory [36, 37] or Hartree-Fock mean-field [38] are there which converts the many body Hubbard Hamiltonian to effective single particle problem. In this thesis, we will mainly focus on mean-field Hubbard model.

Beyond this extreme conditions ($t=0$ or $U=0$) Hubbard model is studied in strong coupling ($U \gg |t|$) as well as weak coupling ($U \ll |t|$), where the former represents a more correlated behavior than the latter. Physics of low energy states ($< U$) at strong coupling limit can be represented by an effective Hamiltonian obtained from Hubbard model. At strong coupling limit the kinetic energy part can be treated perturbatively leading to the t-J model [30] which at half-filling is same as spin-1/2 Heisenberg model [30, 39]. So, the simplest interaction term of Hubbard model can cover various regimes of model Hamiltonian approach.

2.3.4.1 Mean Field approximation

This is one of the simplest approximation to reduce the complexity of many body Hamiltonian in which all many body interactions are replaced by an effective or mean-field of interactions acting on a single body. According to mean-field approximation [38] all the particle operator (second quantization) can be represented in terms of number fluctuations (δn_i) around the mean value ($\langle n_i \rangle$). Hence,

$$n_{i\sigma} = \langle n_{i\sigma} \rangle + \delta n_{i\sigma}, \sigma = \uparrow, \downarrow. \quad (2.62)$$

and the two body interaction term becomes,

$$\begin{aligned}
Un_{i\uparrow}n_{i\downarrow} &= U(\langle n_{i\uparrow} \rangle + \delta n_{i\uparrow})(\langle n_{i\downarrow} \rangle + \delta n_{i\downarrow}) \\
&= U(\langle n_{i\uparrow} \rangle \langle n_{i\downarrow} \rangle + \langle n_{i\uparrow} \rangle \delta n_{i\downarrow} + \langle n_{i\downarrow} \rangle \delta n_{i\uparrow} + \delta n_{i\uparrow} \delta n_{i\downarrow}).
\end{aligned} \tag{2.63}$$

Within mean-field approximation neglecting the correlation of fluctuations($\delta n_{i\uparrow} \delta n_{i\downarrow}$) and using $\delta n_{i\sigma} = n_{i\sigma} - \langle n_{i\sigma} \rangle$

$$U \sum_i n_{i\uparrow} n_{i\downarrow} = U \sum_i (n_{i\uparrow} \langle n_{i\downarrow} \rangle + n_{i\downarrow} \langle n_{i\uparrow} \rangle - \langle n_{i\uparrow} \rangle \langle n_{i\downarrow} \rangle). \tag{2.64}$$

Therefore after a direct Hartree-Fock decoupling of the interaction term the mean-field Hubbard Hamiltonian(MFH) can be written as a sum of Hamiltonian for two spins(up & down) and a constant term as :

$$\begin{aligned}
H_{MF} &= H_{\uparrow} + H_{\downarrow} + C \\
H_{\uparrow} &= -t \sum_{\langle i,j \rangle} c_{i\uparrow}^{\dagger} c_{j\uparrow} + U \sum_i n_{i\uparrow} \langle n_{i\downarrow} \rangle \\
H_{\downarrow} &= -t \sum_{\langle i,j \rangle} c_{i\downarrow}^{\dagger} c_{j\downarrow} + U \sum_i \langle n_{i\uparrow} \rangle n_{i\downarrow} \\
C &= -U \sum_i \langle n_{i\uparrow} \rangle \langle n_{i\downarrow} \rangle.
\end{aligned} \tag{2.65}$$

Thus the Hubbard Hamiltonian [Eq.2.61] reduces to two matrices of size $N \times N$ (N is no of lattice sites per unit cell) with $2N$ mean-field parameters for up and down densities and Eq.2.65 suggests a self-consistent solution, characteristic of a mean-field approach. An effective decoupling treatment of two spins in mean field approach allows the computation of spin polarized charge densities explicitly in terms of a spatially localized basis. Due to its simplicity, it is easy to add some interaction terms to the MFH model or to study various realistic deformation of the lattices[40].

2.3.4.2 Self-consistent approach

Within mean-field approximation, the Hubbard model Hamiltonian transform into two Hamiltonian for two opposite(up- \uparrow ,down- \downarrow)spin where mean-field term for one of the spin(\uparrow) depends on the average occupation of the opposite spin(\downarrow , $\langle n_{i\downarrow} \rangle$). So to calculate the ground state energy and density, this Hamiltonian need to be solved in a self-consistent way. Starting from an initial guess density of electrons of spin σ ($\langle n_{i\sigma} \rangle$) the following steps are repeated until the convergence criterion set in terms of total energy or density is satisfied [Fig.2.5].

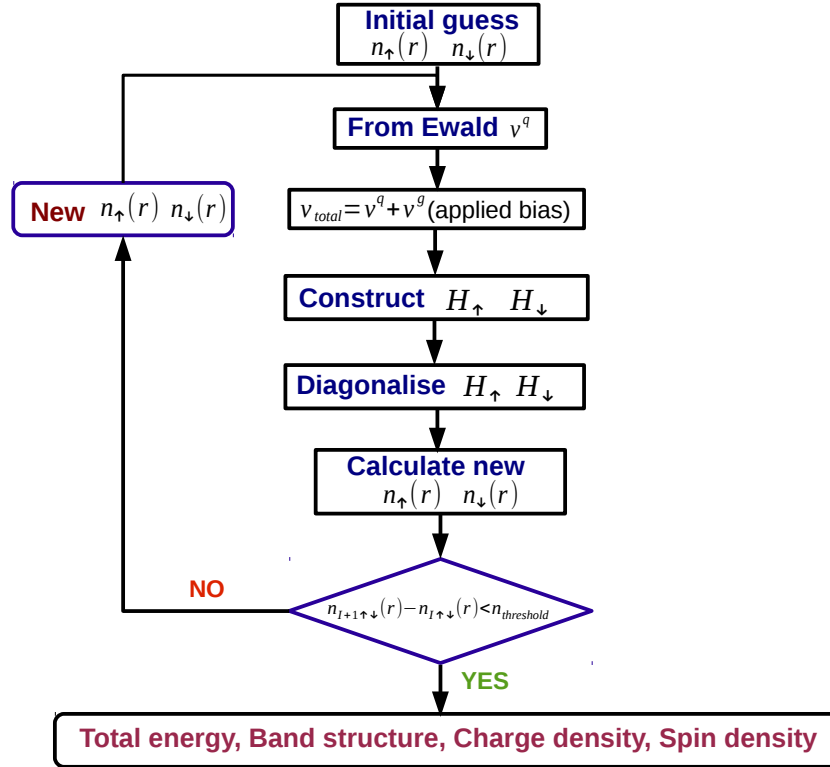


Figure 2.5: Self consistent scheme for mean-field Hubbard model

Fermi energy($\varepsilon_{F\sigma}$) [Eq.2.66] is obtained as

$$\int_{-\infty}^{\infty} D(\varepsilon_{\sigma}) f(\varepsilon_{\sigma} - \varepsilon_{F\sigma}) d\varepsilon_{\sigma} = N_{e\sigma}, \quad (2.66)$$

here $D(\varepsilon)$ is density of states and $f(\varepsilon - \varepsilon_F)$ is Fermi function with Fermi energy ε_F at $T=0$. Average number of particle at each site $i(=j)$ for spin σ is

$$\langle n_{i\sigma} \rangle = \frac{1}{N} \sum_{\mathbf{k}, j} |c_{i,\sigma}^j(\mathbf{k})|^2 f_{\mathbf{k}j\sigma}(\varepsilon_{\mathbf{k}j\sigma} - \varepsilon_{F\sigma}), \quad (2.67)$$

where $c_{i,\sigma}^j(\mathbf{k})$ is weight of the j -th eigen state on i -th site for wave vector \mathbf{k} . For non-magnetic ground state we set $\langle n_\sigma \rangle = \langle n'_\sigma \rangle$, whereas for anti-ferromagnetic ground state we set $\varepsilon_{F\sigma} = \varepsilon_{F'\sigma}$. For ferromagnetic ground state we calculate $\varepsilon_{F\sigma}$ and $\varepsilon_{F'\sigma}$ such that $N_{e\sigma} - N_{e\sigma'}$ is equivalent to net magnetic moment.

A usual problem of convergence is the oscillation of total energy between two successive steps due to sloshing of charge between two regions of the unit cell. The simplest solution is to introduce mixing of charge density or potential of an iteration with one or more previous iterations[41, 42]. Mixing with the previous iteration was sufficient in all our calculations.

2.4 Wannier Function

In the study of various electronic and magnetic properties, localized orbital description similar to ‘localized molecular orbitals’ plays an important role. Analysis of charge density based on various localized descriptors like ‘Mulliken’[43] analysis, ‘Löwdin’[44, 45] analysis, ‘Bader’[46] analysis and most recently electron localization function(ELF)[47] have been evolved. First two approaches are based on projection of extended wave-functions on some localized basis and therefore have marked dependence on the choice of basis whereas the latter one based on separation of charge density into atomic basis through critical point analysis and have been widely used for analysis of bonding, oxidation state, reaction mechanisms and in response

calculation[48].

Like molecular orbital, a set of *localized orthogonal functions* (Wannier functions(WFs))[Fig.2.6] were introduced by Gregory Wannier in 1937[4], which are connected to extended Bloch orbitals by a set of unitary transformations. Wannier functions are one of the powerful representation[49] of localized picture which can be derived from electronic structure. The Wannier centers(WCs), their spatial distribution provide unambiguous partitioning of total charge in atoms and bonds. Even though WFs are non-unique several numerical implementations have been taken up over the years to make spatially localized WFs computationally accessible to the fraternity[49, 50, 51].

Recalling the definition of Wannier function in terms of Bloch function[sec.2.3.1],

$$w_{n\mathbf{R}}(r) = \frac{V}{(2\pi)^3} \int_{BZ} \psi_{n\mathbf{k}}(\mathbf{r}) e^{-i\mathbf{k}\cdot\mathbf{R}} d\mathbf{k}, \quad (2.68)$$

where V is real space primitive cell volume.

The definition of WF is simple, however, due to “gauge freedom,” the construction of WF is not unique[5]. This arises due to arbitrary phases associated with Bloch functions $\psi_{n\mathbf{k}}$ at each \mathbf{k} and hence any unitary transformation can be associated with $\psi_{n\mathbf{k}}$.

$$|\tilde{\psi}_{n\mathbf{k}}\rangle = \sum_{m=1}^N U_{mn}^{(\mathbf{k})} |\psi_{m\mathbf{k}}\rangle, \quad (2.69)$$

and a set of WFs can be constructed with the transformed Bloch function

$$|w_{n\mathbf{R}}\rangle = \frac{V}{(2\pi)^3} \int_{BZ} \sum_{m=1}^N U_{mn}^{(\mathbf{k})} |\psi_{m\mathbf{k}}\rangle e^{-i\mathbf{k}\cdot\mathbf{R}} d\mathbf{k}, \quad (2.70)$$

where $U_{mn}^{(\mathbf{k})}$ is a unitary matrix.

The non-uniqueness in the choice of unitary transformation $U_{mn}^{(\mathbf{k})}$ provide WFs

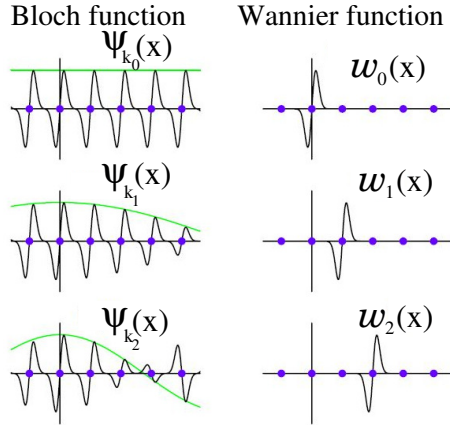


Figure 2.6: Transformation from Bloch functions to WFs. Left: Real-space representation of three of the Bloch functions $e^{ikx}u_k(x)$ associated with a single band in one dimension, for three different values of the wave vector k . Filled circles indicate lattice vectors, and thin (green) lines the envelopes of each Bloch function. Right: WFs associated with the same band, forming periodic images of one another. The two sets of Bloch functions at every k in the Brillouin zone (BZ) and WFs at every lattice vector span the same Hilbert space. Image © Ref. [48]

with various degrees of localization. In principle, smoother the variation of wave functions over the BZ which also implies flatter the corresponding band the more localize would be the WFs and vice versa. In fact, dis-entanglement of bands is the crucial part for the construction of WFs in periodic systems. Indeed in one dimension, a unique choice of $U(k)$ exists which ensures smooth variations of transformed wave functions and their unambiguous band identity throughout the BZ. These transformed wave functions lead to a set of orthogonal WFs having maximum localization in a given direction. Similarly, in higher dimensions a non-unique set of $U(\mathbf{k})$ matrices can be derived to render maximally localized WFs in all directions. In the following, we briefly describe the respective methods.

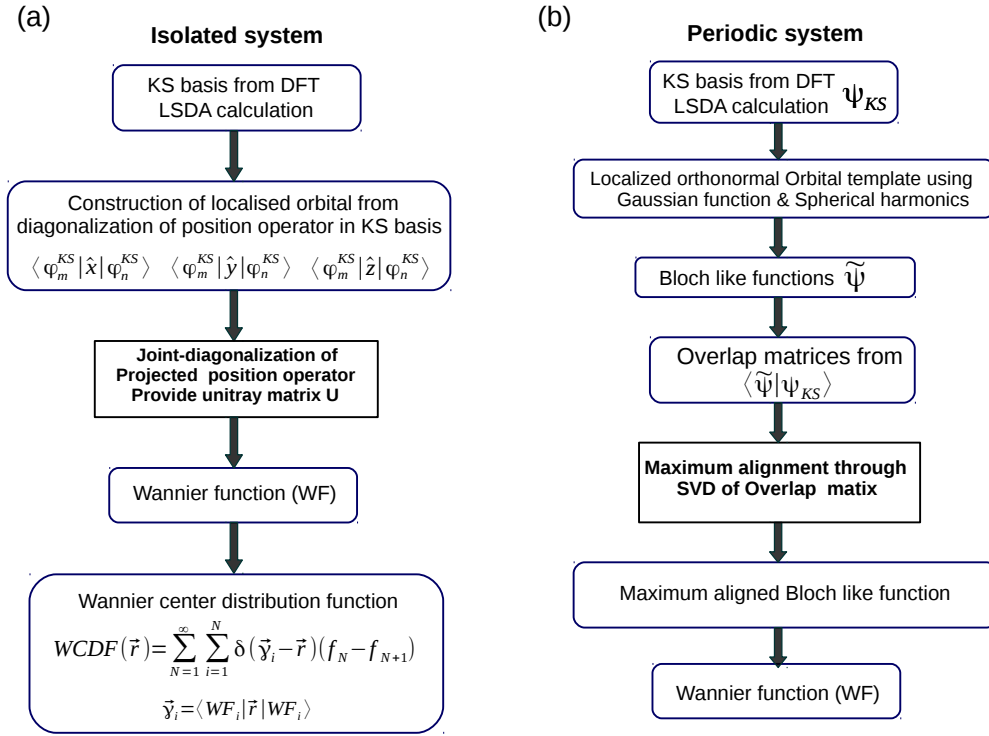


Figure 2.7: Scheme of construction of Wannier function using K-S basis for (a) isolated system and (b) periodic system.

2.4.1 Wannier function from Kohn-Sham basis

For computation of WFs in this thesis we have used the “*Abinit*” [52] code which also uses plane wave basis similar to QE. Our post-processing codes for construction of WFs are interfaced with *Abinit*. Efficient schemes for construction of WFs in higher dimension is nontrivial due to their non-uniqueness rooted at the non-commutative nature of the three position operators projected in the occupied subspace. In my thesis work, I have calculated WFs using two different schemes for isolated and periodic systems as detailed below.

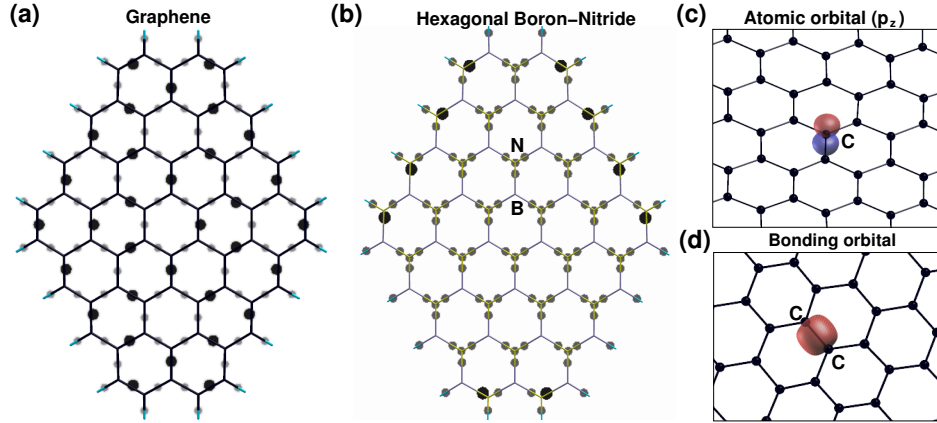


Figure 2.8: Wannier function using K-S basis for isolated system considering a hydrogen passivated finite system of (a)graphene, (b)hexagonal boron nitride and for periodic system representing (c) p_z atomic orbital and (d)bonding orbital for a planar p_z electron system. Big and small circles are equivalent to $2e^-$ and $1e^-$ respectively.

2.4.1.1 Isolated system

We recall from [sec.2.4] that WFs can be understood as linear combinations of Bloch functions which are obtained from first principles as K-S states using DFT. In one dimension the set of WFs which have maximum localization in a given direction, also exclusively diagonalizes the first moment (position operator) along the given direction in the basis of occupied states. Therefore, for the isolated system, such WFs can be readily constructed by diagonalization of position operator for the given direction (e.g. \hat{x}) in the occupied K-S basis $\{\phi_m^{KS}\}$ obtained as,

$$X_{mn} = \langle \phi_m^{KS} | \hat{x} | \phi_n^{KS} \rangle$$

However, since the position operators along three linearly independent directions (X, Y, Z), may not commute within a finite basis set, they can be approximately joint diagonalized to obtain a set of WFs[Fig. 2.7(a)] which maximally diagonalizes their first moments simultaneously and are highly localized in all three dimensions. These

WFs, unlike the maximally localized Wannier function[49], does not depend on any reference template of orbitals to define their symmetries. In this method, the Wannier centers(WCs), which are basically the center of mass of WFs, can be obtained directly from the approximate eigenvalues of the three first moment matrices(FMMs), without explicitly constructing the WFs. Distribution of WCs :

$$\vec{\gamma}_i = \langle WF_i | \vec{r} | WF_i \rangle, \quad (2.71)$$

each of which represents one electron thus facilitates precise estimation of number of electrons associated with bonds and atoms. The position of WCs provides a unique dot structure map for the valence electrons over the entire system cell. Accordingly, for partially occupied bands, we plot *Wannier center distribution function* (WCDF),

$$WCDF(\vec{r}) = \sum_{N=1}^{\infty} \sum_{i=1}^N \delta(\vec{\gamma}_i - \vec{r})(f_N - f_{N+1}), \quad (2.72)$$

where f_N is the occupancy of the N_{th} K-S state, such that

$$\int_{-\infty}^{\infty} WCDF(\vec{r}) d\vec{r} = N_e.$$

N_e is total no of valence electrons.

Based on the location of WCs with respect to atoms, per spin, WCs can be segregated in two categories:(1) atomic WCs(AWC) associated with atoms and (2) bonding WCs (BWC) along the bonds connecting two atoms respectively, at the center of masses of atomic and bonding orbitals. Single and double bonds are represented by one and two WCs between two nearest neighboring atoms, and for ease of representation WCs in close proximity are added up and considered as one big sphere with a radius equivalent to the number of electrons. Mostly in our analysis, it has been

presented either by a sphere or a circle in case of planar projections. From WCs to estimate the net charge (valence electrons) we consider one electron from each AWCs and half of an electron per BWCs. Notably, this counting process is markedly different from any other localized descriptions like Mulliken, Bader or Löwdin analysis. To estimate the level of sub-shell filling we consider one electron per AWC and also one electron per BWC. Thus in this method, the estimation of valence charge and shell filling crucially depends on the identifications of AWCs and BWCs. In covalent and ionic systems this identification is easy and can be automated but in mixed scenarios of covalent and ionic bonding, this identification requires inspection of the WFs. Since this procedure can not be extended for periodic systems, WCs analysis in this method has been done considering an isolated hydrogen passivated patch of the reference system. For graphene island [Fig. 2.8(a)] the big circle corresponds to C=C double bonds, one per atom. In hBN islands [Fig. 2.8(b)] the distribution of WCs towards N-site represents the electronegativity difference between B and N.

2.4.1.2 Periodic system

In periodic systems, the smooth variations of wave functions and preservation of their band identity are ensured by maximally aligning the occupied subspace of K-S States at each \mathbf{k} with an auxiliary set of Bloch like states constructed from a template of localized orbitals as $\{\phi_n(\mathbf{r} - \mathbf{R})\}$:

$$\psi'_{n\mathbf{k}}(\mathbf{r}) = \sum_{\mathbf{R}} e^{i\mathbf{k}\cdot\mathbf{R}} \phi_n(\mathbf{r} - \mathbf{R}). \quad (2.73)$$

Maximum alignment is ensured by demanding hermiticity of the overlap between ψ_{KS} and ψ' , which is achieved through singular value decomposition (SVD) of the overlap matrices at each \mathbf{k} . WFs are constructed using these aligned Bloch functions

which are spatially localized in all directions[Fig.2.7(b)]. Although these WFs are spatially localized they do not guarantee the maximal localization, nevertheless, they reveal the orbital nature of electronic structure leading to unambiguous partitioning of atomic and bonding orbitals[Fig.2.8(c,d)].

Bibliography

- [1] W. Kohn, L. J. Sham, *Physical Review*, 140(4A), (1965).
- [2] Oleg V Yazyev, *Reports on Progress in Physics*, 73(5), (2010).
- [3] Hélène Feldner *et al.*, *Phys. Rev. B*, 81, 115416, (2010).
- [4] Gregory H. Wannier, *Physical Review*, 52, (1937).
- [5] W. Kohn, *Phys. Rev.*, 115.809, (1959).
- [6] P. Hohenberg, W. Kohn, *Phys. Rev.*, 136, B864, (1964).
- [7] W. Kohn, L. J. Sham, *Phys. Rev.*, 140, A1133, (1965).
- [8] Roger Fletcher, *Practical methods of optimization (2nd ed.)*, New York: John Wiley & Sons, ISBN 978-0-471-91547-8, (1987).
- [9] F.D. Murnaghan, *Proceedings of the National Academy of Sciences of the United States of America*, 30, (1944).
- [10] Robert G. Parr, Yang Weitao, *Density-Functional Theory of Atoms and Molecules*, Oxford University Press, (1994).
- [11] R. M. Martin, *Electronic structure: basic theory and practical methods*, Cambridge University Press, (2004).

- [12] Eberhard Engel, Reiner M. Dreizler, *Density Functional Theory: An Advanced Course*, Springer Science & Business Media, **(2011)**.
- [13] D. R. Hamann, M. Schlüter, and C. Chiang, *Phys. Rev. Lett.*, 43, 1494, **(1979)**.
- [14] D. Vanderbilt, *Phys. Rev. B*, 41, 7892, **(1990)**.
- [15] P. Giannozzi *et al.*, “QUANTUM ESPRESSO: a modular and open-source software project for quantum simulations of materials”, *J. Phys. Cond. Mat.*, 21, 395502, **(2009)**.
- [16] N. W. Ashcroft and D. N. Mermin, *Solid State Physics*, Brooks/Cole Thomson Learning, Toronto, **(1976)**.
- [17] Stefano Baroni, Stefano de Gironcoli, Andrea Dal Corso and Paolo Giannozzi, *Rev. Mod. Phys.*, 73, 515, **(2001)**.
- [18] E. R. Johnson, I. D. Mackie, G. A. DiLabio, *J. Phys. Org. Chem.*, 22, 1127, **(2009)**.
- [19] F. London, *The general theory of molecular forces*, Transactions of the Faraday Society, 33, **(1937)**.
- [20] A. Tkatchenko and M. Scheffler, *Phys. Rev. Lett.*, 102, 073005, **(2009)**.
- [21] S. Grimme, *J. Comput. Chem.*, 25, **(2004)**.
- [22] S. Grimme, *J. Comput. Chem.*, 27, **(2006)**.
- [23] S. Grimme, J. Antony, S. Ehrlich, H. Krieg, *J. Chem. Phys.*, 132, 154104, **(2010)**.
- [24] Stefan Grimme, *John Wiley & Sons, Ltd. WIREs, Comput. Mol. Sci.*1, 211, **(2011)**.

- [25] J. C. Slater and G. F. Koster, *Phys. Rev.*, 94, 1498, **(1954)**.
- [26] J. Hubbard, *Proceedings of the Royal Society of London.*, 276(1365), **(1963)**.
- [27] A. Mielke & H. Tasaki, *Commun. Math. Phys.*, 158: 341, **(1993)**.
- [28] Masatoshi Imada, Atsushi Fujimori, and Yoshinori Tokura, *Rev. Mod. Phys.* 70, 1039, **(1998)**.
- [29] P. B. Wiegmann, *Phys. Rev. Lett.* 60, 2445, **(1988)**.
- [30] Patrick Fazekas, *Series in Modern Condensed Matter Physics: Volume 5, Lecture Notes on Electron Correlation and Magnetism*, world Scientific, **(1999)**.
- [31] F. H. L. Essler, H. Frahm, F. Göhmann, A. Klümper, and V. E. Korepin, Cambridge University Press, Cambridge, 17, 152, **(2005)**.
- [32] A. Georges and G. Kotliar, *Phys. Rev. B*, 45, 6479, **(1992)**.
- [33] Z. Bai, J. Demmel, J. Dongarra, A. Ruhe and H. A. Van der Vorst, SIAM, Philadelphia, PA, USA, **(2000)**.
- [34] W. M. C. Foulkes, L. Mitas, R. J. Needs, and G. Rajagopal, *Rev. Mod. Phys.* 73, 33, **(2001)**.
- [35] S. R. White, *Phys. Rev. B*, 48, 10345, **(1993)**.
- [36] H. J. Schulz, *Phys. Rev. Lett.*, 64, 2831, **(1990)**.
- [37] D. Sénéchal, D. Perez, and M. Pioro-Ladrière, *Phys. Rev. Lett.*, 84, 522, **(2000)**.
- [38] V. Bach, E. H. Lieb, J. P. Solovej, *Journal of Statistical Physics*, 76:3, **(1994)**.
- [39] Charles L. Cleveland and Rodrigo Medina A., *American Journal of Physics*, 44, **(1976)**.

- [40] The Hubbard Model: Recent Results, Volume 7 of Series On Advances In Statistical Mechanics, World Scientific, (1991).
- [41] E. Wimmer, H. Krakauer, M. Weinert, A. J. Freeman, *Phys. Rev. B*, 24, 864, (1981).
- [42] D. D. Johnson, *Phys. Rev. B*, 38, 12807, (1988).
- [43] R. S. Mulliken, *The Journal of Chemical Physics*, 23(10), (1955).
- [44] P.-O. Löwdin, *J. Chem. Phys.*, 18, 365, (1950).
- [45] P.-O. Löwdin, *Adv. Quantum Chem*, 5, 185, (1970).
- [46] R. F. W. Bader, *Chem. Rev.*, 91, 893, (1991).
- [47] A. D. Becke and K. E. Edgecombe, *J. Chem. Phys.*, 92(9), (1990).
- [48] N. Marzari, D. Vanderbilt *et al.*, *Reviews of modern physics*, 84, (2012).
- [49] N. Marzari and D. Vanderbilt, *Physical Review B*, 56(20), (1997).
- [50] J. Bhattacharjee, U. V. Waghmare, *Phys. Rev. B*, 71, 045106, (2005).
- [51] J. Bhattacharjee, U. V. Waghmare, *Phys. rev. B (R)*, 73, (2006).
- [52] X. Gonze *et al.* “First-principles computation of material properties: the ABINIT software project”, *Comput. Mater. Sci.*, 25, (2002).

Chapter 3

Electronic and magnetic properties of 2p-block elements in low dimension

3.1 Introduction

With the advent of advance synthesis techniques isolation of single layer of graphene from their bulk structure have reinforced the foundation of research on two dimensional(2D) materials in general. The family of 2D materials have a wide range of selectivity of elements from periodic table[1, 2] and depending on their composition and structure drives a wide variety of electronic and magnetic properties, although here we will mainly focus on 2p-block elements.

The goal of this chapter is to present a brief outline of electronic and magnetic properties of some of the most well known monolayers made of the 2p-block elements, primarily graphene and quasi one dimensional(1D) structure derived from it, namely graphene nanoribbons, followed by brief discussion on similar 2D and 1D structures

made of boron(B), carbon(c) and nitrogen(N). In this chapter we have also discussed briefly about the mechanism of magnetic ordering observed in these systems exclusively due to p-electrons, which is a key aspect dealt with extensively in this thesis.

3.1.1 Graphene

Graphene is a monolayer of sp^2 hybridized carbon(C) atoms in honeycomb lattice. The strong covalent bonds made by the sp^2 orbitals of carbon makes graphene mechanically robust and resilient. The unhybridized $2p_z$ orbitals delocalize in the lattice in order to reduce kinetic energy, leading to π conjugation which adds to the mechanical resilient and renders graphene chemically inert despite having unpaired electrons. However, the delocalization of p_z electron in honeycomb lattice leads to semi-metallic band structure and extra ordinarily high mobility of electrons which has rendered graphene as one of the most promising material for fabrication of electronic devices at nanoscale. With the valence and conduction band edges described by a single p_z electron per site the electronic structure of graphene and related graphenic systems are well represented within a single orbital TB framework[3].

The honeycomb lattice of graphene consists of a primitive cell with two atom basis, where n-n sites belong to opposite triangular sub-lattices(A,B) implying bipartite symmetry, as shown in Fig.3.1(a). For two atom unit cell, recalling [Eq.2.54], we can write

$$H_{\mathbf{k}}^{ij} = t(1 + e^{i\mathbf{k}\cdot\boldsymbol{\delta}_1} + e^{i\mathbf{k}\cdot\boldsymbol{\delta}_2}) \equiv t\gamma_{\mathbf{k}}, \quad (3.1)$$

where t is n-n hopping amplitude and $\boldsymbol{\delta}_1, \boldsymbol{\delta}_2$ are lattice vectors as shown in Fig.3.1(a).

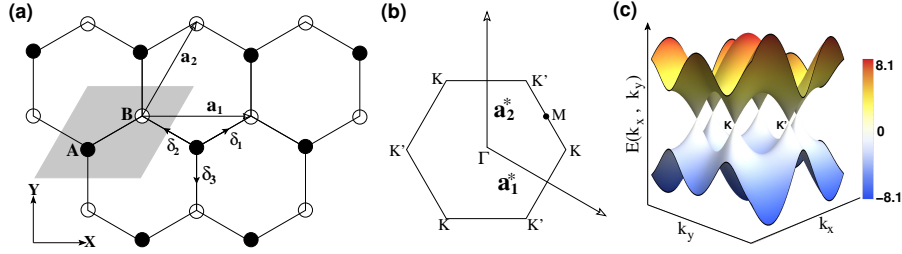


Figure 3.1: (a) Representation of bipartite Graphene with two sub-lattices A (filled circle) and B (hollow circle), real space basis vectors \vec{a}_1 , \vec{a}_2 and the vectors $(\vec{\delta}_1, \vec{\delta}_2, \vec{\delta}_3)$ connecting nearest neighbor site. shaded region corresponds to primitive cell of bipartite lattice. (b) First Brillouin Zone with reciprocal lattice vectors \vec{a}_1^* , \vec{a}_2^* Dirac point K, K' and high symmetry k-point Γ and M. (c) Band structure of graphene using Eq. 3.4 with $t = -2.7$ eV.

Hence, from secular equation

$$\det \begin{bmatrix} 0 - E_{\mathbf{k}} & t\gamma_{\mathbf{k}}^* \\ t\gamma_{\mathbf{k}} & 0 - E_{\mathbf{k}} \end{bmatrix} = 0. \quad (3.2)$$

The dispersion relation,

$$E_{\mathbf{k}} = \pm t |\gamma_{\mathbf{k}}|, \quad (3.3)$$

putting, $\delta_1 = \frac{a}{2} (\sqrt{3}, 1)$, $\delta_2 = \frac{a}{2} (-\sqrt{3}, 1)$ [Fig. 3.1(a)] and after simplification,

$$E(k_x, k_y) = \pm t \left[1 + 4\cos\left(\sqrt{3}k_x \frac{a}{2}\right) \cos\left(k_y \frac{a}{2}\right) + 4\cos^2\left(k_y \frac{a}{2}\right) \right]^{\frac{1}{2}}. \quad (3.4)$$

Here, \pm sign represents two energy band, (+) corresponds to conduction band $[\pi^*]$ and (-) corresponds to valence band $[\pi]$ [Fig. 3.1(c)]. Since each C atom contribute one π electron and spin-up or spin-down state each can occupy an electron, the lower band is completely filled and the upper band is completely empty, so the Fermi level is at the energy where both the band (π , π^*) touches. Thus pristine graphene shows a semi-metallic density of states with zero gap. The set of k-points for which $E_{\mathbf{k}}=0$ can

be calculated using Eq.3.1. There are six such points around the Γ point constituting a hexagon. Among these only two are inequivalent points (K and K')[Fig.3.1(b,c)], where the rest all are connected through reciprocal lattice vectors to the inequivalent points. These special points are known as Dirac point because at continuum limit the linearization of energy dispersion[Eq.3.4] around this sets of k-points gives linear dispersion relation and the Hamiltonian resembles [4] Dirac Hamiltonian. However, it is known that the quasi particle nature of electrons and spin-orbit coupling leads to a negligibly yet non zero small gap around Fermi energy.

3.1.2 Graphene Nanoribbon

Graphene nanoribbon(GNR), a quasi 2D periodic structure of graphene which is periodic in one dimension and confined on the other. Depending on edge configurations there are two types of GNRs, armchair graphene nanoribbon(AGNR) and zigzag graphene nanoribbon(ZGNR). The width of AGNR(ZGNR) has been defined by $N_A(N_Z)$ counted along the zigzag(dimer) lines[Fig.3.2(a)]. Effect of width and edge configurations in electronic structure can be understood from single orbital(π) TB model. Depending on width, AGNRs shows metallic band structure [Fig.3.2(b): $N_A=5$] if $N_A=3m+2$, where m is a positive integer, otherwise it is semiconducting [Fig.3.2(b): $N_A=10$] and gap decreases with increasing N_A [5, 6]. In GNRs, the confinement along one direction restricts the allowed k-values of the graphene band structure and hence if the lines passes through the special k-points(K, K') will be metallic [7]. The degree of band gap opening is largely influenced by widths and the edge geometry [6].

Within TB framework ZGNRs shows metallic band structure[Fig.3.2(d)] irrespective of their ribbon widths. The valence and conduction bands are degenerate near $k=\pi$ (X-here) and this flat region of bands extends within a region of $2\pi/3 \leq |k| \leq \pi$. These partial flat bands are due to the presence of localized states at the two edges

that belongs to opposite sub-lattices A and B as shown in Fig.3.2(e). However note that two zigzag edges are made of two different sub lattices. This sub-lattice asymmetry hinders π conjugation and leads to spin separation between the two sub-lattices with introduction of on-site Coulomb repulsion term U as per Hubbard model[8]. The gap appears due to an effective difference in on-site term for two n-n sites for each of the spins. This spin separation intensifies near the edges leading to n-n FEM order at the edges and AFM order between the two edges. Such appearance of gap and spin separation is also observed from first principles calculations within LSDA. Bipartite lattices are known to have particle-hole symmetry within Hubbard model, e.g. in pristine graphene. However, with the introduction of inequivalence between the sub-lattices, e.g. at the edges of zigzag graphene nanoribbon, the inhomogeneities of the effective onsite term across the ribbon for each spin leads to broken particle-hole symmetry. Such opening of band gap due to localised magnetic ordering [Fig.3.2(f)] rooted at sub-lattice asymmetry is the unique feature of zigzag edges which are absent in armchair edges[Fig.3.2(c)] due to symmetry of the two sub-lattices.

3.2 p-electron driven magnetism in graphenic systems

Electronic structure three coordinated bipartite systems at half-filling with one $2p_z$ electron per atom, is determined primarily by the competition between inter-sub-lattice delocalization in order to reduce kinetic energy, and inter-sub-lattice spin separation, which reduces Coulomb potential energy of occupied orbitals. Both these two factors can be undermined by localization of electron in one of the sub-lattices in case the two sub-lattices have different onsite terms, e.g. in hBN sheet. In pristine graphene the lowering in kinetic energy due to delocalization is more than the

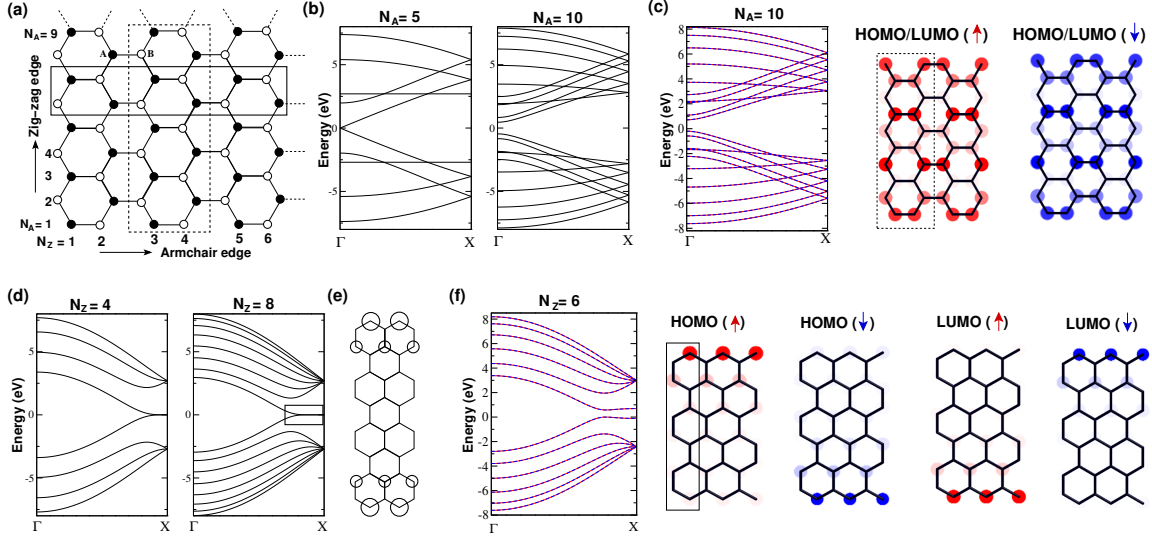


Figure 3.2: (a) Representation of graphene nanoribbon for zigzag and armchair edges with periodic direction and unit cell as shown by solid and dotted rectangle respectively for ZGNR and AGNR. Band structure from TB model with various width of (b) AGNR for $N_A=5$ and $N_A=10$ and (d) ZGNR for $N_Z=4$ and $N_Z=8$. (e) Charge density for a selected region of $N_Z=8$. Band structure and density profile for HOMO and LUMO from mean-field Hubbard model for (c) AGNR for $N_A=10$, (f) ZGNR for $N_Z=6$.

increase of Coulomb potential in the process leading to a non-magnetic semi-metallic ground state as discussed in previous section. In pristine hBN the localization due to the large difference of electronegativities of B and N leads to non-magnetic insulating ground state. However, with modest levels of inequality between the two sub-lattices, e.g. physical or chemical modifications which dissimilarly effects the two sub-lattices, the inter sub-lattice delocalization is hampered, which opens scopes for the inter sub-lattice spin separation to consolidate, leading to nearest-neighbor ferromagnetic ordering in the ground state in the vicinity of modifications and a net magnetic moment. This is a key mechanism responsible for magnetism in graphenic systems reported in a large body of work accumulating in literature over the last two decades or so. For example, existence of robust and tunable magnetic ordering [9, 10]

have been explored through chemical functionalization at edges [11, 12, 13], application of electric field [14] across ribbons, substitution with different elements or with adatom, defects [15, 16, 17, 18, 19, 20, 21, 22, 23] etc.

The onset of magnetism in these weakly correlated systems is traditionally understood in terms of Hubbard model, where the on-site Coulomb interaction between the electrons of different spins is exclusively the source of correlation. Mott transition has been shown to be possible in honeycomb lattices for $U/|t| > 4$ [24], whereas in pristine graphene $U/t \simeq 1$ leads to a non-magnetic ground state as discussed above. However, due to sub-lattice asymmetry a Mott like spin separation between sub-lattices emerges with $U > 0$ [25] as seen in zigzag edged graphene nanoribbons and tubes.

3.2.1 Ferromagnetism in bipartite system

Nearest neighbor FM ordering in bipartite systems is rare in general. Within the framework of Hubbard model [26], which provides a comprehensive description of magnetism sourced at Coulomb correlation among itinerant electrons, primarily two classes of mechanisms have been proposed to rationalize n-n FM ordering in bipartite systems [27]. It was shown by Nagaoka [28] that with $U \rightarrow \infty$, upon doping by a single hole the ground state will have FM ordering in an attempt to reduce the kinetic energy of the hole while avoiding the double occupancy of a site. However, Nagaoka-FM is not relevant in honeycomb lattices [25], as they do not satisfy the criteria of loop connectivity [28] for Nagaoka-FM to sustain. Although, to comment on whether the Nagaoka mechanism will be effective in ribbons particularly with enhanced correlation due to bias induced confinement, is beyond the scope of my work since it will involve a more careful consideration of correlation effect possible beyond the scope of first principles and mean-field Hubbard model used in this thesis.

The other class of mechanism is proposed to be exchange interaction driven, but possible only in presence of a flat or nearly flat band [29, 30] at Fermi energy so that such a band can accommodate electrons emptied from the doubly occupied states below. The contribution of itinerant electrons have also been argued [31] to mediate exchange interaction nucleating at the flat bands.

However, on one hand the Nagaoka mechanism has been generalized to fractional doping [29], while on the other hand the flat band based mechanisms has also been generalized to nearly flat and partially occupied bands [30]. Thus a simpler general requirement for existence of nn FM order appears to converge from the two mechanisms to high U and nonzero density of states at Fermi energy, as also given by the Stoner Criteria. An important approach for description of FM ordering understood within mean-field approximation is the Stoner criteria [32] which can thus be understood as meeting ground between Nagaoka and flat band mechanisms. Stoner criteria suggests a high U and a finite density of states at Fermi energy as a necessary criterion for the unequal number of two spins to be energetically favorable.

Bibliography

- [1] Pere Miró, Martha Audiffred and Thomas Heine, *Chem. Soc. Rev.*, 43, **(2014)**.
- [2] Ganesh R. Bhimanapati *et al.*, *ACS Nano*, 9, 12, **(2015)**.
- [3] P. R. Wallace, *Phys. Rev.*, (71)622, **(1947)**.
- [4] A. H. Castro Neto, F. Guinea, N. M. R. Peres, K. S. Novoselov, and A. K. Geim, *Reviews of Modern Physics*, (81)109, **(2009)**.
- [5] K. Nakada, M. Fujita, G. Dresselhaus, and M. S. Dresselhaus, *Physical Review B*, (54)17954, **(1996)**.
- [6] Young-Woo Son, Marvin L. Cohen, and Steven G. Louie, *Phys. Rev. Lett.*, (97)216803, **(2006)**.
- [7] Katsunori Wakabayashi, Ken-ichi Sasaki, Takeshi Nakanishi and Toshiaki Enoki, *Sci. Technol. Adv. Mater.*, (11)054504, **(2010)**.
- [8] M. Fujita, K. Wakabayashi, K. Nakada, and K. Kusakabe, *J. Phys. Soc. Jpn.*, (65)1920, **(1996)**.
- [9] Zhuhua Zhang, Changfeng Chen, and Wanlin Guo, *Phys. Rev. Lett.* 103, 187204, **(2009)**.
- [10] Yeonsig Nam, Daeheum Cho, Jin Yong Lee, *J. Phys. Chem. C*, 120, 20, **(2016)**.

- [11] K. Wakabayashi, M. Fujita, H. Ajiki, & M. Sigrist, *Phys. Rev. B*, 59, (1999).
- [12] Hosik Lee, Young-Woo Son, Noejung Park, Seungwu Han, and Jaejun Yu, *Phys. Rev. B*, 72, 174431, (2005).
- [13] Daeheum Cho, Kyoung Chul Ko, Heesoo Park, and Jin Yong Lee, *Journal of Physical Chemistry C*, 119 (18), (2015).
- [14] Young-Woo Son, Marvin L. Cohen & Steven G. Louie, *Nature*, 444, (2006).
- [15] Yafei Li, Zhen Zhou, Panwen Shen, Zhongfang Chen, *ACS Nano*, 3, 7, (2009).
- [16] J. J. Palacios, J. Fernández-Rossier, and L. Brey, *Phys. Rev. B*, 77, 195428, (2008).
- [17] Min Kan, Jian Zhou, Qiang Sun, Qian Wang, Yoshiyuki Kawazoe, and Puru Jena, *Phys. Rev. B*, 85, 155450, (2012).
- [18] Erjun Kan *et al.*, *Appl. Phys. Lett.*, 96, 102503 (2010).
- [19] D. W. Boukhvalov, M. I. Katsnelson, *Nano Lett.*, 8, 12, (2008).
- [20] A. H. Castro Neto *et al.* *Solid State Communications*, 149, 1094, (2009).
- [21] O. V. Yazyev, & L. Helm, *Phys. Rev. B*, 75, 125408, (2007).
- [22] P. O. Lehtinen, A. S. Foster, Yuchen Ma, A. V. Krasheninnikov, and R. M. Nieminen, *Phys. Rev. Lett.*, 93, 187202, (2004).
- [23] Pablo Esquinazi *et al.*, *IEEE Transactions on Magnetism*, 49(8), (2013).
- [24] S. Sorella and E. Tosatti *Europhys. Lett.*, 19(8), (1992).
- [25] Patrick Fazekas, Series in Modern Condensed Matter Physics - Vol.5 {5 Toh Tuck Link, Singapore 596224, World Scientific Publishing Co. Pte. Ltd. (1999).

- [26] J. Hubbard, *Proc. R. Soc. London A* (276)238, **(1963)**.
- [27] J. C. Amadon and J. E. Hirsch, *Phys. Rev. B*, (54)6364, **(1996)**.
- [28] Y. Nagaoka, *Phys. Rev.* 147, 392**(1966)**; H. Tasaki *Phys. Rev. B*, (40)9192, **(1989)**.
- [29] A. Mielke and H. Tasaki, *Commun. Math. Phys.*, (158)341, **(1993)**.
- [30] H. Tasaki, *Prog. Theor. Phys.* (99)489, **(1998)**.
- [31] H.-H. Lin, T. Hikihara, H.-T. Jeng, B.-L. Huang, C.-Y. Mou, and X. Hu, *Phys. Rev. B*, (79)035405, **(2009)**.
- [32] E. Stoner *Proc. R. Soc. London, Ser.A*, (165)372, **(1938)**.

Chapter 4

Partial Bias Induced Magnetism

4.1 Introduction

The different network structures of sp^2 hybridized carbon atoms such as graphene sheet, graphene nanoribbon(GNR), and carbon nanotube shows different electronic properties depending on their shape, size and symmetry in their pristine configuration [1]. The addition of spin selectivity in these systems opens up a new scopes of magnetism beyond the traditional d-electron based magnetism in transition metals.

In pristine bipartite systems the existence of magnetism has been discussed either at strong coupling limit where the strength of on-site Coulomb correlation(U) is dominant over the kinetic energy or at moderate coupling($U \sim t$) [sec. 2.3.4] due to inequivalence of sub-lattices [2] leading respectively to nearest neighbor(n-n) anti-ferromagnetic(AFM) [3, 4, 5] and ferrimagnetic(FEM) ordering. As a source of inequivalence a large variety of possibilities have been proposed through structural [6, 7, 8] and physical [9, 10, 11] or chemical [12, 13, 14, 15, 16] functionalization, leading to scopes for band gap tuning, half-metallicity and magnetism exclusively due to p_z electron.

In this chapter, we will focus on evolution of electronic and magnetic properties due to inhomogeneous application of bias in sheets and islands of graphene and graphene nanoribbons. First I describe electronic structure of inhomogeneously biased armchair graphene nanoribbons and zigzag graphene nanoribbon demonstrating the emergence on n-n FM order at moderate coupling followed by explanation of observed results through simple model.

4.2 Inhomogeneous bias on graphene nanoribbon

In my thesis spin-polarized electronic structure for AGNRs and ZGNRs have been primarily calculated from mean-field Hubbard model which we recall from [sec.2.3.4.1] as

$$H = t \left(\sum_{\langle i,j \rangle, \sigma} c_{i,\sigma}^\dagger c_{j,\sigma} + h.c \right) + \sum_{i,\sigma} c_{i,\sigma}^\dagger c_{i,\sigma} (U \langle n_{i,\sigma'} \rangle - V_g^i + V_q^i), \quad (4.1)$$

where, $\langle n_{i,\sigma'} \rangle$ is the population of electron with spin- σ at the i -th site, U is the strength on-site Coulomb repulsion, V_g^i is the gate bias and nearest neighbor(n-n) hopping amplitude $t = -2.7eV$ [17]. Coulomb repulsion V_q^i at nearest neighboring sites and beyond is calculated using the Ewald summation scheme [18, 19]. A self-consistent computation [sec.2.3.4.2] of Eq.4.1 describes the electronic structure of the system. To probe the nature of magnetic ordering as a function of applied bias V_g and the parameter U , we define the average n-n spin correlation as:

$$S = \frac{1}{N_s} \sum_i^{N_s} \frac{1}{nn_i} \sum_j^{nn_i} S_i S_j, \quad (4.2)$$

where N_s is the number of sites per unit cell, nn_i is the number of n-n sites around the i -th site, and $S_i = \langle n_{i,\sigma} \rangle - \langle n_{i,\sigma'} \rangle$ as obtained from converged self-consistent calculation for each set of V_g and U . The positive and negative values of spin correlation function

S thus represents the existence of either n-n FM or n-n AFM or FEM ordering respectively.

4.2.1 Inhomogeneously biased armchair graphene nanoribbon

As a function of bias(V_g) and the strength of on-site Coulomb repulsion, the positive and negative part of the spin correlation function(S) for AGNRs, as shown in Fig.4.1, implies the existence of n-n FM order at moderate coupling and separation of regions with FM and FEM ordering primarily in regions with and without positive bias respectively. Fig.4.1(a-f) imply rapid consolidation of AFM(FM) ordering above $U \sim 2|t|$ with zero(positive) V_g . For $V_g = 0$ this resembles a Mott like transition [20] at half-filling. With increasing V_g the transition from non-magnetic to the FM ordered ground state happens with increasing U . This trend is similar to the observed non-magnetic to AFM transition in bipartite lattices with deviation from half-filling. The latter is understood in terms of the additional correlation required to dominate over the kinetic energy of the excess charges upon deviation from half-filling. The similarity in trend is expected since with non-zero V_g the biased and unbiased regions both deviate locally from half-filling. This systematic variation of S is impacted by the width of the biased region. Narrow bias towards the AGNR edge[Fig.4.1(a,d)]is more preferable for n-n FM order at moderate coupling since it further enhances localization of charge which is inherently more at the edges than the bulk. FM ordering quenches rapidly in AGNRs [Fig.4.1(b,c,e,f)] as the biased region moves away from the edges or are widened and it requires either high U or V_g for emergence of FM ordering.

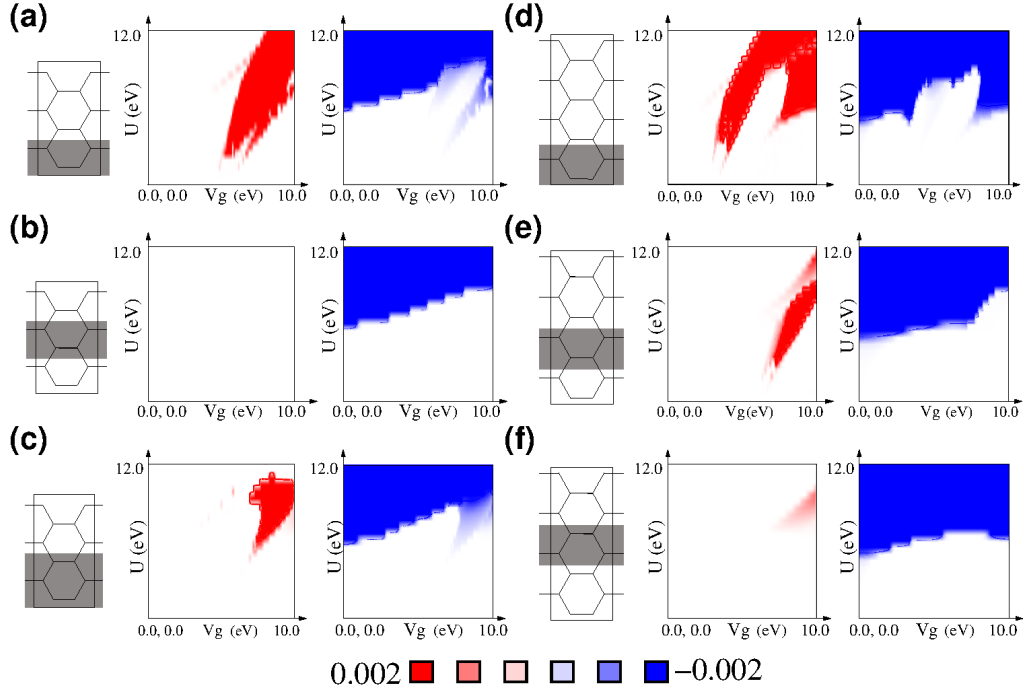


Figure 4.1: spin-correlation(positive & negative) plot as a function of U & V_g for different bias coverages: AGNR($N_A=6$)(a,b,c); AGNR($N_A=8$)(d,e,f). Here gray shade represents the bias coverage

4.2.1.1 Indirect band gap

For AGNRs, the n-n FM ordering is prefaced by band gap tuning and direct to indirect transition as shown in Fig.4.2(a-c). With increasing V_g the bands(bonding and anti-bonding orbitals both) which corresponds to the biased region will become lower in energy, while their counterparts which are far from the biased region will have least change in energies. This leads to a net reduction in band gap since the energy of conduction band edge of the biased region lowers with respect to the valence band edge of the unbiased region. In such a scenario an indirect band gap is natural to expect since the valence and conduction band edges have similar energies but are contributed by electrons at regions of different potential energies which is compensated by difference in their kinetic energies as reflected by different \mathbf{k} at valence band

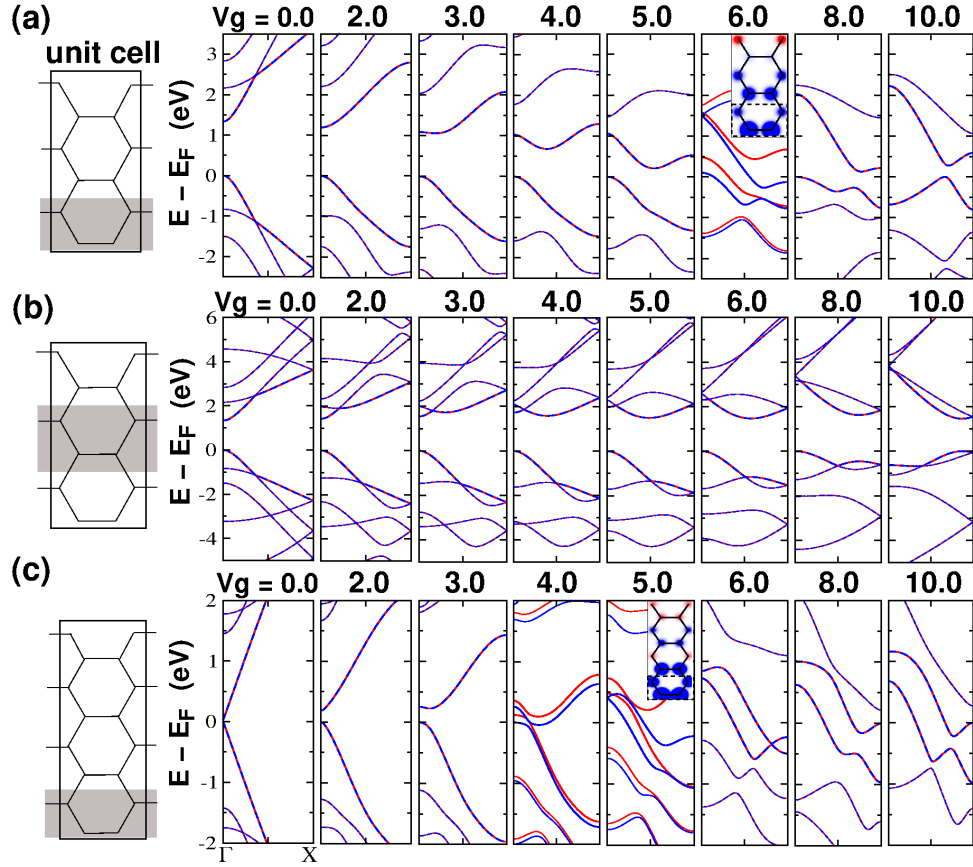


Figure 4.2: Band structure and spin density(inset) from mean-field Hubbard model at $U=4.0$ eV for different gate voltages V_g with different bias coverage of AGNR: (a,b) $N_A=6$ and (c) $N_A=9$. Here gray shade represents the biased region

maxima and conduction band minima.

4.2.1.2 Metallic phases

With increasing V_g , further lowering of the conduction band edge in the biased region finally leads to a closure of indirect gap. Consolidation of one spin over the other due to appearance of n-n FM order within the biased region, inherently implies the lifting of spin degeneracy[Fig 4.2(a,c)] of the band structure in conjunction with narrowing indirect band gap as discussed above. Therefore it is natural to expect emergence of FM-semiconducting or FM-metallic or half-metallic phases accompanying n-n FM

order. We find AGNRs with n-n FM order to be metallic in general[Fig.4.2(a,c)] although in some cases half-metallic windows can also be present.

As the biased region moves from the edge towards the middle(bulk) the localization at the biased region weakens which suppresses the n-n FM order to emerge, nevertheless the direct to indirect transition still occur and band gap remain largely preserved[Fig.4.2(b)].

4.2.2 Inhomogeneously biased zigzag graphene nanoribbon

In ZGNRs, due to the contest between inherent inter-edge AFM ordering and bias induced n-n FM ordering, the influence of n-n FM ordering is rich in comparison to AGNRs. As we explain below, the contest leads to consolidation of one spin and suppression of the other spin from the edges, leading systematic emergence of window of half-metallic transport. For ZGNRs, with finite U at $V_g=0$ the spin correlation function S [Eq.4.2] shows FEM order[Fig.4.3(a-f)] between the two sub-lattices near each of the edges[Fig.4.4(a-d)]. However, with application of $V_g (>0)$ [Fig.4.3(a-f)] quenching of magnetic ordering is observed in ZGNRs below a threshold value of U , which increases with increasing V_g . This can be understood by noting that, since occupation of biased sites($V_g >0$) is favored by electrons with both the spins, they would require a higher U to separate between the sub-lattices. The onset of positive spin correlation, implying n-n FM ordering, enhances if bias region located near any of the edges[Fig.4.3(b,c)] as seen in AGNRs also. The emergence of n-n FM order is much prominent if the biased region cover zigzag C-C chains parallel to the edges[Fig.4.3(a-c)]. Notably, the spin of the n-n FM ordering at those biased sites would prefer the same spin at the edge sites as well due to n-n FEM ordering in the intervening region. Therefore for the zigzag biased sites[Fig.4.4(c)] mixing of

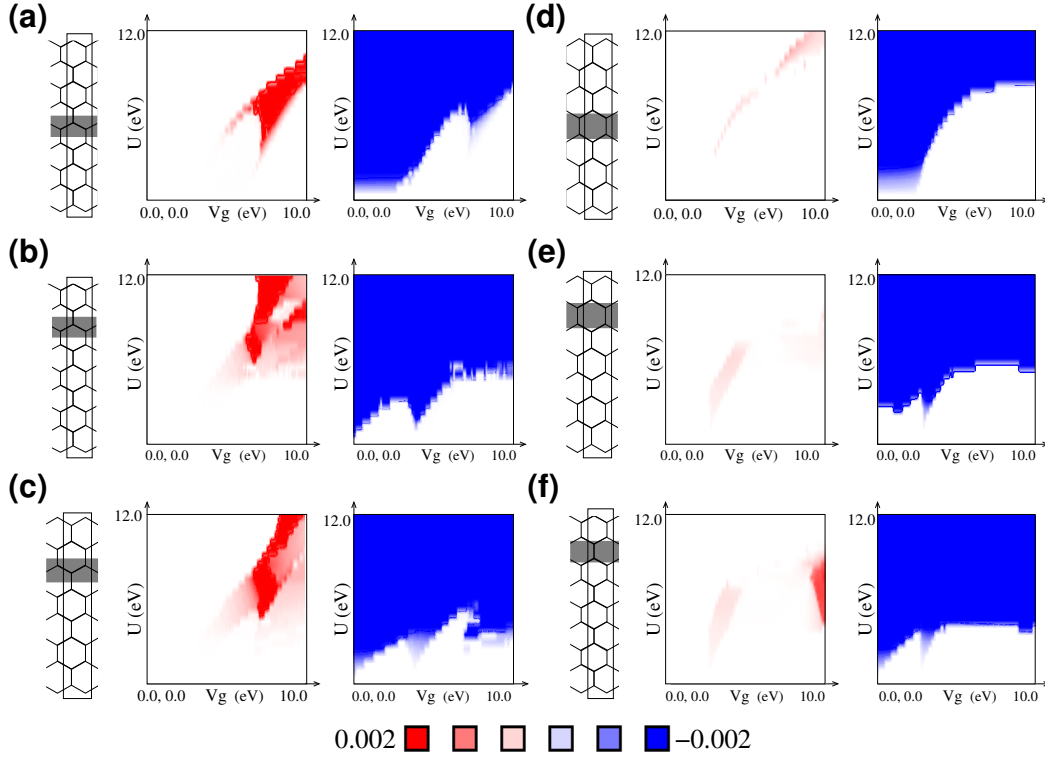


Figure 4.3: spin correlation(positive & negative) plot as a function of U and V_g with gate coverage of zigzag C-C bond for(a,b) $N_z = 9$, (c) $N_z = 8$. and with gate coverage of transverse C-C bond for(d,e) $N_z = 8$, (f) $N_z = 9$. unit-cell and bias coverage is shown here with solid line and gray shade respectively.

FM ordered states at those sites with that at the nearest localized edge states can mutually stabilize both of them and also induce FM ordering between the two edge states. The degree of stabilization would thus enhance due to proximity of the biased region to any of the edges. Whereas, if the biased sites covers the transverse C-C bonds the spin of FM ordered state at those sites would prefer an opposite spin at both the edges[Fig.4.4(a)]. However such a biasing results effectively into isolated biased dimers which would prefer a non magnetic ground state. As a result the appearance of n-n FM order is much suppressed in this case[Fig.4.3(d-f)]. Similar effective reduction of Coulomb correlation will happen for both the spins as the bias region shifts from the edge towards the bulk and it drives to a non-magnetic ground

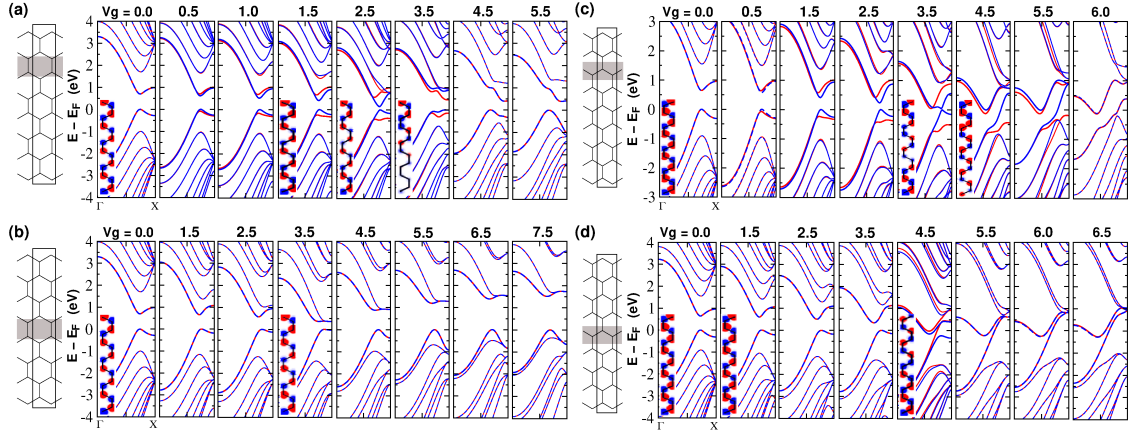


Figure 4.4: Band structure and spin density(inset) from mean-field Hubbard model for $U=4.0$ eV at different gate voltages V_g of ZGNR:(a,b) $N_z = 8$ with gate coverage of transverse C-C bond, and (c,d) $N_z = 9$ with gate coverage of zigzag C-C bond. unit-cell and bias coverage is shown here with a solid line and gray shade respectively.

state akin to AGNRs with a bias tunable spin-degenerate band structure[Fig.4.4(b)]. Therefore it is important that the biased sites should cover more zigzag chains than transverse dimers for onset of n-n FM order at moderate coupling. However, the systematic reduction of gap for one of the spins occurs for biased region near the edges irrespective of whether the biased region covers C-C transverse [Fig.4.4(a)] or zigzag[Fig.4.4(c)] bonds paving the way of bias controlled FM semiconducting and half-metallic window. For zigzag bias coverage the inter-edge AFM ordering clearly evolves into inter-edge FM ordering[Fig.4.4(c,d)] on the onset of n-n FM ordering as discussed above. To understand the evolution of the band edges we plot the bands projected on the edges[Fig.4.5]. Here, owing to inter-edge FM ordering after a certain threshold value of V_g the band edge corresponding to the minority spin (spin-2) for both the edges evolves and finally at the gate voltage at which the n-n FM emerges the valence band edge for spin-2 emerges into a partially occupied dispersive band[Fig.4.5], which offers a robust window of half-metallic transport. Therefore due to suppression and facilitation of edge states of a particular spin depending on the

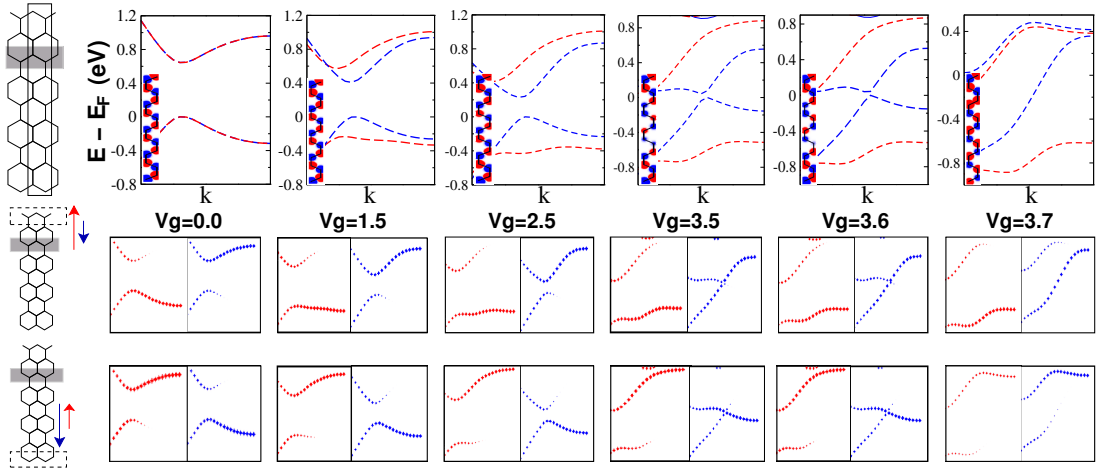


Figure 4.5: For gated configuration of Fig.4.4(c), projected band structure corresponding to the edge sites with majority and minority spin both. This shows a clear evolution of band edges with the emergence of n-n and inter-edge FM ordering (spin density :inset).

spin of the FM order, the evolution of band structure opens up a new mechanism to systematically open a window of half-metallic transport, compared to other previous known processes[9, 21, 22, 23].

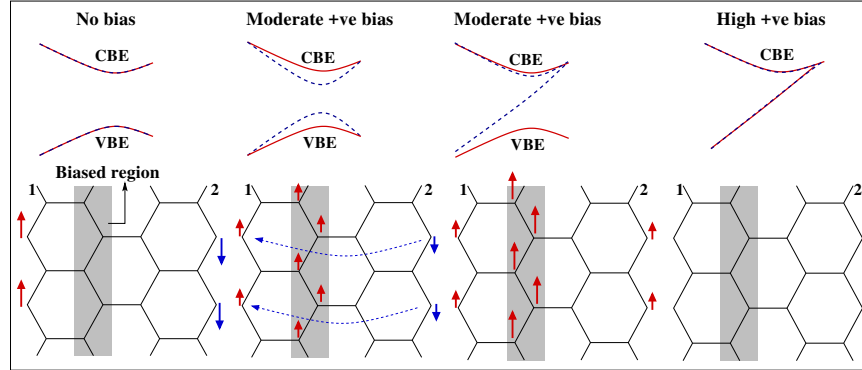


Figure 4.6: Schematic band diagram(above) and spin density(below). The migration of electrons with spin-2(\downarrow)from edge-2 towards edge-1, owing to n-n FM order with spin-1(\uparrow) at biased region, C(V)BE : conduction(valence)band edge.

This evolution of band structure can be understood from the schematic band diagram as shown in Fig.4.6. The competing interactions(n-n FM and inherent AFM)

leads to the stabilization of one of the edge states, say at edge-1 with spin-1 while suppression of the localized state at the other edge with spin-2. Therefore electrons with spin-2 would delocalize leading to reduction in band gap for the same spin. Eventually the spin at the edge-2 flips from spin-2 to spin-1 as favored by the n-n FM order leading to complete disappearance of the valence band edge of spin-2. This dispersive valence band of spin-2 offers a window for half-metallic transport. With further increase of V_g occupancy of biased sites with both the spins become favorable leading to delocalization of edge state at edge-1 which results into dispersive nature of the valence band with spin-1 as well. Therefore for both the spins the valence band becomes dispersive leading to a metallic phase.

4.2.3 First principles calculation for zigzag graphene nanoribbon

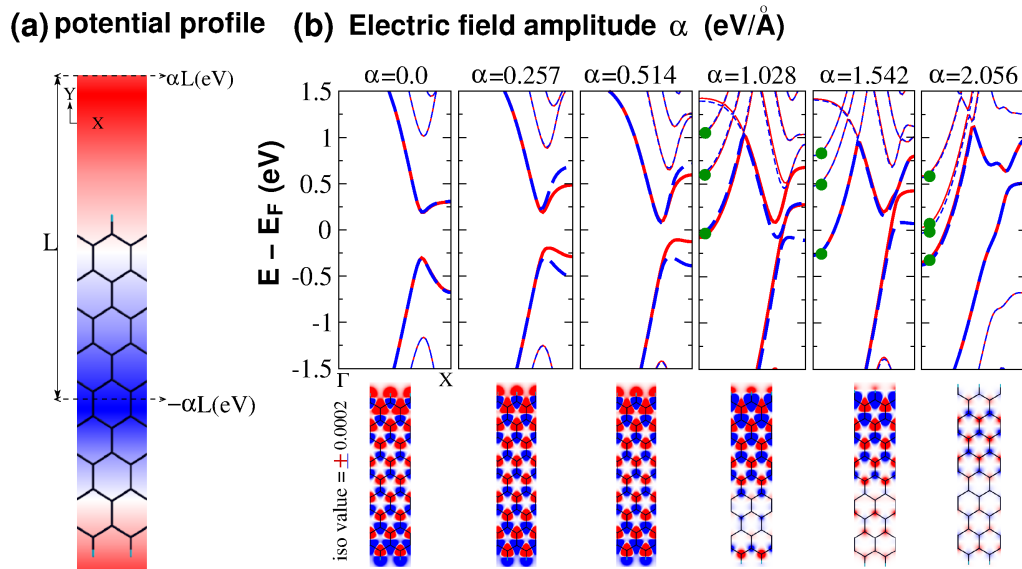


Figure 4.7: ZGNR in presence of sawtooth potential: (a) potential profile ; (b) band structure (above) & spin density(below). DFT results are qualitatively similar to their counterparts [Fig.4.4] based on mean-field Hubbard model.

To understand the impact of inhomogeneous biasing from first principles, we apply sawtooth potential along the transverse direction[Fig.4.7(a)] of ZGNR to resemble a bias coverage similar to Fig.4.3. We find a similar trend in terms of evolution of charge density as evident in Fig.4.4(c) which also shows the lifting of spin degeneracy and half-metallic window[Fig.4.7(b,c)] within a range of applied potential. This qualitative agreement between DFT and mean-field result is a verification of MFH results within the level of correlation considered in DFT. Furthermore, the reported agreement of DFT with more advanced methods like DMRG, QMC[24, 25] in rationalizing FM ground state for doped AGNRs at moderate coupling limit implies the likelihood of our mean-field results to be consistent with improved consideration of correlation. Structural relaxation from first principles indicates that the ribbons maintain their structure in that range of potential in which the n-n FM order exists.

However, in addition to the n-n FM ordering, DFT calculations of gated GNRs reveal an interesting new property. We find parabolic bands like those of free electrons[Fig.4.7(b)] about Fermi energy and above. Origin of these bands are traced to accumulation of space charge above and below the ribbon plane. Coinciding with emergence of n-n FM order space charge also acquires a spin polarization thus implying in effect a perfect one dimensional channel to transport electrons with a preferred spin. However, work in this direction is not expected to matured by the time of submission of this thesis. Further details about this has been presented in the section on future scope.

4.2.4 Mechanism & analysis with minimal model

The trend of emergence of n-n FM order in our results is present without doping and irrespective of existence of flat band at Fermi energy, which is indeed different from previous discussion[sec.3.2.1]. This n-n FM ordering is more prominent in presence

of narrow bias coverage near the edges of the ribbon. This clearly suggests that localization and the resultant enhancement of Coulomb correlation of the electrons are likely the responsible key factors for the emergence of the n-n FM order, which we will discuss in more detail in the following.

4.2.4.1 Nearest neighbor FM order in simple model

To further generalise our results we resort to a simple unit cell with four sites(4-site), of which two neighboring sites are biased[Fig.4.8(a)]. Remarkably, the spin-correlation between the two biased sites [Fig.4.8(b)] as a function of V_g and U has similar generic features as in case of AGNRs and ZGNRs, namely, existence of positive spin correlation implying n-n FM correlation among biased sites with similar variation of V_g and U , which thus establishes the generality of our results implying a general property of non-uniformly biased bipartite systems. This also allows us to focus on the 4-site model to probe the source of the n-n FM order in more detail. Notably, if we do not consider non-zero crystal momentum then the positive spin-correlation does not exist, implying the role of itinerant electrons in manifesting the n-n FM ordering. Nevertheless, in this case, the trend of spin-correlation as a function of V_g and U agrees qualitatively with that obtained using exact diagonalization(ED). So the itinerant electrons which are described by dispersive bands at Fermi energy, thus likely to play an important role in demonstration of n-n FM order, as suggested by Fig.4.2,4.4.

4.2.4.1.1 Phenomenological argument for n-n FM order : For 4-site system, the evolution of spin-polarized charge densities [Fig.4.9(a,c,e)] suggest a spin separation between biased and unbiased region similar to that observed in GNRs. The appearance of such spin separation can possibly be rationalized by regarding

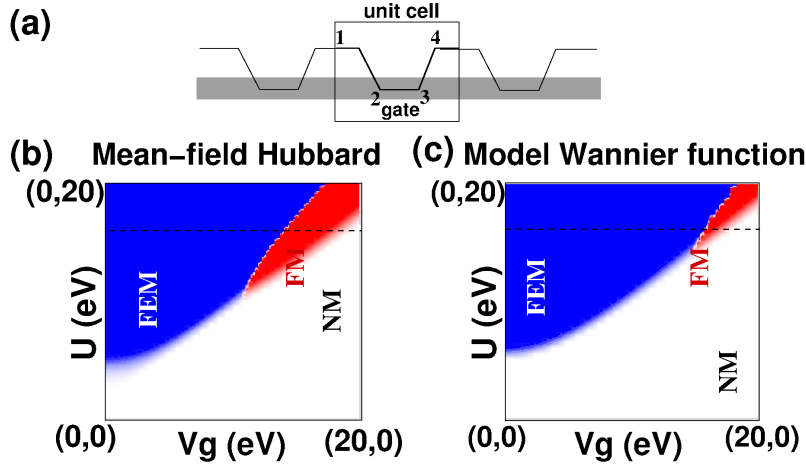


Figure 4.8: (a) 4-site model with n-n gate coverage. Bias site spin-correlation plot with (b) mean-field Hubbard model and (c) model Wannier function.

that the increased occupancy of the biased sites by electrons with both the spins, upon increase of V_g , would in turn increase potential energy due to on-site Coulomb repulsion. Thus to lower the potential energy at each of the biased sites they will prefer to be dominated by electrons with one of the spins. However, for such neighboring sites having opposite spins would correspond to the rapid oscillation of wave functions for both the spins between two neighboring sites, leading to enhance kinetic energy. Alternatively, if wave functions for one type of spin dominate both the biased sites over that of the other spin, as evident from the charge densities [Fig. 4.9(a,c,e)], the wave functions can be smoother, implying lesser kinetic energy while allowing lower on-site Coulomb repulsion as well. The evolution of charge densities [Fig. 4.9(a,c,e)] clearly implies electrons to be more itinerant for one spin than for the other upon emergence of n-n FM, leading to lifting of spin degeneracy [Fig. 4.9(c,d)] akin to that in Fig. 4.2(a,c). Upon further increase of V_g [Fig. 4.10(b,c,d)] the lowering of potential energy dominates over the increase of on-site Coulomb repulsion and it leads to an occupation of bias sites by both the spins. So, eventually it returns a non-magnetic ground state and spin degenerate band structure [Fig. 4.9(e,f)]. Thus for a higher U a

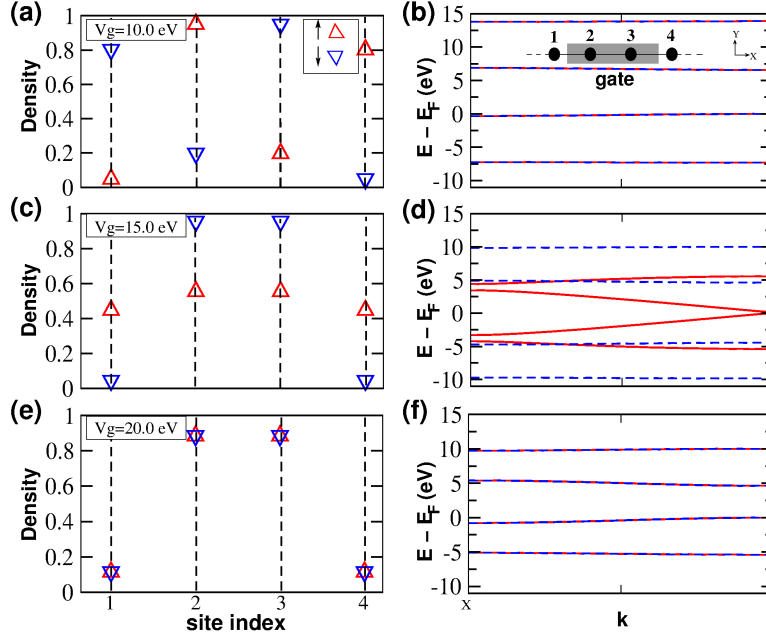


Figure 4.9: Density(up,down) and band structure of 4-site system[Fig.4.8(a)] from mean-field Hubbard model for $U=15.0$ eV with: (a,b) $V_g=10.0$ eV; (c,d) $V_g=15.0$ eV and (e,f) $V_g=20.0$ eV.

higher V_g is required for the n-n FM order to quench, which is also consistent with the trend observed in Fig.4.1,4.3. Notably, the band structure[Fig.4.9(d)] also shows closing of gap for the minority spin upon emergence of n-n FM order, as observed for zigzag ribbons.

4.2.4.1.2 Quantitative analysis of mechanism : For a quantitative confirmation of the above mechanism, we partition the total energy[Fig.4.10(a,b)] of the ground state into kinetic energy and potential energies contributed by on-site Coulomb repulsion and applied bias. The energetics of unconstrained(UC) ground state is then compared with their counterparts obtained by considering non-magnetic(NM) and FEM constraints on the ground states. NM condition is imposed by assigning the same charge density for both the spins during self-consistent calculation whereas, for FEM the charge density for one of the spins is specified to be the mirror image of that

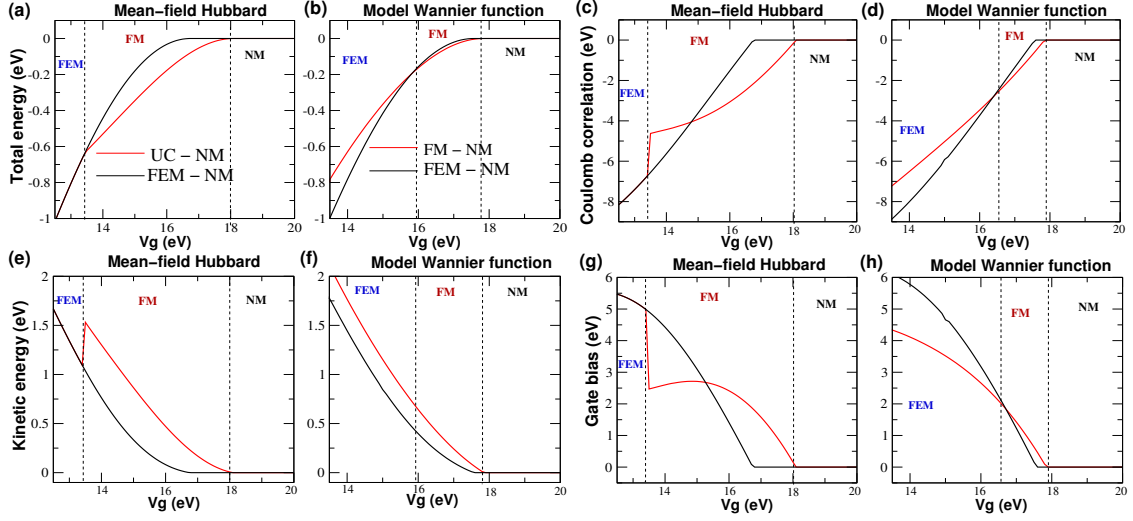


Figure 4.10: Different energy contributions for $U=15.0$ eV from : mean-field Hubbard model(a,c,e,g) & model WFs calculation(b,d,f,h). for a range of applied bias V_g to focus at three different regime : FEM, FM and NM along the dotted line of Fig.4.8(b,c).

for the other spin about the center of the unit cell. Then considering NM ground state as the reference the energetics are plotted in Fig.4.10(a-h). From Fig.4.10(e,g) it is evident that the UC ground state with n-n FM order has lower energy in comparison to NM and FEM ground states. This lowering is initially facilitated by lowering of potential energy due to gate bias, but subsequently due to lowering of onsite Coulomb repulsion aided by spin separation of between biased and unbiased sites. Notably, although in comparison to UC ground state the FEM ground state has a lower kinetic energy, the degree of localization at the positively biased region offered by the latter appears to be much lower. Thus for a FEM ordered state having the same degree of localization like the UC ground state it must have higher kinetic energy as anticipated in the phenomenological argument. Therefore, minimization of on-site Coulomb repulsion with the least increase in kinetic energy thus indicating maximal retention of the itinerant nature of electrons, is the essential factor of having n-n FM order in the ground state.

4.2.4.1.3 Beyond mean field approximation : For further illustration of this observed n-n FM order beyond the mean-field approximation, we resort to a simple analytical model of Wannier functions(WFs) to express the ground state of the 4-site unit cell at half-filling. The model WFs are based on WFs computed from the Bloch functions obtained within mean field approximation and it can be chosen to be real and highly localized within a unit cell in one dimension. Thus in place of $2N_k$, wave functions for each spin, where N_k is the number of allowed wave vectors in the first BZ, two WFs for each spin is adequate to represent four electrons. Here we approximate the WFs to be non-zero only within a unit cell. Such approximate WFs for the NM ground state can be written in the general form as:

$$\begin{aligned}\phi_{1,\uparrow/\downarrow}^{NM} &= (a, b, c, d), \\ \phi_{2,\uparrow/\downarrow}^{NM} &= \left(e + \frac{c.f}{a}, g + \frac{d.f}{b}, -f - \frac{a.e}{c}, -f - \frac{g.b}{d} \right),\end{aligned}$$

which are orthogonal to each other by construction. Similarly, two orthogonal WFs for the FEM ground state can be approximated as:

$$\begin{aligned}\phi_{1,\uparrow}^{FeM} &= (a, b, c, d), \\ \phi_{2,\uparrow}^{FeM} &= \left(e + \frac{c.f}{a}, g + \frac{d.f}{b}, -f - \frac{a.e}{c}, -f - \frac{g.b}{d} \right), \\ \phi_{1,\downarrow}^{FeM} &= (d, c, b, a), \\ \phi_{2,\downarrow}^{FeM} &= \left(f + \frac{g.b}{d}, f + \frac{a.e}{c}, -g - \frac{d.f}{b}, -e - \frac{c.f}{a} \right),\end{aligned}$$

where the $|\phi_{i,\uparrow}|^2$ is mirror image of $|\phi_{i,\downarrow}|^2$ with respect to the middle of the unit cell. Finally, orthogonal WFs with nn FM can be approximated as:

$$\begin{aligned}\phi_{1,\uparrow}^{FM} &= (a, b, b, a), \\ \phi_{2,\uparrow}^{FM} &= (c, d, -d, -c), \\ \phi_{1,\downarrow}^{FM} &= (e, f, f, e), \\ \phi_{2,\downarrow}^{FM} &= (g, h, -h, -g).\end{aligned}$$

To represents the WFs the number of independent variables are determined from the symmetry of the spin densities[Fig.4.9(a,c,e)] and orthogonality of the states. The total energies of the ground states are calculated on the basis of this WFs within the Hubbard model without mean-field approximation. For all sets of WFs the ground state is obtained by minimizing the total energy in terms of a, b, c, d, e, f, g, h variables and t, U, V_g as parameters using the cylindrical algebraic decomposition scheme as implemented in Mathematica[26]. From this model calculation the spin-correlation function of the biased sites shows a similar type of n-n FM ordering[Fig.4.8(c)] as obtained using MFH calculation. Using this model WFs of ground states the kinetic energy and the potential energies due to on-site Coulomb repulsion and external bias are estimated from the expectation value. Notably, Fig.4.10(b,d,f,h) implies exactly the same trend of emergence of n-n FM order as suggested within the mean-field Hubbard model[Fig.4.10(a,c,e,g)]. These agreements along with agreements with DFT results, are the basis of our claim of generality of n-n FM order beyond mean-field approximation, as a property of inhomogeneously biased bipartite system.

4.3 Possible experimental realization

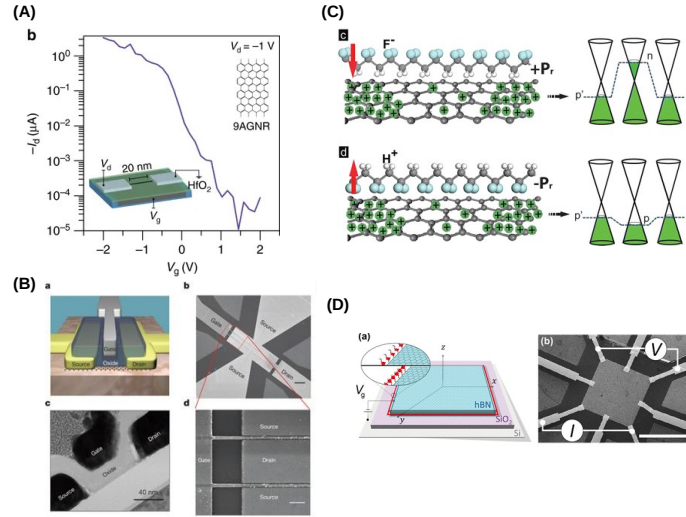


Figure 4.11: (A) 6.5 nm HfO_2 local back gate [Ref. [31]], (B) a, Schematic view of a top-gated graphene r.f. transistor on DLC substrate. b, SEM image of a typical top-gated dual-channel r.f. device. Scale bar, 3 μm . c, Cross-section TEM image of a graphene transistor with a gate length of 40 nm. Scale bar, 40 nm. d, SEM image of the 40-nm device. Scale bar, 400 nm. [Ref. [30]], (C) c. Electrostatic doping in graphene with P(VDF-TrFE) at the +Pr state. The green particles in graphene represent the initial p-type charged impurities doping, d. (c) Electrostatic doping in graphene with P(VDF-TrFE) at the -Pr state. The green particles in graphene represent the initial p-type charged impurities doping [Ref. [32]], (D) a. Polar molecules at graphene edges in micrometer-scaled gated devices, Inset shows the two collectively aligned molecular configurations existing at graphene edges: above and below the graphene plane, b. SEM of one of our devices. Scale bar is 5 μm . [Ref. [33]]

In view of recent experimental advancement [Fig. 4.11(A-D)], implementation of gate in nanoelectronic devices has been reached upto sub-micron length or even less than that [27, 28, 29, 30, 31]. Beyond these there is another functionalization as well, which would lead to similar properties, such as deposition of ferroelectric polymer gate [32] or via adsorption at precise sites [33]. Therefore our results might encourage the implementation of this direction in the future.

Bibliography

- [1] A. H. Castro Neto, F. Guinea, N. M. R. Peres, K. S. Novoselov, and A. K. Geim, *Reviews of Modern Physics*, (81)109, **(2009)**.
- [2] D. Soriano & J. Fernández-Rossier, *Phys. Rev. B*, (85)195433, **(2012)**.
- [3] N. F. Mott, *Proc. Phys. Soc. London, Ser. A*, (62)416, **(1949)**.
- [4] L. M. Martelo, M. Dzierzawa, L. Siffert, D. Baeriswy, *Z. Phys. B*, (103), 335-338, **(1997)**.
- [5] Patrick Fazekas, Series in Modern Condensed Matter Physics - Vol.5 {5 Toh Tuck Link, Singapore 596224, World Scientific Publishing Co. Pte. Ltd.**(1999)**.
- [6] Young-Woo Son, Marvin L. Cohen, and Steven G. Louie, *Phys. Rev. Lett.*, (97)216803, **(2006)**.
- [7] Kyle A. Ritter & Joseph W. Lyding, *Nature Materials*, 8, **(2009)**.
- [8] Gábor Zsolt Magda *et al.* *Nature*, 514, **(2014)**.
- [9] Young-Woo Son, Marvin L. Cohen & Steven G. Louie, *Nature*, 444, 347-349, **(2006)**.
- [10] H. Raza, E. Kan, *Phys. Rev. B*, (77)245434, **(2008)**.

- [11] Lian Sun, Qunxiang Li, Hao Ren, Haibin Su, Q. W. Shi, and Jinlong Yang *The Journal of Chemical Physics*, (129)074704, **(2008)**.
- [12] F. Cervantes-Sodi, G. Csányi, S. Piscanec, A. C. Ferrari, *Phys. Rev. B* 77, 165427, **(2008)**.
- [13] X. Deng, Y. Wu, J. Dai *et al.*, *Physics Letters A*, (375)3890, **(2011)**.
- [14] Oleg V. Yazyev, Lothar Helm, *Phys. Rev. B*, (75)125408, **(2007)**.
- [15] Yan, L., Zheng, Y. B., Zhao, F. *et al.* , *Chem. Soc. Rev.*, 41(1), **(2012)**.
- [16] Yea-Lee Lee, Seungchul Kim, Changwon Park, Jisoon Ihm, Young-Woo Son, *ACS Nano*, 4, 3, **(2010)**.
- [17] J. W. Mintmire, B. I. Dunlap, and C. T. White, *Phys. Rev. Lett.* 68, 631**(1992)**;
J. W. G. Wilder, L. C. Venema, A. G. Rinzler, R. E. Smalley, and C. Dekker, *Nature* (London) 391, 59 **(1998)**; T. W. Odom, J. L. Huang, P. Kim, and C. M. Lieber, *Nature* (London) 391, 62 **(1998)**.
- [18] P. Ewald, *Ann. Phys.*, 369(3), **(1921)**.
- [19] A. Bródka, *Chemical Physics Letters*, 363, 604, **(2002)**.
- [20] S. Sorella and E. Tosatti, *Europhys. Lett.*, (19)699, **(1992)**.
- [21] S. Dutta, & S. K. Pati, *J. Phys. Chem. B*, 112(5), 1333 **(2008)**.
- [22] Er-jun Kan, Z. Li, J. Yang, & J. G. Hou, *J. Am. Chem. Soc.* 130(13)4224, **(2008)**.
- [23] J. Bhattacharjee, *J. Chem. Phys.* 137, 094705 **(2012)**.

- [24] H.-H. Lin, T. Hikihara, H.-T. Jeng, B.-L. Huang, C.-Y. Mou, and X. Hu, *Phys. Rev. B*, (79)035405, **(2009)**.
- [25] H. Feldner, Zi Y. Meng, A. Honecker, D. Cabra, S. Wessel & F. F. Assaad, *Phys. Rev. B*, (81)115416, **(2010)**.
- [26] Wolfram Research, Inc., Mathematica, Version 10.0, Champaign, IL **(2014)**.
- [27] Xinran Wang *et al.*, *Phys. Rev. Lett.*, 100,206803, **(2008)**
- [28] L. Liao *et al.*, *Nature*, 467, **(2010)**.
- [29] Frank Schwierz, *Nature Nanotechnology*, 5, **(2010)**.
- [30] Yanqing Wu *et al.*, *Nature*, 472, **(2011)**.
- [31] Juan Pablo Llinas *et al.*, *Nature Communications*, 8, 633, **(2017)**.
- [32] Guang-Xin Ni *et al.*, *ACS Nano*, 6, 5, **(2012)**.
- [33] José M. Caridad *et al.*, *Nano Lett.*, 18, **(2018)**.

Chapter 5

Magnetism in graphene-hexagonal boron nitride hybrids

5.1 Introduction

Atomically thin layered magnetic materials with sustain magnetism are desirable for miniaturization of data storage and processing devices. Layered magnetic materials with lighter elements will thus be ideal since lighter elements have weak spin-orbit coupling and therefore large spin relaxation time. Low dimensional materials made of 2p block elements, namely, carbon(C), boron(B), nitrogen(N) with p electron based magnetism has thus opened up a new vista owing not only due to their sustain magnetism but also due to their structural stability and resilience.

Pristine graphene and hBN both are non-magnetic, nevertheless, in graphene-hBN hybrid systems, the possibility of manipulating local magnetic moments, which naturally arises at the interface, boundaries [1, 2, 3] and defects [4] is promising. In these hybrid systems, local moments corresponds to non-degenerate density of states at Fermi energy, which can lead to a ferromagnetic semiconductor, metal or a half-

metal[5, 6, 7]. Substitution by C in hBN is known to form patches of graphene. As per Lieb's theorem[8] graphene islands(Gr-island), covering dissimilar number of sites from the two sub-lattices will have nonzero magnetic moment. Triangular Gr-islands with zigzag edges are known to have largest sub-lattice asymmetry and therefore the largest magnetic moment which is evident from the fact that all its zigzag edges belong to the same sub-lattice[9]. Such Gr-islands have been observed to distribute themselves in arrays in hBN matrix[10, 11, 12, 13], which motivates exploration of scopes for new kind of magnetic materials made of non-metals. In case of free standing networks of triangular Gr-islands, FM ordering has been proposed[14, 15, 16] through magnetic ordering propagated by interlinking C chains. Magnetic ordering for such neighboring magnetic Gr-islands embedded in hBN has come under [17, 18] focus in recent years, although a detailed understanding of mediation of magnetic order by hBN is yet to be established, which motivates the work presented in this chapter.

Here we first focus on interaction between magnetic Gr-islands starting with two of them and then further extending to larger hybrid structures. Specifically, we focus on deriving the microscopic mechanism of propagation of magnetic order through hBN and learn how to establish FM ordering between two magnetic Gr-islands embedded in hBN. We then apply our understanding to propose graphene-hBN hybrid systems which may be half-metal or FM semiconductor possibly at room temperature. All the analysis presented here are based on spin-polarized electronic structure and spatially localized Wannier function computed from first principles. Proposed mechanism has been described within mean-field model through spin dependent hopping.

5.2 Calculation details

All the equilibrium configurations and their energetics are calculated within LSDA using ultrasoft pseudopotential and gradient corrected PBE functional as implemented in Quantum espresso[sec.2.2.3]. All the configurations through total energy minimization using BFGS are converged with plane wave cut-off over 800 eV considering a k-mesh which is equivalent to 30×30 for a hBN primitive cell and forces per atom less than 10^{-4} Rydberg/Bohr. For atomically resolved analysis of electronic structure, WFs are constructed as described in sec.2.4.1.2. The microscopic mechanism implied by results from first principles, is verified with the TB framework using the mean-field approximation of Hubbard model. Phase diagrams have been calculated using mean-field Hubbard model described in sec.5.2.1.

5.2.1 Estimation of mean-field parameters

Within model Hamiltonian approach, for heteroatomic(graphene-hBN hybrid) system using Eq.2.48 mean-field Hubbard[sec.2.3.4.1](MFH) Hamiltonian can be written as,

$$H_{MF} = \sum_{i,\sigma} \varepsilon_i c_{i\sigma}^\dagger c_{i\sigma} + \sum_{\langle i,j \rangle, \sigma} t_{ij} c_{i\sigma}^\dagger c_{j\sigma} + \sum_{i,\sigma} U_i n_{i\sigma} \langle n_{i\sigma'} \rangle \quad (5.1)$$

where $\varepsilon_i : \varepsilon_B, \varepsilon_N, \varepsilon_C$ being the on-site energy at B, N and C-site respectively. $t_{ij} : t_{CC}, t_{BN}, t_{CN}, t_{CB}$ are nearest neighbor hopping parameters and $U_i : U_B, U_N, U_C$ are the strength of onsite Coulomb repulsion.

Since the valence shell of B, C, and N are of same principal quantum number($n=2$), we have considered same $\{U\}$ and hopping parameters($\{t\}$) for all sites. We have fitted the bulk boron nitride DFT band gap to MFH gap to tune the onsite parameters of B and N. We set the onsite term of C to zero. The comparison of projected density of

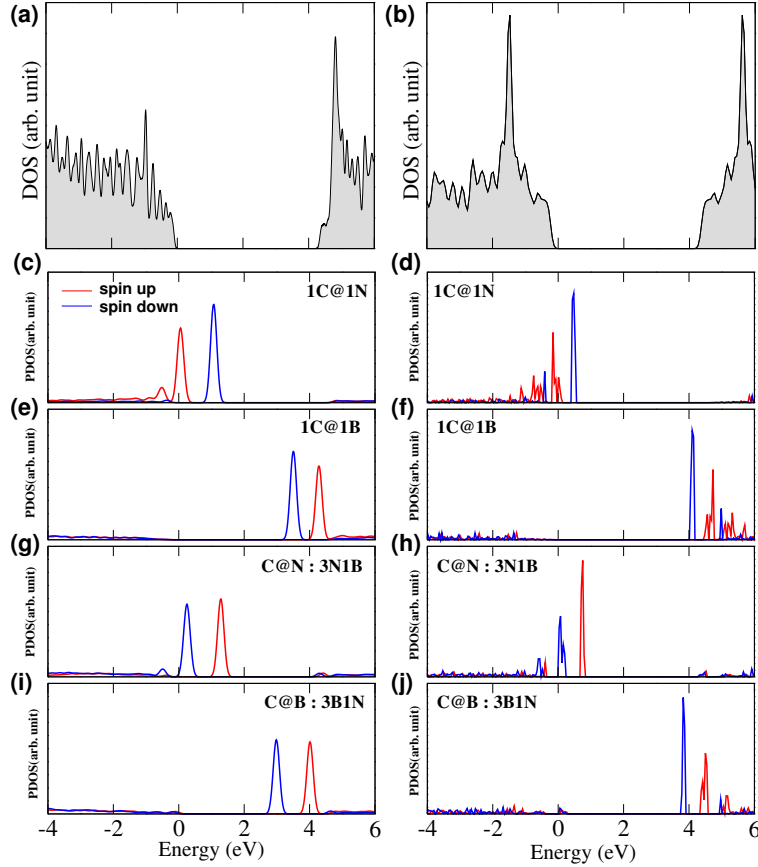


Figure 5.1: Density of states for pristine hexagonal boron nitride from (a) DFT and (b) MFH model. Projected density of states of the C-site for different C-substituted hBN from DFT and MFH calculation (c,d) 1C@1N, (e,f) 1B@1C, (g,h) C@N site for 3N1B island and (i,j) C@B site for 3B1N island respectively. Valence band edge has been adjusted to $E=0$ for better comparison in both cases.

states (PDOS) in Fig. 5.1 imply that with further marginal variation of the onsite term of C and CB or CN hopping parameters (t_{CB}, t_{CN}) the fit of PDOS can be improved, although not exhaustively. Incremental improvements of fitting can be further envisaged by tuning the Hubbard U for B and N and t_{CB}, t_{CN} . Partitioning of sites as per their proximity to the interfaces can bring in additional scopes of variation in fitting parameters. However, our goal here is to demonstrate the validity of the mechanism suggested by DFT results, within the framework of Hubbard model, and to that end, an exact evaluation of parameters is not an essential requirement. We thus only vary

the onsite terms of B and N and keep all the other parameters same as graphene[19]. Various literature[20, 21, 22] indeed suggests variations of those parameters within 20% on average.

Using first principles data we estimate the exchange coupling parameter J and the corresponding transition temperature(T_C) by using the Ising model of honeycomb lattice considering nearest neighbor coupling only[23] as,

$$T_C = \frac{2J}{\ln(2 + \sqrt{3})}, \quad (5.2)$$

where $-6J = (E_{FM} - E_{AFM})$, and E_{FM}, E_{AFM} are the energies corresponding to FM and AFM configurations obtained from DFT.

5.3 Interaction between magnetic graphene islands in hBN

First, we have considered interaction between an isolated pair of magnetic Gr-islands embedded in a large segment of hBN, followed by honeycomb lattice made by the same Gr-islands implying a graphene-hBN hybrid super-lattice.

We have considered two configurations of C4 islands: 3B1N(C4a) and 3N1B(C4b). At their closest approach C4a(C4b) islands are separated by single N(B)[Fig 5.2(a:inset)] site denoted as $d=0$, where d denotes an intermediate B-N pathway made of $2d+1$ sites connecting two nearest graphene islands. Due to asymmetric sub-lattice coverage, both the islands host a magnetic moment of $(3-1)=2 \mu_B$ according to Lieb's theorem for bipartite system.

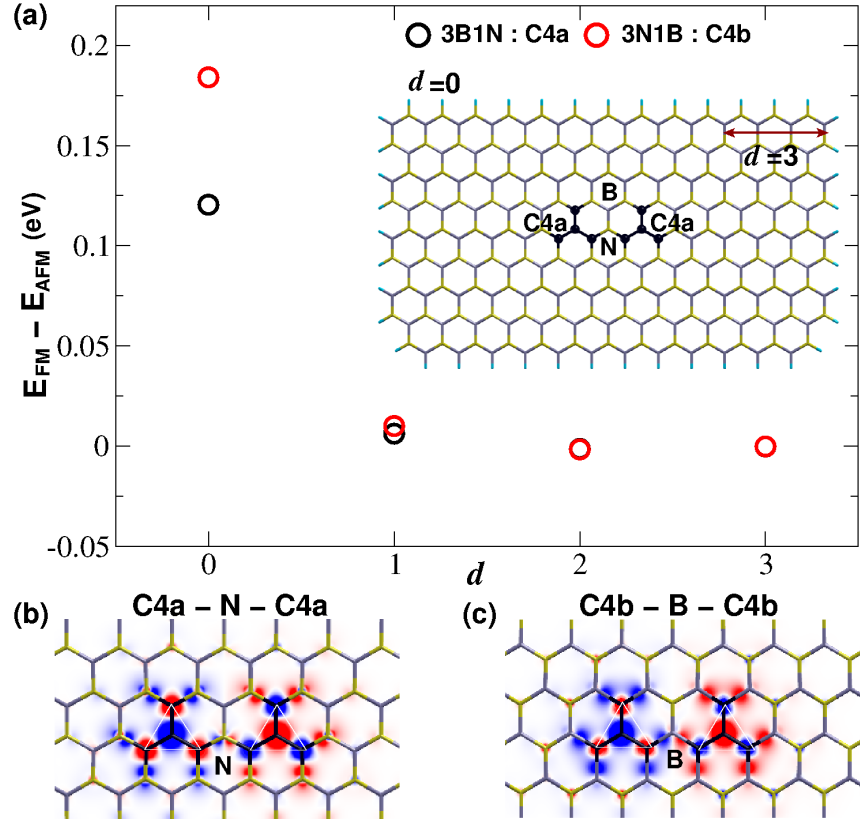


Figure 5.2: For C4 island within a hydrogen passivated hBN chunk: (a)energy difference($E_{FM} - E_{AFM}$) for different island separation d (Inset: C4a island in hBN chunk for $d=0$ and the separation d) and spin density with single site separation($d=0$) for (b)C4a-N-C4a, (c)C4b-B-C4b. $E_{FM} - E_{AFM} > (<) 0$ favors AFM(FM) ordering.

5.3.1 Isolated pair of graphene islands

Magnetic islands in proximity in hBN have been argued from first principles calculation to favor AFM ordering as a means to allow delocalization of spin densities[17, 18], although the exact mechanism is yet to be derived. Similar AFM ordering also exists for our systems irrespective of C4a or C4b islands[Fig. 5.2(b,c)] within a isolated hBN patch of increasing size. The strength of AFM ordering reduces with increase of island separation d . With $d > 4$ the islands in effect become isolated[Fig. 5.2(a)]. The strength of AFM coupling is more if it mediates through N (C4a-island) than

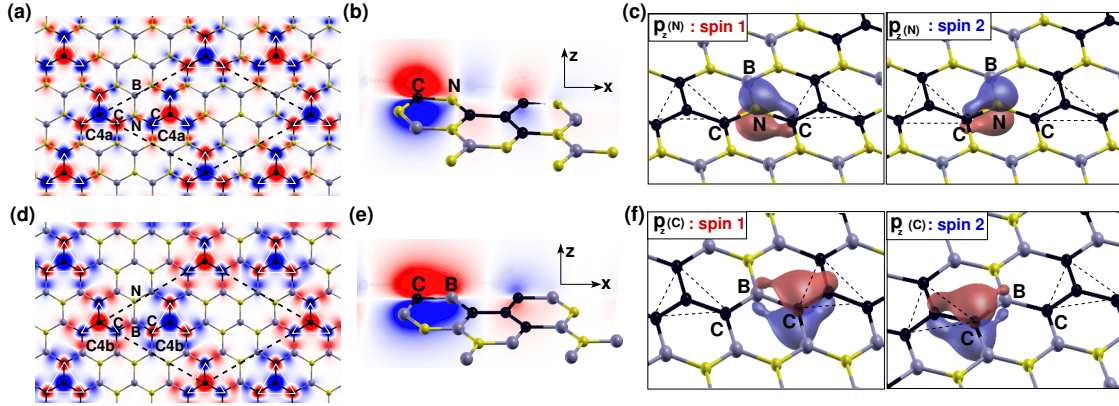


Figure 5.3: LSDA Spin density of a pair of (a)C4a(3B1N) and (d) C4b(3N1B) as a part of a honeycomb super-lattices in hBN sheet are shown Planar projection of Wannier functions representing $2p_z$ orbital of C along (b) C-N and (e) C-B bonds for honeycomb super-lattices made of C4a and C4b islands respectively. Spin-resolved Wannier function of $2p_z$ orbital of (c)the bridging N atoms between C4b islands and (f) of the outer C atoms of the C4a islands connected through a B atom.

B(C4b-island) as shown by energy difference plot in Fig. 5.2(a). Careful observation of spin density at intermediate N and B atom shows a spatial separation for electrons with opposite spins towards the two AFM ordered islands on two sides hinting at a microscopic mechanism akin to super-exchange to be responsible for mediation of magnetic order.

5.3.2 Honeycomb super-lattice of C4 islands

The smallest honeycomb super-lattice consisting of two C4a or C4b islands with separation of a single site(N or B) also shows AFM ordering between the Gr-island like in pair of Gr-islands in hBN[Fig. 5.2(a)]. Also like the latter, spatial separation of opposite spins occur at N or B -site[Fig. 5.3(a,d)]. To trace the origin of such spin separation we looked at orbital resolved Wannier functions, which represents the extent of spatial localization of the $2p_z$ orbitals of C and N. As evident from Fig. 5.3(c), at N-site, two unpaired $2p_z$ orbitals with opposite spins(spin1 and spin2) extend spa-

tially in opposite directions resulting in back transfers of electrons with opposite spins from N to the two C atoms on its two sides. Similar back transfer of opposite spins also happens from $2p_z$ orbitals of the two C atoms to the N atom. Similarly for intermediate B atom between the C4b islands[Fig. 5.3(f)], the back transferred electrons due to the $2p_z$ orbitals of C atoms from nearest neighbor sites are of opposite spins implying a spin separation about B as observed in the spin densities[Fig. 5.3(d,e)]. Furthermore, the planar projection of the orbitals in Fig. 5.3(b,e) implies that the amount of back transfer electrons from C to B atom is relatively more than that from C to N, which is consistent with the result that B mediated AFM ordering is stronger than that mediated by N, implying a possible connectivity between spin separation of lone pairs and back transferred electrons on sites along the -B-N- pathway, to the observed AFM order of the Gr-islands it connects. In addition, the estimation of effective J using hybrid functional(HSE) for exchange-correlation confirms that -B-N-zigzag connectivity between nearby Gr-islands favors AFM ordering more than -B-N-armchair connectivity[17].

5.3.3 Mechanism of mediation of magnetic ordering

The spatial separation of orbitals of opposite spins implies a super-exchange like mechanism for propagation of magnetic order through -B-N- pathway. We consider spin dependent hopping parameter within the TB model and test its relevance in determining the magnetic ordering of the ground state. Spatial separation of WFs representing the N lone pair suggests a symmetric displacement for the orbitals with opposite spin from the atomic site as considered schematically in Fig. 5.4(a), which naturally implies spin asymmetry of hopping. This also implies an equal enhancement of orbital energy i.e. the onsite energy value for both the spins since they move away from the local minima of the potential. We consider a pair of C4(C4a

& C4b) islands in close proximity ($d=0$) within a large hBN segment so that the edges are sufficiently away from the islands to mutually impact magnetism of each other. Imposing the appropriate constraints we then calculate AFM, FM and non-magnetic(NM) ground states as a function of spin-asymmetric hopping defined as, $\Delta t = t - t'$ applied to all the B-C and N-C bonds around the islands, and increase in onsite term of the associated B and N sites denoted by $E_{on-site}$. The true magnetic ordering of the ground state is obtained by comparing total energies calculated from AFM, FM and NM conditions. We chose Gr-islands within an isolated hBN segment in order to avoid the dependence of the magnetic ordering on the periodicity of unit cell. From MFH based phase diagram[Fig.5.4(b,c)] it is evident that without spin dependent hopping($\Delta t = 0$) the ground state is FM ordered with total magnetization $4\mu_B$ obtained from two FM ordered C4 island, which is in disagreement with DFT result. Within MFH model the emergence of AFM ordered ground state is only possible beyond a threshold value of Δt . As evident from Fig.5.4(b,c) the threshold value of Δt decreases with decreasing U and with increasing onsite term. Therefore, with all the standard onsite energy values and U for B, C and N site, spin dependent hopping parameter is indispensable in order to have the AFM ordered ground state for Gr-islands, as observed with DFT. These results thus point out the role of onsite Coulomb correlation at the intermediate B and N sites in mediating the AFM ordering between Gr-islands. Also, the result that the onset of AFM ordered ground state occurs at a lesser threshold value of Δt [Fig.5.4(c)] in case of B mediated C4b islands agrees with the DFT result that B mediated AFM order is stronger than N mediated AFM order. We recall here that in sec.5.3.2 this trend was rationalized based on higher rate of back transfer of electrons from C to B than that to N. This analysis thus establishes onsite Coulomb repulsion driven spin dependent hopping as a generic refinement of TB model for bipartite lattices with different onsite energies at

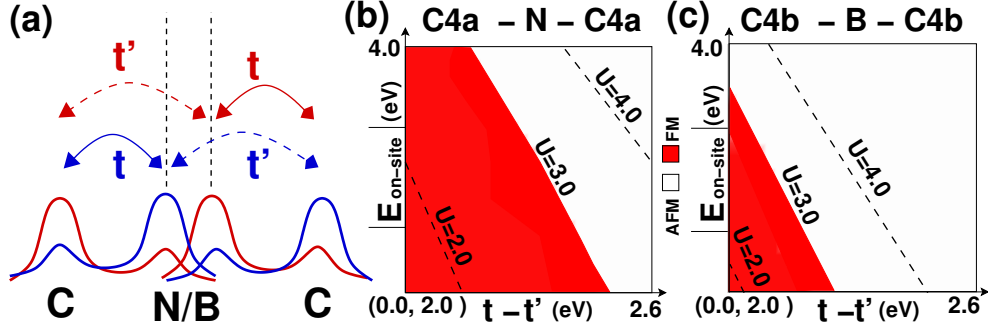


Figure 5.4: (a) Schematic representation of spin dependent hopping mechanism. Contour plot of total magnetization of the ground state calculated as a function of $(t-t')$ and onsite energy $E_{on-site}$ for a pair of (b) C4a(3B1N) and (c) C4b(3N1B) islands with $d = 0$ in a finite hBN segment at three different U values (2.0, 3.0 and 4.0) eV. For $U=4.0$ eV and $U=2.0$ eV the FM-AFM boundary is shown by black dotted line.

two sub-lattices, where the sites in rich sub-lattice offer super-exchange like pathway for magnetic ordering.

5.3.3.1 Microscopic model

Schematic diagram of Fig. 5.5(a) summarizes the mechanism of propagation of AFM order through -B-N- zigzag pathway between Gr-islands. In fact, this mechanism points out a general property of magnetic ordering mediated via zigzag bipartite lattices between two local magnetic moments [Fig. 5.5(b)] and inherently it would be AFM irrespective of whether the local moments belong to the same or opposite sub-lattices as represented in Fig. 5.5(b). Notably, this is different from graphene because there the nature of magnetic interaction depends on whether the moments are on same or different sub-lattices. The interaction between local moments in hBN becomes weak if the intermediate -B-N- pathway consists of an equal number of B and N sites, as this implies an integer number of B-N bonds and the back transfer of electrons along the bonds can occur on equal footing for both the spins in order to reduce the kinetic energy. This is also the possible reason why -B-N- armchair connectivity

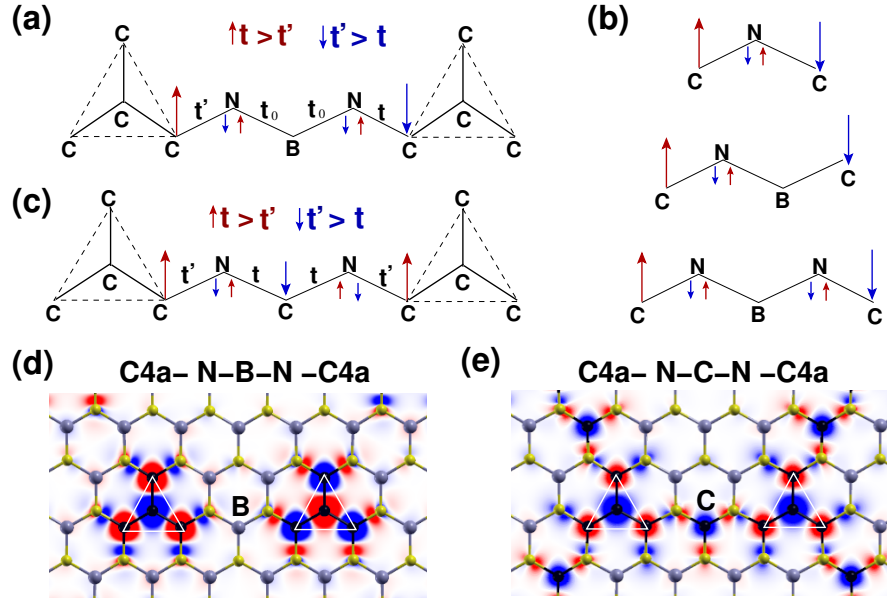


Figure 5.5: Schematic model of (a) AFM ordered C4a(3B1N) islands with spin dependent hopping. (b) Inherent AFM order between two local moment shown by C. (c) FM ordered C4a(3B1N) islands due to the extra local moment(C) at B site between the C4a islands. LSDA spin density plot of honeycomb super-lattice of C4a islands with $d = 1$ in (c) absence and (d) presence of C in the intermediate B sites. Wannier function representing the $2p_z$ orbitals of (e) the two N atoms back transferring to the C in the middle.

is less effective in the propagation of AFM order.

5.3.3.2 Switching of anti-ferromagnetic to ferromagnetic order

This mechanism[Fig.5.5(a)] also suggests that the AFM order can be switched to FM order if in the connecting pathway another unpaired electron is added as shown schematically in Fig.5.5(c). An unpaired electron can be due to a single substitution of C at B or N site or more generally due to formation of another magnetic Gr-island within the -B-N- pathway between the two Gr-islands of the honeycomb lattice. Spin densities in Fig.5.5(d) and Fig.5.5(e) without and with the intermediate C between the C4 islands respectively, indeed confirms the anticipated switching of magnetic order from AFM to FM between Gr-islands(C4a) connected through -N-C-N- zigzag

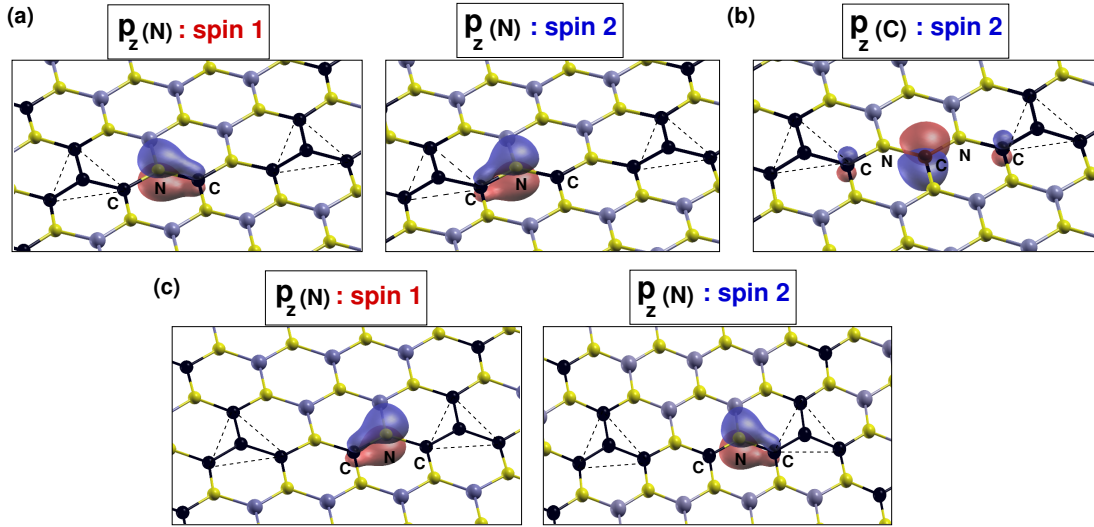


Figure 5.6: Wannier function representing the $2p_z$ orbitals of (e)the two N atoms back transferring to the C in the middle, and (f)of the C atom itself, in the -N-C-N-zigzag pathway between C4a islands.

pathway. The role of the unpaired electron in emergence of FM order of the magnetic Gr-islands is evident from spin density [Fig. 5.5(e)] and Wannier function plot [Fig. 5.6(a,c)]. The two neighboring N atoms on two sides of isolated C is seen to back transfer electrons to that C atom of similar spin (spin1) [Fig. 5.6(a,c)] due to the presence of an electron with opposite spin (spin2) at C [Fig. 5.6(b)], hence it appears to open up a half-metallic bridge along the connecting pathway of the two Gr-islands.

5.4 Ferromagnetic ordering in honeycomb-Kagome double-lattice

Incorporation of additional local moments between the two nearest moments, which constituted the honeycomb(H) lattice, essentially implies an interpenetrating honeycomb(H)-Kagome(K) double-lattice of local moments, wherein, different choices of location of the additional moment would lead to different twisted Kagome lattices. Here on-

wards we will focus on electronic structure and magnetism of a systematic variety of H-K double-lattices of Gr-islands in hBN, which we will refer as the Gr-hBN hybrid super-lattice.

We now describe a systematic understanding of variation of strength of FM ordering in the honeycomb lattice as a function of variation of the Kagome lattice as apparent in Fig. 5.7(a). We consider C4 islands to constitute the honeycomb lattice and isolated substitution by C(X) to constitute the Kagome lattice. Note that different locations of X lead to a variety of twisted Kagome lattices. The energy difference $E_{FM} - E_{AFM}$ for C4a-X honeycomb-Kagome (H-K) super-lattices [Fig. 5.7(b-e)] suggests a systematic emergence of FM ordering between Gr-islands and a ferrimagnetic ordering between the two super-lattices. As evident in Fig. 5.7(b-e), the strong FM ordering is possible only if X is at B(N)-site for the honeycomb lattice made of C4a(C4b)-island. This observation actually reiterates the reason as discussed previously that the even membered -B-N- connectivity suppress the propagation of magnetic order and only odd membered -B-N- pathway enhances the strength. These results suggest [Fig. 5.7] that for $d \leq 4$ which allows a separation up to about 12Å between magnetic Gr-islands in the honeycomb lattice and up to about 10Å separation between nearest Kagome and honeycomb sites, strong FM ordering [Fig. 5.7(d,e)] in honeycomb lattice can occur. In fact, these results are valid for any general Cm-Cn H-K super-lattices, where Cm and Cn represent two types of magnetic graphene islands constituting the two lattices. The islands can be chosen to be similar or dissimilar, even if the islands in two sub-lattices are similar we note that there will be different numbers of islands for the two sub-lattices per supercell. Both examples have been demonstrated in sec. 5.5. As the strength of the FM order depends on d [Fig. 5.7(b-e)] this can also be understood as a competition between the inherent AFM order between the Gr-islands in the honeycomb lattice and the induced FM order by the

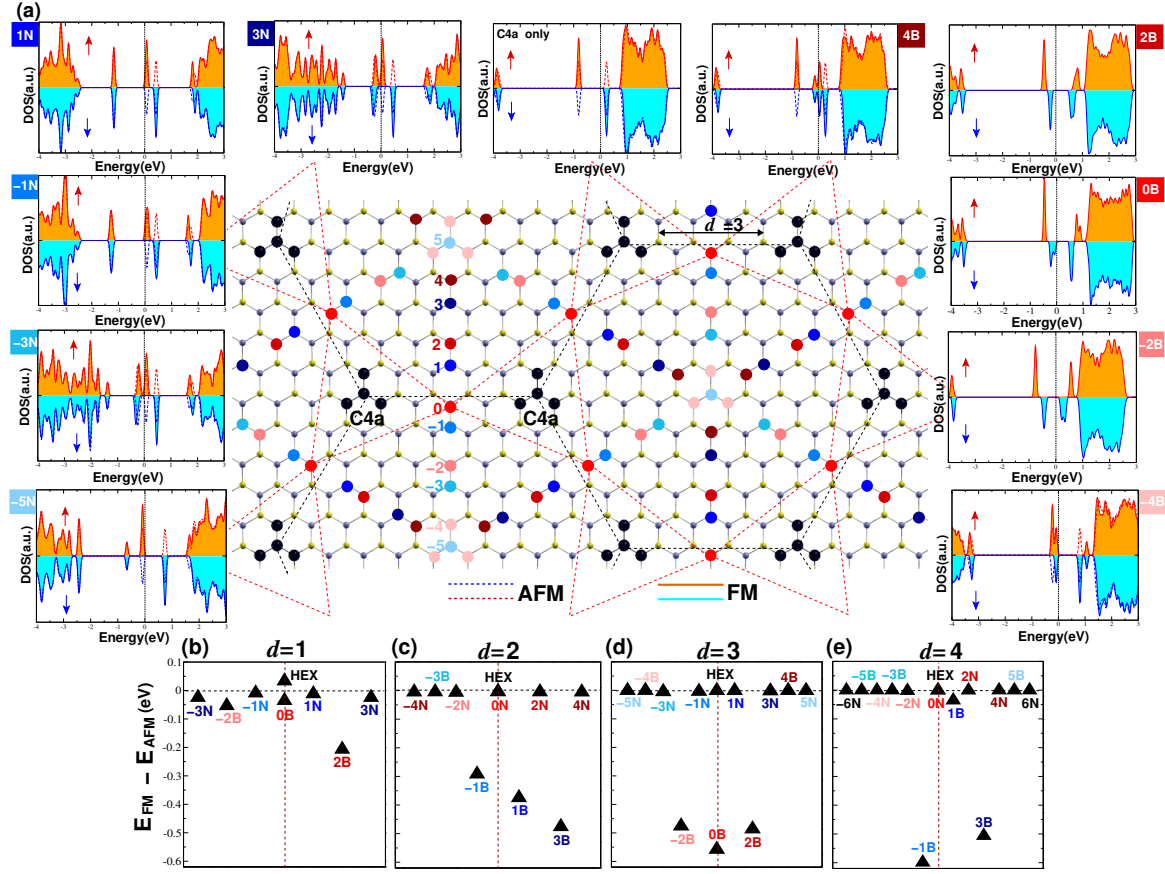


Figure 5.7: (a) Representation of inter-penetrating C4a-X honeycomb-Kagome superlattices for various intermediated substitution by C at X (B or N) sites for $d = 3$. Energy difference ($E_{FM}-E_{AFM}$) for different X with different separations of C4a islands, (b) $d=1$ (c) $d=2$ (d) $d=3$ and (e) $d=4$. $E_{FM}-E_{AFM} < 0$ implies FM order in honeycomb super-lattice.

Kagome lattice of X sites. Since, the strength of AFM order reduces with increasing d it leads to a peak for the FM order which reduces further with the increase of $d > 4$, implying a length scale up to nanometers.

5.4.1 Different phases due to ferromagnetic ordering

The switching of magnetic order in these Gr-hBN hybrid super-lattices has an important impact in their electronic structure in comparison to pristine graphene and hBN.

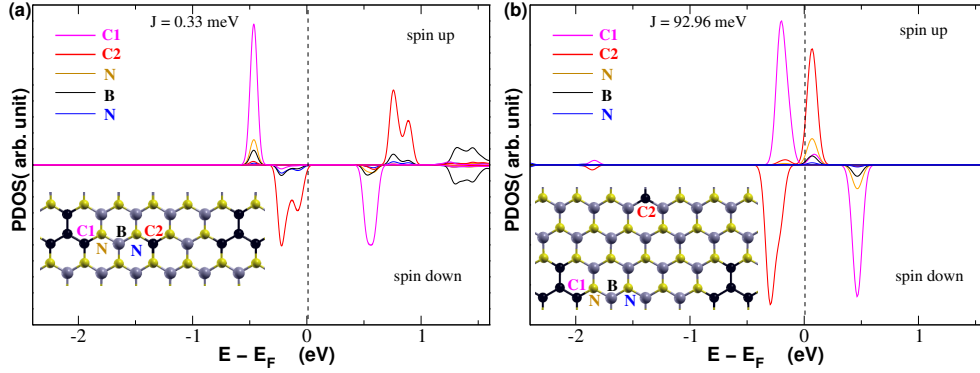


Figure 5.8: Projected density of states of $2p_z$ orbital for some of the inequivalent atomic sites (shown in inset) for C4a honeycomb super-lattice with X at (a) 0B and (b) 3N location of Fig. 5.7(a). The estimated coupling strength J is written in the inset.

In this honeycomb super-lattices, the FM ordering leads to FM-semiconducting (FM-Sc) to half-metallic phases depending on the position of X, whether it is at B or at N site as implied in DOS plot of Fig. 5.7(a). To understand this emergence of FM-Sc or half-metallic phases we resort to the orbital resolved projected density of states (PDOS). As evident from PDOS plot [Fig. 5.8(a,b)], the relative shifts of energies of (A) the $2p_z$ orbitals of edge C atom of the Gr-islands and (B) those of the C atoms at X site leads to these two regimes. For a general understanding, projected density of states corresponding to the sets of orbitals **A**, **B** is presented schematically in Fig. 5.9(a-d) by solid and dashed lines respectively. The relative energy shift of orbitals **A** and **B**, which are contributed from opposite spins, can be understood by noting whether they are hosted by C-atoms at B or N-site and the degree of their localization. Notably, the p_z orbitals at X-sites due to isolated substitution becomes more localized than those of the Gr-islands at honeycomb site and the amplitude of spin separation of energy due to onsite Coulomb repulsion depends on the degree of localization. Fig. 5.9(a,b) and Fig. 5.9(c,d) suggests similar properties of the C4a-X:(N,B) and C4b-X:(B,N) H-K super-lattices. Also the half-metallic and FM-Sc phases due

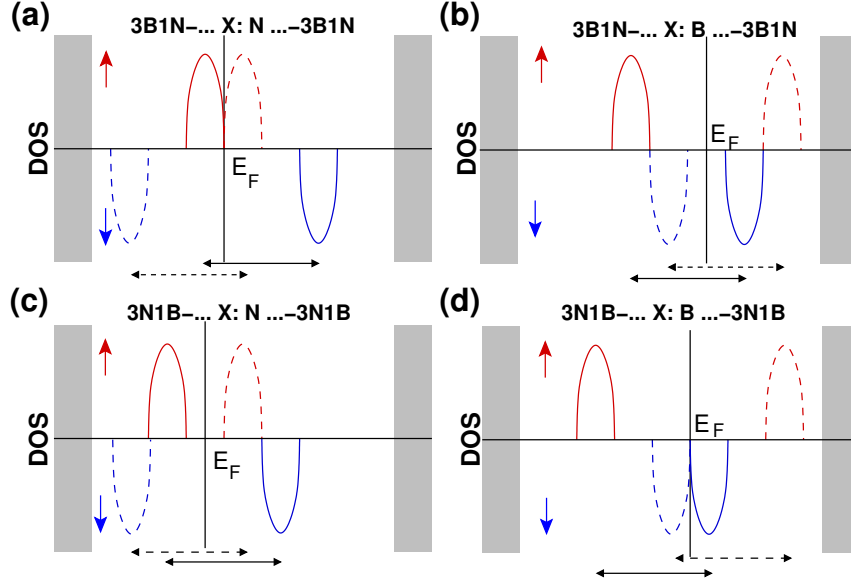


Figure 5.9: Schematic DOS to understand the evolution with different choices of Gr-islands and X (a)C4a-X:N (b)C4a-X:B (c)C4b-X:N and (d)C4b-X:B for representative study.

to X:N(B) and X:B(N) for Gr-islands C4a(C4b) are in agreement with DFT results shown in Fig. 5.7(a). This schematic representation thus suggests a more delocalized spin at X site as the key parameter for a more robust half-metallic window, which is possible if either the X sites are close to each other as seen in Fig. 5.7(a,4B,5N), or X sites are replaced by Gr-islands as discussed in sec. 5.5.

For all the systems the effective strength of exchange interaction J and the corresponding transition temperature are estimated within the Ising model of spin Hamiltonian [23] for honeycomb lattice. For FM ordered ground state the estimated temperature T_C [Eq. 5.2] indicates the possibility of existence of the proposed FM order at room temperature. In fact, all representative configurations having energy difference $(E_{FM} - E_{AFM}) \geq 0.3$ eV, in principle present possibilities of ferromagnetism at room temperature.

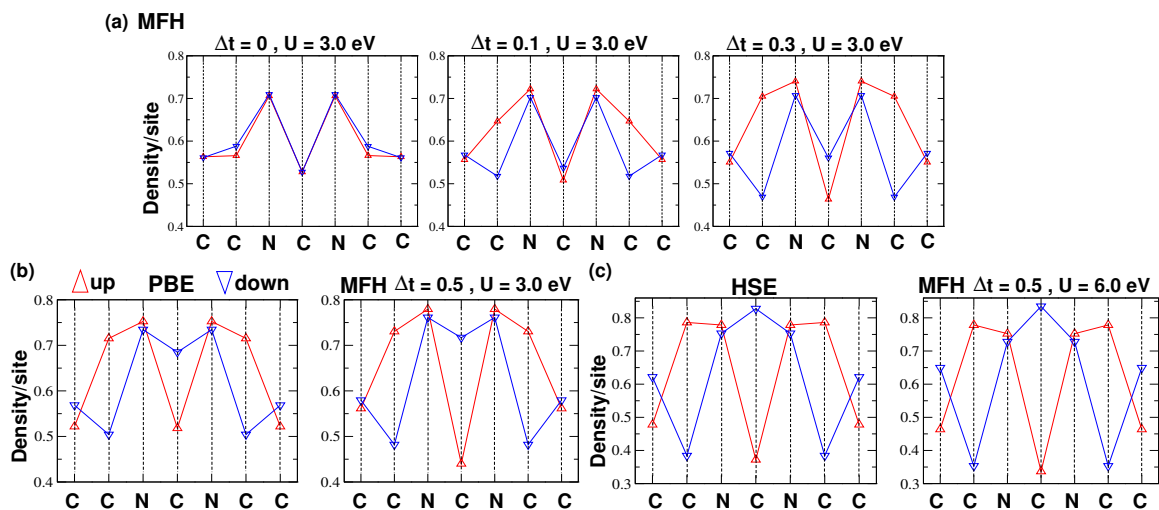


Figure 5.10: Occupancy of spin due to $2p_z$ electrons at sites along the C-N-C-N-C zigzag path due -N-C-N- connectivity between C4a islands calculated using PBE, HSE and from MFH at $U=3.0$ eV and 6.0 eV.

5.4.2 Confirmation with improved exchange-correlation functional

By using hybrid exchange-correlation functional(HSE) the enhancement of the effective J beyond its PBE value confirms the robustness of the FM ordered honeycomb lattice in the ground state. Fig. 5.10(a-c) clearly suggests that for FM ordering of the honeycomb lattice within MFH spin dependent hopping around the B-C and N-C bonds is indeed an important parameter. Densities (p_z only) obtained from Löwdin analysis using PBE/HSE for both the spins along the C-C-N-C-N-C-C pathway [Fig. 5.6(c)] matches well [Fig. 5.10(b,c)] for a finite Δt value. Since at high U limit Hubbard Hamiltonian evolves into a spin exchange Hamiltonian, it was possible to match PBE and HSE densities(both spin) along the zigzag pathway with MFH densities at $U=3.0$ eV [Fig. 5.10(b)] and $U=6.0$ eV [Fig. 5.10(c)] respectively, with a finite Δt . These agreements thus confirm the central role of Coulomb correlation driven spin dependent hopping in rationalizing the FM ordering between the Gr-islands of

the honeycomb lattice in the H-K double-lattice of Gr-islands in hBN.

5.5 Hybrid super-lattices with bigger graphene island

For generalization of the observed phenomena with C4-X H-K super-lattices, a similar systematic analysis has been done with bigger Gr-islands such as C9(6B3N) for the honeycomb lattice and up to C4 for the Kagome lattice. The energy difference $E_{FM} - E_{AFM}$ plotted in Fig. 5.11(a-c) for C9-X(B/N) shows a systematic emergence of FM ordering in honeycomb super-lattices and its evolution w.r.t island separation, d is similar to that observed for C4-islands in honeycomb lattice. The strong FM order only occurs with X:B[Fig. 5.11(a,b)] and due to its zigzag connectivity via odd number -B-N- sites with neighboring Gr-islands[Fig. 5.12(a)]. This observed similarity with C4 Gr-islands, therefore, generalizes the intermediate pathway for strong FM ordering as $-(2d+1 \text{ B, N})\text{-C}\text{-}(2d+1 \text{ B, N})\text{-}$. These results also suggest that in general if an odd number of magnetic Gr-islands (single C atom(C_1) or a patch(C_m , $m > 1$)), located within a length-scale of nanometer of each other within hBN, can be ferrimagnetically ordered with a finite magnetic moment, which is probably easier to observe. The strong FM order leads to FM-Sc phase for C9 H-K super-lattice, which is evident from Fig. 5.12(a). Here the orbitals near Fermi energy is from edge C-atoms of the C9 island and the Kagome X site[Fig. 5.12(b)], which is consistent with the schematic plot of DOS of Fig. 5.9(b). Similarly for Kagome site with X: N leads to half-metallic phase, although it is very weak beyond $d > 1$ as the energy difference is very less[Fig. 5.11(b,c)]. In Fig. 5.13 we have presented a few different combinations of Gr-islands in both honeycomb as well as Kagome lattices to exhaustively establish our observation of FM-order and mechanism of switching of

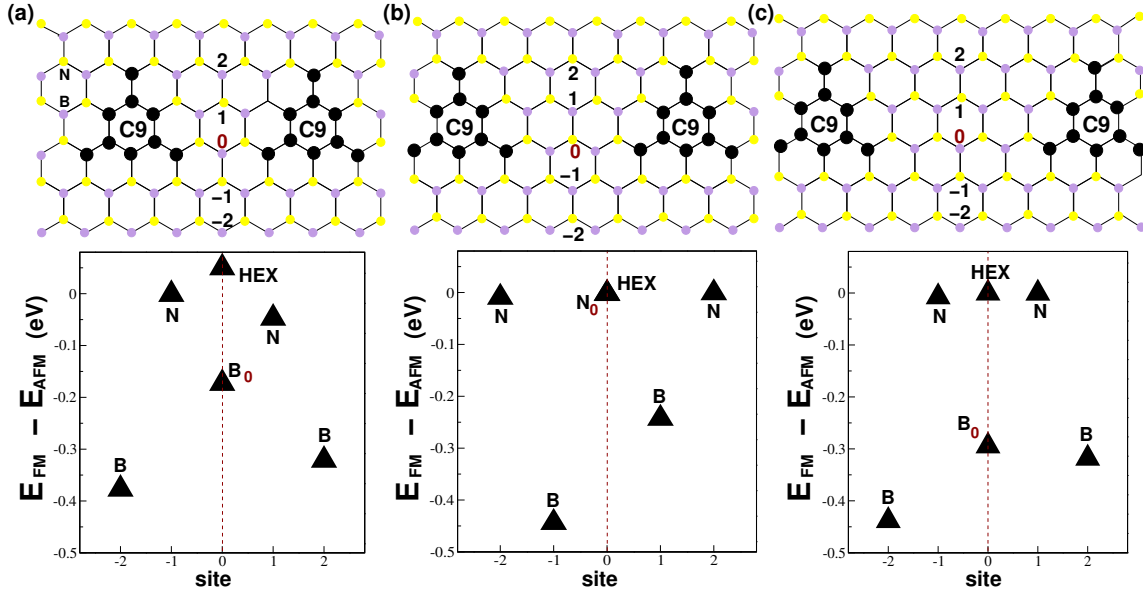


Figure 5.11: Schematic presentation of C9(6B3N) islands(upper row) with different X-location and island separation d . This is a part of full interpenetrating H-K superlattices. Energy difference ($E_{FM}-E_{AFM}$) for different X with different separations of C9 islands, (a) $d=1$ (b) $d=2$ (c) $d=3$, $E_{FM}-E_{AFM} < 0$ implies FM order in honeycomb super-lattice.

magnetic ordering as explained in previous sections. According to energy difference and total magnetization[Fig.5.13(f)] all configurations correspond to the FM ground state, which is also evident from FM ordering between honeycomb sites as shown in spin density profile[Fig.5.13(a-e)]. With enhanced substitution at N-site for the islands which constitute the Kagome lattice, the half-metallic window becomes more robust compared to single substitution[Fig.5.7(a)] and this systematic is indeed true irrespective of island configurations at honeycomb site[Fig.5.13(a,b,d)]. Whereas, for B-rich island at Kagome site always lead to FM-Sc phase with smaller as well as larger islands at honeycomb site[Fig.5.13(c,e)].

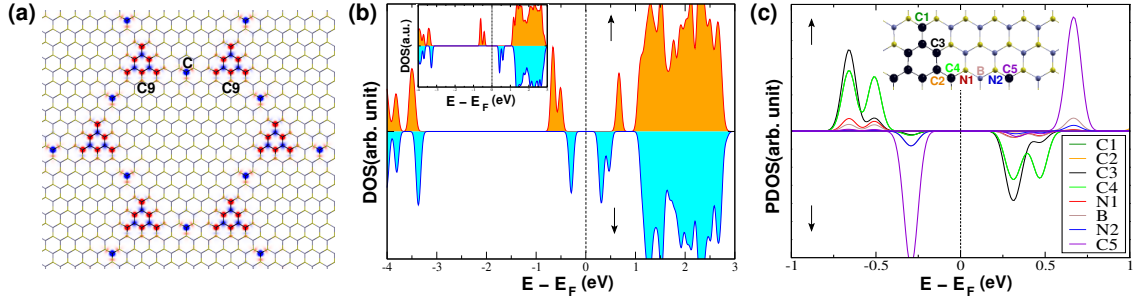


Figure 5.12: (a) Spin density and spin polarized (b) DOS, (c) PDOS($2p_z$ only) for C9-X:B H-K super-lattice with Gr-island separation $d=3$. DOS for honeycomb super-lattice is shown in the inset of (b) and all the inequivalent atomic sites for PDOS plot shown in the inset of (c).

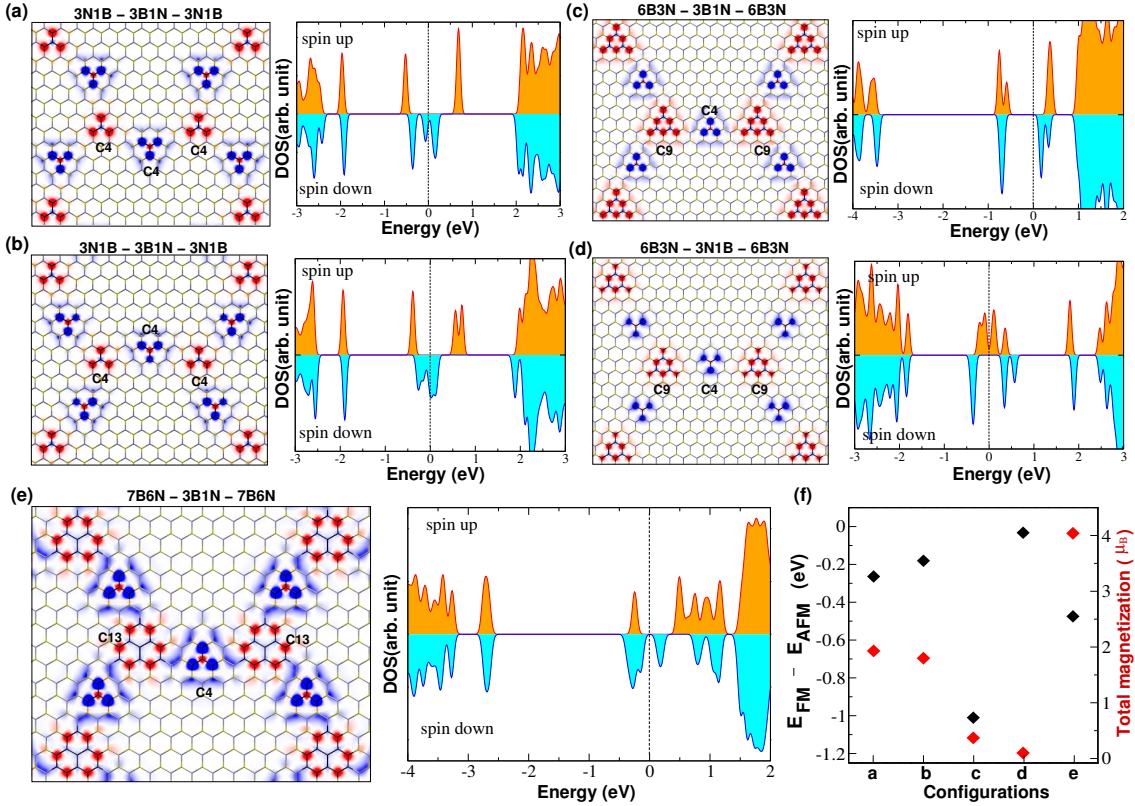


Figure 5.13: Spin density and spin-polarized DOS for hybrid super-lattice, consists of (a) 3N1B(H); 3B1N(K), (b) 3N1B(H); 3B1N(K), (c) 6B3N(H); 3B1N(K), (d) 6B3N(H); 3N1B(K), (e) 7B6N(H); 3B1N(K) graphene islands at honeycomb(H) and Kagome(K) site respectively, (f) energy difference ($E_{FM} - E_{AFM}$) and total magnetization of the lower energy configuration for all hybrid super-lattices as marked by a-e. $E_{FM} - E_{AFM} > (<) 0$ corresponds to AFM(FM) ground state.

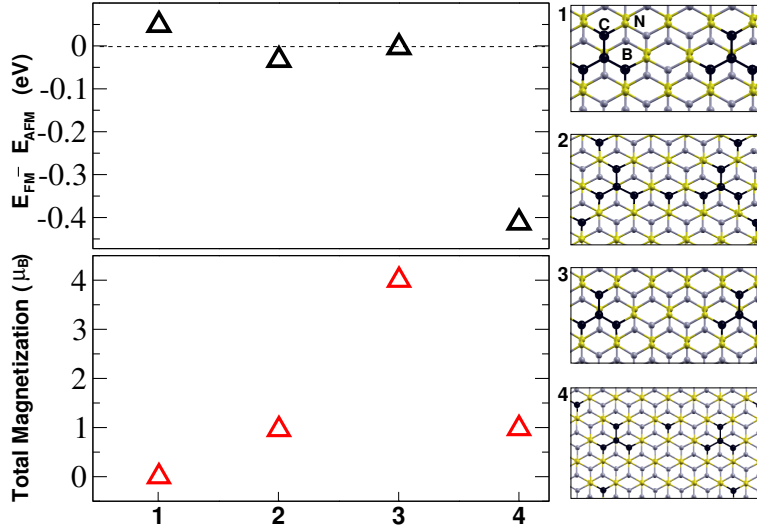


Figure 5.14: Energy difference($E_{FM}-E_{AFM}$) and total magnetization of the lower energy configuration for bilayer hybrid super-lattices as marked by **1-4**. $E_{FM}-E_{AFM} > (<)0$ corresponds to AFM(FM) ground state.

5.6 Effect of additional hBN layer

Here we probe the retention of the observed magnetic order in GR-hBN hybrid super-lattice due to presence of an additional hBN layer beneath. Since A-B stacking is known to be energetically favorable[24] for hBN bilayer systems, we have considered A-B stacking between hBN monolayer and Gr-hBN hybrid layer. From the energetics[Fig.5.14] it is clearly evident that the switching or enhancement of FM ordering in Gr-hBN hybrid layers[Fig.5.14(1-4)] remain intact in the presence of an additional hBN layer beneath. From the energetics and the spin densities[Fig.5.15(b,e)] it is clearly evident that the FM order and generic mechanism of mediation of magnetic order through -B-N- pathway remain preserved.

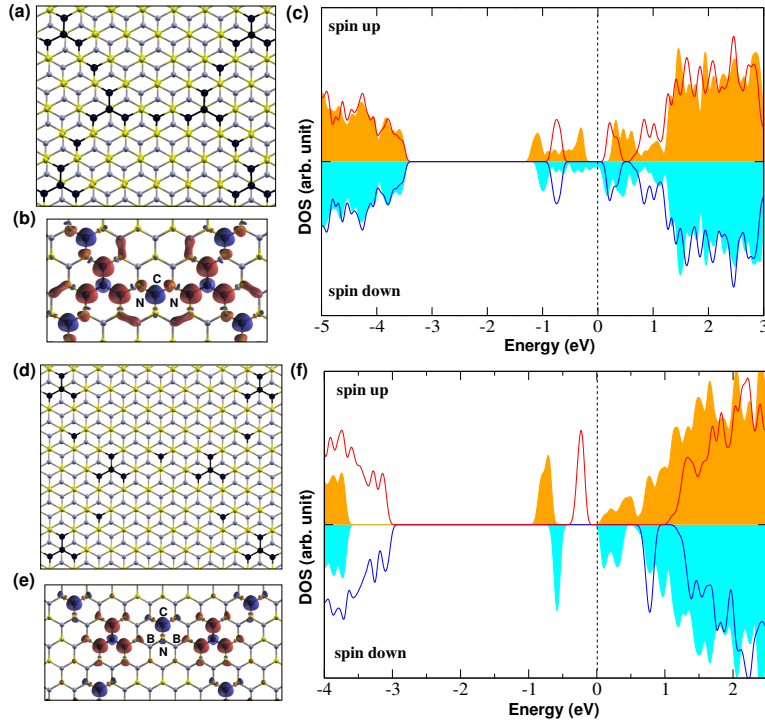


Figure 5.15: Bilayer hybrid super-lattices and spin density for (a,b)d=1 and (d,e)d=2 with d as mentioned in Fig. 5.7, spin-polarized DOS with (2,4 of Fig. 5.14) and without C(1,3 of Fig. 5.14) at intermediate (Kagome) sites for (c)d=1 and (f)d=3. Red and blue line corresponds to 1 and 3 configuration of Fig. 5.14, filled color represents the configuration 2 and 4 of Fig. 5.14.

5.7 Possible experimental realization

Hexagonal boron nitride with a patterned distribution of graphene islands are fast become experimentally realizable [Fig. 5.16]. The novel synthesis technique of formation of these Gr-hBN in-plane heterostructures imposes a high impact in the field of theoretical as well as experimental research. In recent years fabrication of graphene domain with controllable shape and size [13, 25, 11, 26, 27, 28] within hBN matrix makes them attractive for various applications. These precise fabrication processes and several modern measurement techniques in this nanoscale regime encourages our theoretical observation.

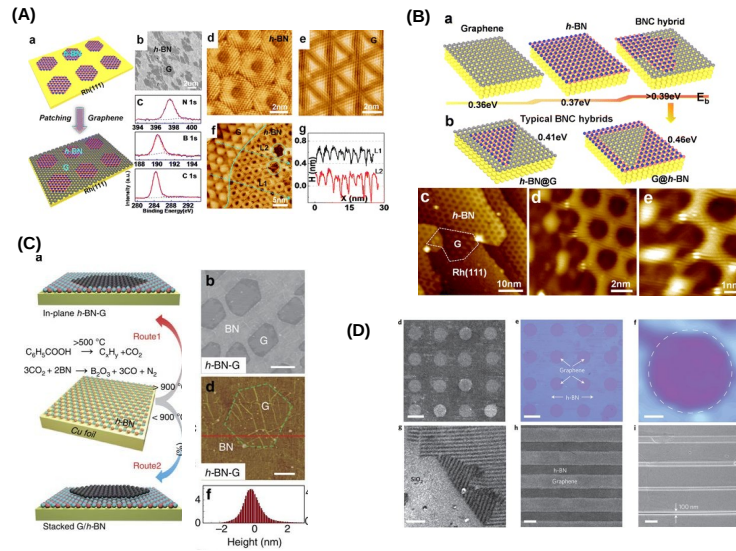


Figure 5.16: (A)(a) Schematic diagram of the patching growth. (b) SEM morphology of hybridized domains. (c) XPS spectra of B, N, C 1s core levels. (d,e)($V_T = -0.002$ V, $I_T = 23.00$ nA; -0.011 V, 6.30 nA) Atomically resolved STM images of pure h-BN and graphene on Rh(111), respectively. (f)(-0.200 V, 33.30 nA) Zoomed-in STM image at the boundary linking h-BN and graphene. (g) Cross-sectional profiles along L1 and L2 in (f) showing the apparent corrugations spanning over two analogues.[Ref. [25], (B)(a) DFT calculations of the binding energies (E_b) of graphene, h-BN, and BNC hybrids. (b) Two typical BNC hybrids of BN@G and G@BN. (c) ($V_T = 0.800$ V, $I_T = 0.02$ nA) Large-scale STM images showing the preferred linking of graphene to preexisting h-BN domains. (d) (0.700 V, 0.02 nA) and (e) (0.400 V, 0.02 nA) Sequential zoomed-in of (c)[Ref. [25], (C)(a) Schematic illustration of the temperature-triggered switching growth between in-plane h-BN-G and stacked G/h-BN heterostructures, defined as Route 1 and Route 2, respectively.(b)SEM image of a sample synthesized by Route 1, showing discrete hexagonal graphene islands embedded in h-BN. (d)AFM height images of h-BN-G after being transferred onto 300-nm-thick SiO₂ substrates, with corresponding height histograms and line sections shown in (f)The scale bars in d is 1[Ref. [28], (D)d-f, SEM image, optical image and Raman mapping of a graphene/h-BN array of circles, with graphene circles embedded in an h-BN matrix. Scale bars, 50 m (d), 50 m (e) and 10 m (f). g,h, SEM images of graphene/h-BN stripes. Scale bars, 50 m (g) and 10 m (h).i, SEM image of graphene/h-BN strip structure with graded strip dimensions, fabricated by FIB etching of h-BN and subsequent graphene growth. The widths of each strip, from top to bottom, are 1 m, 500 nm, 200 nm and 100 nm, respectively. Scale bar, 1 m. [Ref. [11]]

Bibliography

- [1] J. M. Pruneda, *Phys. Rev. B*, 81, 161409(R), **(2010)**.
- [2] Shaobin Tang and Zexing Cao, *Phys. Chem. Chem. Phys.*, 12, **(2010)**.
- [3] Somnath Bhowmick, Abhishek K. Singh and Boris I. Yakobson, *J. Phys. Chem. C*, 115, **(2011)**.
- [4] Ru-Fen Liu and Ching Cheng, *Phys. Rev. B* 76, 014405, **(2007)**.
- [5] Chong Zhao *et al.* , *Adv. Funct. Mater.*, 24, **(2014)**.
- [6] W Sheng, Z. Y. Ning, Z. Q. Yang and H. Guo, *Nanotechnology*, 21(38), **(2010)**.
- [7] Hongzhe Pan *et al.* , *New J. Phys.*, 18, 093021, **(2016)**.
- [8] E. H. Lieb, *Phys. Rev. Lett.* 62, 1201, **(1989)**.
- [9] Wei L. Wang, Sheng Meng and Efthimios Kaxiras, *Nano Lett.*, 8(1), **(2008)**.
- [10] Yuanyue Liu, Somnath Bhowmick, and Boris I. Yakobson, *Nano Lett.*, 11, **(2011)**.
- [11] Zheng Liu *et al.*, *Nature Nanotechnology*, 8, **(2013)**.
- [12] Jiong Lu, Lídia C. Gomes, Ricardo W. Nunes, A. H. Castro Neto and Kian Ping Loh, *Nano Lett.*, 14(9), **(2014)**.

- [13] Xianlong Wei, Ming-Sheng Wang, Yoshio Bando, and Dmitri Golberg, *ACS Nano*, 5(4), (2011).
- [14] Jian Zhou, Qian Wang, Qiang Sun and Puru Jena, *Phys. Rev. B*, 84, 081402(R), (2011).
- [15] Xiaowei Li and Qian Wang, *Phys. Chem. Chem. Phys.*, 14, (2012).
- [16] Xiaowei Li and Qian Wang, *Phys. Chem. Chem. Phys.*, 14, (2012).
- [17] Ashwin Ramasubramaniam, Doron Naveh, *Phys. Rev. B*, 84, 075405, (2011).
- [18] Mina Maruyama and Susumu Okada, *J. Phys. Chem. C*, 120, (2016).
- [19] O. V. Yazyev, *Reports on Progress in Physics*, 73, 5, (2010).
- [20] Zheng, Fawei; Sasaki, Ken-ichi; Saito, Riichiro; Duan, Wenhui; Gu, Bing-Lin, *Journal of the Physical Society of Japan*, 78, 074713, (2009).
- [21] Tomoaki Kaneko, Kikuo Harigaya, and Hiroshi Imamura, *J. Phys. Soc. Jpn.*, 82, 083710, (2013).
- [22] Tomoaki Kaneko and Kikuo Harigaya, *J. Phys. Soc. Jpn.*, 82, 044708, (2013).
- [23] J. Baxter, *Exactly Solved Models in Statistical Mechanics* (Academic Press, London, (1982).
- [24] Yoshitaka Fujimoto and Susumu Saito, *Physical Review B*, 94, 245427, (2016).
- [25] Yabo Gao *et al.*, *Nano Lett.*, 13(7), (2013).
- [26] Soo Min Kim *et al.*, *Nano Lett.*, 13(3), (2013).
- [27] Mengxi Liu *etal.*, *Nano Lett.*, 14(11), (2014).
- [28] T. Gao *et al.*, *Nat. Commun.*, 6:6835, (2015).

Chapter 6

Electrocatalysis with hybrid layers made of 2p-block elements

6.1 Introduction

Two dimensional materials have received much attention as a promising host for physics and chemistry at nanoscale. In these systems, the strong co-planarity of atoms on account of their sp^2 hybridized orbitals makes them chemically inactive on their own, but controlled chemistry with appropriate functionalization of these materials has been long envisaged to be advantageous [1, 2, 3, 4] owing to the large surface to volume ratio that they offer. The most popular means of functionalization has been through substitutional doping [5, 6, 2, 7] by neighboring elements in the 2p block, such that, the intra-layer coordination remains intact while the extra electron or hole acquired in the process facilitates the emergence of new physical and chemical properties like magnetism and electrocatalysis [8, 9]. In fact, from understanding of previous work, as well as in course of this work, we show that these two properties are intertwined and sourced inherently at Coulomb correlation, unrevealing the

underlined mechanism is the main motivation of this chapter.

In past few years, primarily boron(B) and/or nitrogen(N) doped graphene[10, 11, 12, 13], carbon nanotubes[14, 15] have been extensively explored as platform for electrocatalysis[16, 8]. Conversely, carbon(C) doped hBN is also expected to offer similar platform since the neighborhood of a C dopant in hBN is similar to that of an activated C in graphene due to co-doping[17, 11] by B and N around it. One important demerit of hBN as cathode is its insulating nature, which would impede the flow of electron to active sites. However we envisage solution of this problem by introducing islands of graphene in hBN. Indeed formation of graphene islands(Gr-islands) due to successive substitution of C in hBN has been experimentally observed[18, 19, 20, 21, 22]. First principle studies reported so far are based on isolated substitution, [23, 24] which therefore do not represent the true nature of electrocatalysis offered by C-doped hBN.

Accordingly, in this work we focus on chemical activation of islands of graphene in hBN. We study a representative variety of configurations with substitution by C in hBN starting from isolated to big C-islands to rationalize different scenarios of chemical activation down to atomistic details. In this chapter, we present a comprehensive survey of possible active sites from analysis of bond order calculated from mean-field Hubbard model within the tight-binding framework. Detail mechanism of chemical activation and catalytic support to oxygen reduction(ORR) and evolution reactions have been understood from calculation of free energies and construction of spatially localized Wannier function from first principles. The primary goal of this work has been to propose a metal-free alternate to the precious metal used in cathodes of fuel cells, where ORR plays the central role. In the process we also propose a quantitative framework to estimate the degree of chemical activation.

6.2 Calculation details

All equilibrium configurations and energetics are obtained from DFT based first principles calculation[sec.2.2.3], wherein, wave functions of valence electrons are expanded in plane wave basis and the effect of core electrons can be approximated by a class of maximally smooth *ultrasoft*[sec.2.2.2.2] pseudopotentials which substantially reduce the range of plane wave basis required for their adequate representation. Exchange-correlation contribution to total energy is approximately estimated using gradient corrected Perdew-Burke-Ernzerhof[25] functional. Configurations of substitution by C is considered in 8×8 hBN supercell. Total energies are minimized using the BFGS[sec.2.2.2] scheme and converged with plane wave cutoff more than 800 eV, k-mesh in effect up to 40×40 per pristine unit cell and forces less than 10^{-4} Rydberg/Bohr per atom. Physisorbed configurations have been further relaxed by incorporating dispersion interaction[sec.2.2.3.2].

The nature and degree of chemical activation due to substitution by C is estimated by studying the evolution of sub-shell filling and charge neutrality of atoms, estimated through partitioning of charge density in spatially localized Wannier functions(WFs) as detailed in sec.2.4.1.1.

Formation energies of the substitution configurations are estimated per C atom as:

$$[(E_{doped} - E_{undoped}) + n_N \mu_N + n_B \mu_B - (n_N + n_B) \mu_C] / (n_N + n_B), \quad (6.1)$$

where E_{doped} and $E_{undoped}$ are total energies of the hBN system with and without substitution by C. μ_C and μ_N are chemical potentials estimated realistically as energy per atom in graphene and N_2 respectively. μ_B is calculated as $\mu_{hBN} - \mu_N$ where

μ_{hBN} is approximated as total energy per B-N pair in hBN considering N-site rich environment [26]. Total energies are obtained from DFT calculation.

Adsorption energies for adsorbate estimated from total energies(E) as calculated from DFT as,

$$E_{ads} = E_{substrate+X} - E_{substrate} - E_X, \quad (6.2)$$

where X is adsorbed species and substrate corresponds to different C substituted hBN configurations.

Gibb's free energy of reaction coordinates are evaluated as [27]:

$$G = E + ZPE - TS, \quad (6.3)$$

where E is total energy, $ZPE(= \sum_i \hbar\omega_i)$ being the zero point energy with ω_i being the frequency of the i -th phonon mode calculated using first principles [sec. 2.2.3.1], T is fixed at room temperature, and entropy S taken to be non-zero only for molecules in gas phase for which standard literature [28] has been followed.

6.2.1 Bond order calculation

We propose that the reactivity of active sites can be understood by estimating bond order(BO) [29] involving the active site. BO is a measure of charge distribution along the bond. A bond with higher BO value is more stable and thus less active towards reactants. In past few decades, several approaches [30, 31, 32, 33, 34] have been developed for calculation of BO although, most of them have evolved around the concept of orbital overlap population [30, 35] originally defined within the realm of molecular orbital(MO) theory [31, 32] and later formulated in terms of density matrices [36]. Much elegantly, BO was connected to the exchange component of two particle density, [33] which was also subsequently extended to describe unpaired electrons [37]. Recently, an

effective interpretation of BO has been proposed based on the partitioning of charge and spin densities[34].

However, we have resorted to conventional definition of BO based on MO theory[29] as,

$$BO = \frac{N_b - N_{ab}}{2}, \quad (6.4)$$

where N_b and N_{ab} are occupation of bonding and anti-bonding orbitals. To estimate N_b and N_{ab} we resort to single orbital mean-field Hubbard(MFH) Hamiltonian [sec.2.3.4.1], which is known to be a good approximation for unhybridized p_z orbital of 2p-block elements[19]. In the basis of single p_z orbital per site for each spin we rewrite the $|\psi_b\rangle$ and $|\psi_{ab}\rangle$ as,

$$|\psi_b\rangle = \frac{1}{\sqrt{2}} \begin{pmatrix} 1 & 1 & 0 & 0\dots \end{pmatrix}^T, |\psi_{ab}\rangle = \frac{1}{\sqrt{2}} \begin{pmatrix} 1 & -1 & 0 & 0\dots \end{pmatrix}^T. \quad (6.5)$$

The occupation of electrons in bonding(N_b) and anti-bonding(N_{ab}) orbitals for a single bond is calculated from projection as,

$$N_b = \sum_m f_m \langle \psi_m^{MFH} | \psi_b \rangle, N_{ab} = \sum_m f_m \langle \psi_m^{MFH} | \psi_{ab} \rangle, \quad (6.6)$$

where m is the number of atomic sites, f_m is the occupation factor and $|\psi_b\rangle$, $|\psi_{ab}\rangle$ are bonding and anti-bonding basis respectively. Average BO (ABO) of each atomic site is then estimated by averaging over BOs of all the nearest neighbor(n-n) bonds made by the atom as

$$ABO = \frac{1}{N_{nn}} \sum_{i=1}^{N_{nn}} BO_i. \quad (6.7)$$

A systematic analysis based on ABO has been discussed in the following for some small systems.

The estimated ABO, starting from a C-C trimer to a big C-island, shows a sys-

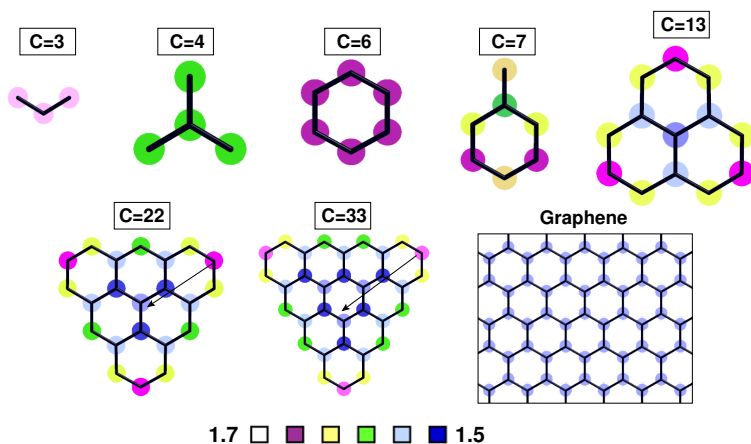


Figure 6.1: Average bond order (ABO) for isolated C-island starting from C=3 to C=33 atoms and graphene sheet. Color scheme represents a different order of sharing of electrons between the neighboring sites. The arrow shows the ABO variation from edge towards the middle (bulk) region.

tematic evolution with respect to system size [Fig. 6.1]. Agreement of the ABO value of the single hexagonal ring (C=6) i.e. $ABO = 0.67$ (π -only) with that of benzene [38] and for graphene (0.525, π -only) [38] with MO calculation confirms the usefulness of our simple approach.

As evident from the trend of ABO values implied in Fig. 6.1 with increasing island size the C-atoms in the bulk of the islands should behave increasingly like in pristine graphene, whereas the C-atoms at the vertices behave increasingly like those in C=3 trimer.

However the ABO values of these C-atoms modify substantially as we considered them embedded in hBN as discussed in sec. 6.3.2.1.

6.3 Carbon doped hexagonal boron nitride

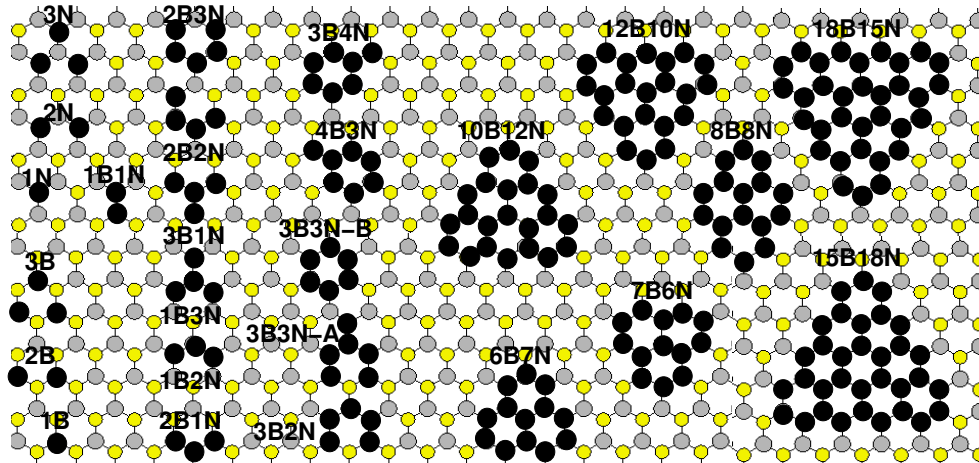


Figure 6.2: Representative variety of configurations with substitution by carbon in hexagonal boron nitride.

For our systems of interest, we consider a representative variety of configurations of substitution by C in hBN, with an increasing number of C atoms as described in Fig. 6.2. A general nomenclature of $(n_B + n_N)C = n_B B n_N N$ has been used to denote the number of B(n_B) and N(n_N) sites substituted by C in the immediate neighborhood of each other. Thus, $n_B = 0$ or $n_N = 0$ would mean substitution only from next nearest sites constituting the N or B sub-lattices, whereas, $n_B = n_N$ would imply substitution from nearest neighboring sites such that all the C atoms can in principle have a double bond in pairs. By the same argument, $n_B \neq n_N$ would imply $|n_B - n_N|$ number of C atoms to have all three single bonds and would thereby have incomplete sub-shell filling unless negatively charged. It is the ratio of number of C-C single and double bonds (C=C) and the distribution of C atoms with all single bonds, which determine the energetics of substitution.

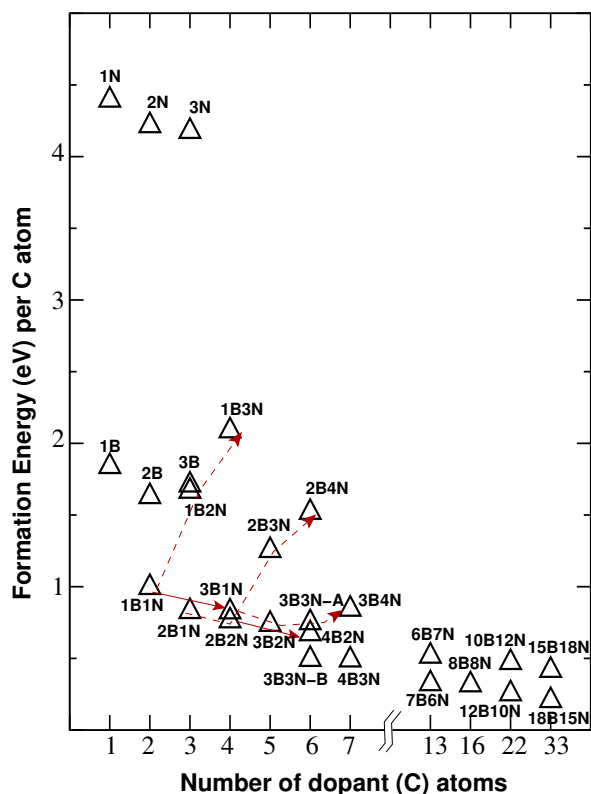


Figure 6.3: Formation energy (per C atoms) of C substituted hBN configurations shown in Fig. 6.2. The dashes and solid arrows show the variation in average formation energy with increasing number of N and B atoms respectively for the fixed number of B and N atoms.

6.3.1 Energetics of substitution

Substitution energy of representative configurations have been calculated using Eq. 6.1. As evident from Fig. 6.3 substitution by C in hBN is endothermic. Substitution by C is more favorable at B site than at N site, primarily because the dissociation energy of C-N σ -bonds are higher than those of C-B σ -bond owing to the ascending order of electronegativity from B to N, which is also reflected in the fact that C-B single bond is about 10% longer than a B-N bond, while the C-N bond is 5% smaller than B-N bond. It is thus obvious that replacement of B-N bonds by C-B bonds to be energetically costlier than replacement of B-N bonds by C-N bonds, which explains

why the substitution of B by C is energetically more favorable than the substitution of N by C. Thus, in general, the average (per C atom) formation energy of C doped regions should increase at a higher rate with increasing n_N than with increasing n_B , which is consistent with the trends highlighted in Fig. 6.3. Notably, $n_B = n_N$ indeed leads to C=C bonds of order 2 as evident from the distribution of Wannier centers(WCs) shown in Fig. 6.9(f). Since a C=C bond is about 10% shorter than B-N bonds, compressive strain due to C=C bonds will compensate the expansive strains due to the C-B and C-C single bonds, thus resulting into low formation energy of C doped regions with $n_B = n_N$. Furthermore, with equal no.of substitution by C i.e. $n_B = n_N = 3$, in closed loops is more preferable over chains owing to the uncompensated strain which is present around the terminal C atoms of a chain. This is clearly evident in Fig. 6.3 and explains the preference for substitution by C from nearest neighboring sites, leading to the formation of Gr-islands in hBN [39, 40]. Fig. 6.3 also suggests that with increasing size of the even membered patch($n_B = n_N$), the difference in energy required for substitution of an N or B by C at the edge of the even membered patch decreases. Therefore it is realistic to consider bigger C-islands i.e. Gr-islands in hBN with $n_B \neq n_N$.

In this chapter, we will focus on different Gr-islands starting from C=3 to C=33, considering both B-site rich($n_B > n_N$) and N-site rich($n_N > n_B$) configurations of C substitution. Along with that, single site(1B & 1N) substitution has been calculated as a reference for discussion in context with published literature.

6.3.2 Chemical activation

To study the scenarios of chemical activation due to the substitution of n_B and n_N number of B and N atoms by C in hBN, it is reasonable to expect that for $n_B \neq n_N$ there can be at least $|n_B - n_N|$ number of active C atoms since each of the rest of

the $2 \cdot \text{Min}(n_B, n_N)$ number of C atoms can in principle make one C=C bond each. Their activation is primarily rooted at their unpaired p_z electron since these C-atoms will be constrained to have only C-C σ -bonds with their neighbors. However, the net activation due to the $|n_B - n_N|$ active sites will be distributed across the C-atoms primarily over the zigzag edges of the islands. The active C atoms are thus likely to be located at the graphene hBN interface[21, 41].

In Table.6.1 we have listed adsorption energies[Eq.6.2] of H atom and few common radicals on an isolated C due to a single substitution(1C) as well as on the most active C in a bigger island made of twenty two C-atoms(22C). At this point, the most active site is defined as the site which offers the strongest adsorption, which we substantiate formally in the following[sec.6.3.2.1]. Since the adsorbing site is a C-atom it is expected to observe different trends in adsorption of species which have higher or lower electronegativity compare to C. Accordingly, we find that for species which are more electronegative than C such as N and O adsorbed more strongly on C@B site than on C@N site, whereas species with lower electronegativity like H adsorb strongly on C@N site than on C@B site. Reduction in adsorption energy on 22C compared to that on 1C also suggests moderation of activation in bigger Gr-islands in general.

Species	1B(C@B)	1N(C@N)	12B10N(C@B)	10B12N(C@N)
<i>H</i>	-4.63	-5.06	-3.38	-3.67
<i>OH</i>	-4.52	-3.78	-3.10	-2.81
<i>OOH</i>	-3.06	-2.35	-1.67	-1.34
<i>CH₃</i>	-3.69	-3.79	-2.38	-2.54
<i>NO₂</i>	-2.27	-2.09	-1.07	-0.79
<i>NO</i>	-1.65	-1.64	-0.53	-0.60

Table 6.1: Adsorption energy in eV.

6.3.2.1 Average bond order(ABO) as a measure of activation

In Fig. 6.4 we have plotted the adsorption energy of atomic H on all the inequivalent C-atoms in a magnetic and non-magnetic Gr-island embedded in hBN. As discussed in the previous chapter[sec. 5.3] Gr- island with $n_B \neq n_N$ will have a net magnetic moment of $|n_B - n_N| \mu_B$. Fig. 6.4 clearly implies a higher level of activation for the magnetic Gr-islands thus implying an intimate connection between chemical functionality and magnetism of C doped hBN, which we explore in detail in sec. 6.3.2.3. We, therefore, focus henceforth exclusively on magnetic Gr-islands in hBN.

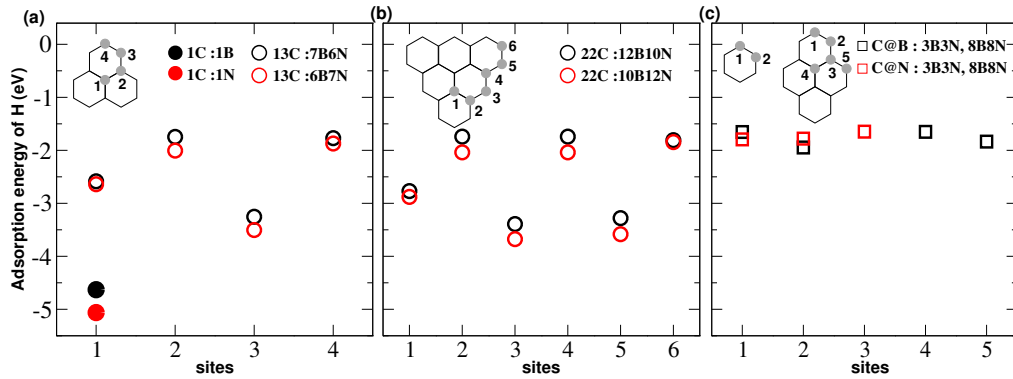


Figure 6.4: Adsorption energy of H-atom at inequivalent sites(gray filled circle) of (a)1C and 13C, (b)22C, (c)6C and 16C Gr-island embedded within hBN.

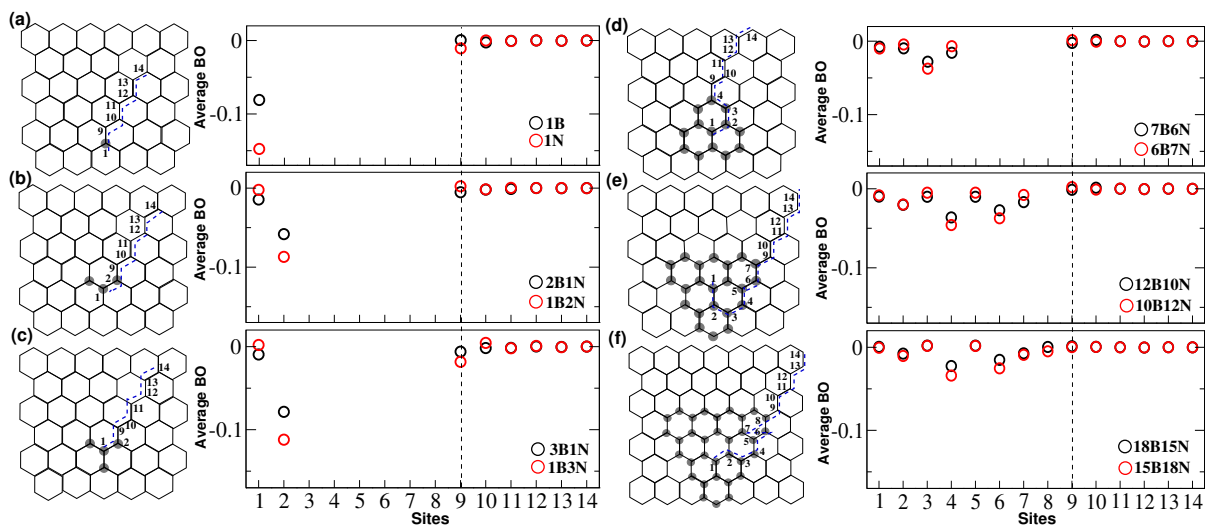


Figure 6.5: Average bond order (ABO) values at different sites in reference of pristine graphene (for C-site) and hBN (B,N-sites). ABO values at different sites for different C-substitution (gray circle) configurations: (a) single C (1C), (b) 3C, (c) 4C, (d) 13C, (e) 22C and (f) 33C, where red (black) circles represent the N-site rich (B-site rich) substitution and blue dotted lines define the sites as written in x-axis of all plots.

We now demonstrate that the active sites can be easily identified by calculating their ABOs. In Fig. 6.5 we have plotted the ABO values for the inequivalent C-atoms. Notably, Fig. 6.5(d,e) are plots the ABOs of the chemically active sites evident in Fig. 6.4(a,b) respectively. The agreement in trends of chemical activation of the inequivalent C-atoms and those of their ABOs suggest that the latter is an efficient marker of the level of chemical activation of each site.

Since a lower value of ABO of a site implies increased availability of electron at that site, Fig. 6.5 indeed suggests that the sites with lowest ABOs are the most active, as evident from comparison of Fig. 6.4(a,b) and Fig. 6.5(d,e). Fig. 6.5 unambiguously implies lowering of activation with increasing size of magnetic Gr-islands as also evident in terms of H-adsorption on 13C and 22C depicted in Fig. 6.4(a,b) respectively. Also as we see from Fig. 6.5(a) to (f), the relative difference of ABOs between equivalent C at N(C@N) and C at B(C@B) sites reduce with increasing size

of Gr-islands in general. Therefore active sites with a modest level of activation can be available at the zigzag interface of magnetic Gr-islands. Fig.6.5 suggests that the most active C atoms are likely to be found near the middle of zigzag edges as also implied in Fig.6.4. As per Fig.6.5 the degree of activation of such sites converges for islands of size beyond few nm^2 .

6.3.2.2 Activation as a function of electronegativity

In principle, the degree of activation would also depend on change in magnitude of ABOs upon adsorption, since enhancement of ABOs would essentially imply increased in-plane delocalization of p_z electrons leading to lowering of kinetic energy. In Fig.6.6 we therefore plot the change in ABO(ΔABO) which is $(ABO_{final} - ABO_{initial})$, where “initial” and “final” denotes in-plane ABO before and after adsorption. In Fig.6.6 we have plotted ΔABO as a function of onsite energy of the adsorbed atom with the aim of studying the variation of activation as a function of adsorbed species as listed in Table.6.1. We note that the trend of switching of favorable adsorption site(C@N or C@B) for species with higher and lower electronegativities compare to that of C, as evident in Table.6.1, is also present in the plot of ΔABO about the onsite energy of C which is set to zero. The switching is evident by noting that for onsite energy > 0 , which implies electronegativities lesser than that of C, adsorption on C@N site is more favorable as also seen in Table.6.1, whereas for onsite energy < 0 , which implies electronegativities higher than that of C, adsorption is more favorable on C@B site.

6.3.2.3 Correlation between chemical activation and magnetism

In this section, we explore the magnetic origin of the variation in activation of different inequivalent C-atoms in Gr-islands in hBN. In Fig.6.7 we have plotted the density of states(PDOS) projected on p_z orbitals for both the spins. We see in Fig.6.7 that the

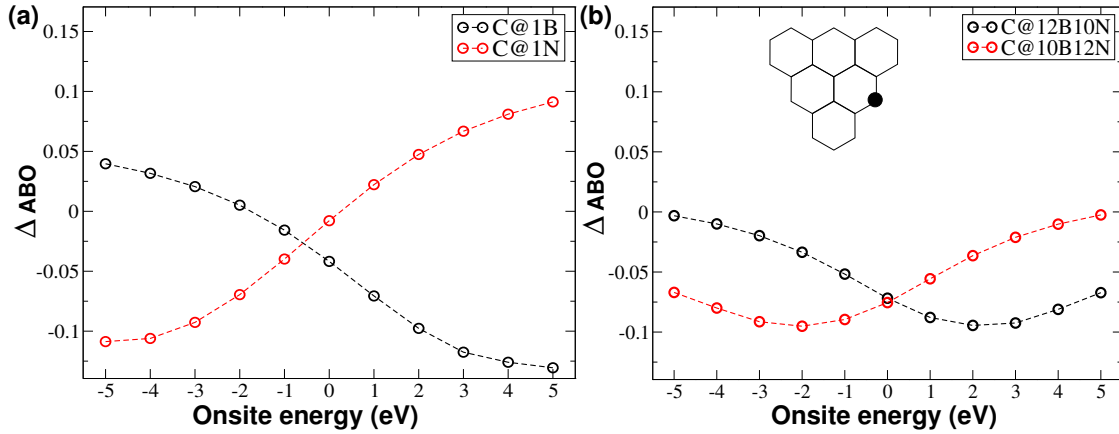


Figure 6.6: Variation of in-plane ABO with respect to different onsite energies for representation of adsorbed species at that site and ABO of that adsorbed species(inset) with (a)1C@1B and 1C@1N, (b)22C@12B10N and @10B12N. Here red(black) color represent N-site rich(B-site rich) configuration.

splitting in energy of the spin-polarized $2p_z$ orbitals are the highest in 1B and 1N followed by that of most active sites in 13C and 22C, implying an undeniable role of Coulomb correlation in rendering those C-sites chemically active.

In Fig. 6.8, we have compared the difference of ABO of the C-sites from that of graphene as a contour, with spin densities calculated from MFH and DFT. The sites with higher contour values of ABO difference are the most active sites and also has the highest spin densities. This agreement between first principles results and MFH based analysis gives us confidence about the robustness and generality of the proposed BO based approach in discussing chemical activation.

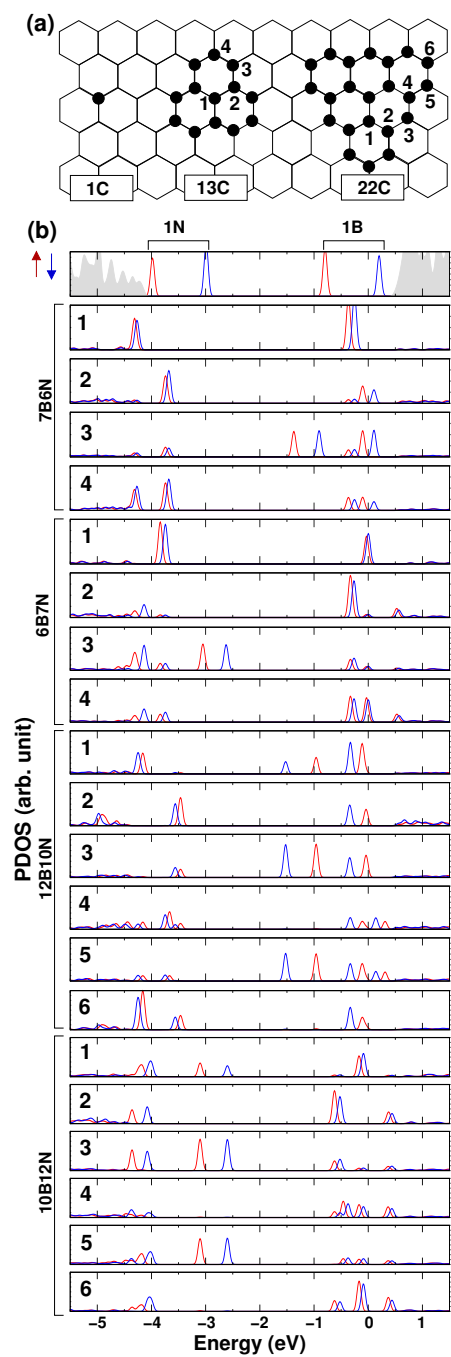


Figure 6.7: (a)Representation of inequivalent sites for PDOS plot, (b)PDOS for up(red) and down(blue) spin for all sites mentioned in (a). Gray shade corresponds to total DOS of pristine hBN.

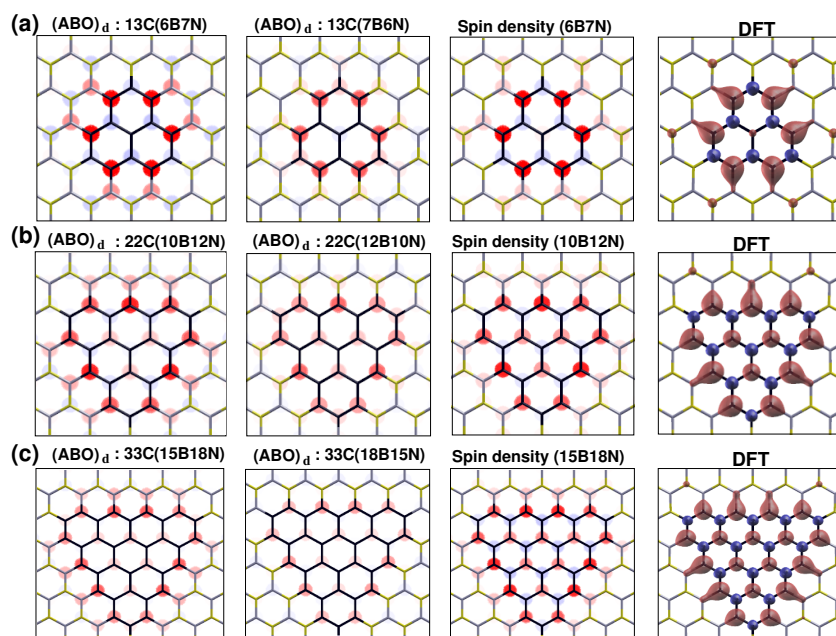


Figure 6.8: Contour plot of ΔE_{ads} : ABO difference w.r.t pristine graphene and hBN for N-site rich and B-site rich configurations, spin-density from MFH calculation and DFT for N-site rich configurations respectively for (a)13C, (b)22C, and (c)33C Gr-island embedded within hBN.

The variation in spin density of the inequivalent sites is in agreement with the variation of their activation as calculated from adsorption energies of H-atom, [Fig. 6.4] as well as from ABOs [Fig. 6.5]. Therefore, the ABO analysis and spin density in agreement suggest two most active sites in each of the three zigzag edges of triangular island 33C [Fig. 6.8(c)].

6.3.2.4 Orbital view of chemical activation

The underlying mechanism of chemical activation can be understood from spatially localized Wannier functions (WFs) and distribution of Wannier centers (WCs) [sec. 2.4.1.1]. WCs plotted in Fig. 6.9(b-e) suggests single C-N or C-B bonds in case of isolated substitution at B or N site, leading to an incomplete sub-shell filling of those C atoms and localization of their $2p_z$ electrons, which is consistent with our discussion in sec. 6.3.2.

Those C atoms will thus be chemically active in an attempt to achieve complete sub-shell filling and reduce the kinetic energy of the $2p_z$ electrons by engaging them in a covalent bond. Activation of these C atoms is thus a result of the tendency to maximally retain the charge neutrality and sub-shell filling of the surrounding atoms in hBN, thus constraining C-N or C-B bonds of order one. Interestingly, spin resolved WCs[Fig.6.9(b-e)] suggests charge redistribution for the spin which is absent(present) on C@N(C@B), amounting to depletion(accumulation) of the same spin in the sub-lattice made of N(B) atoms. as evident in Fig.6.9(b,c) and Fig.6.9(d,e). This can be understood by noting that the increase in B-N bond order for spin-2 in effect imply partial withdrawal of electron from N and transfer to B, leading to net non-zero spin-1 (spin-2) on N(B) sites respectively, thus leading to separation of spin between two sub-lattices locally around the C-atom. Note that before substitution both spin-1 and spin-2 are localized at N-site, but after substitution, the localization of only spin-1 in N-sites remain preserved while the spin-2 redistribute in an attempt to localize at B-site in the vicinity of substitution.

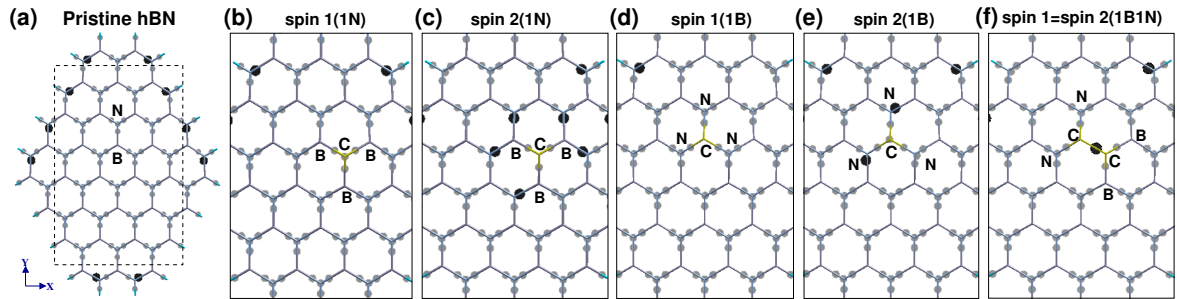


Figure 6.9: Planar projection of Wannier centers in hydrogen passivated patch of hBN with: (a)no doping, with substitution by C of (b-c)single N, (d-e)single B, (f)neighboring BN-pair. The smaller(bigger) translucent circle represents one(two) WC(s) each representing one electron.

Such spin separation is known to be driven by correlation due to onsite Coulomb repulsion between electrons of opposite spins, although, in pristine hBN, this is com-

pletely suppressed [Fig.6.9(a)] by the large difference in electronegativity of B and N. Notably, increase in B-N bond orders also causes deviation from charge neutrality and sub-shell filling of B and N atoms of the hBN matrix around activated C-site. The Motivation of activation of C-site also emerges from the fact that engaging the unpaired electron of C in covalent bond through chemisorption on C[Fig.6.12(a,d)] would quench the spin separation and thereby restores charge neutrality and sub-shell filling of the host atoms around C-site.

Fig.6.9(b-e) suggests that chemisorption at C can be exothermic due to lowering of the kinetic energy of the unpaired electron as it forms bond, and lowering of potential energy due to quenching of localization of the unpaired electron, and also due to restoration of charge neutrality and sub-shell filling in the rest of hBN sheet. Coulomb correlation thus play a non-trivial role in activating C atoms at B or N site, and the degree of activation will in part be governed by the level of correlation in the two cases. Evidently, correlation is more in case of C@B [Fig.6.9(e)] than that in case of C@N [Fig.6.9(c)], since the occupied sites (C and N) are nearest neighbors, in the former and they are next nearest neighbors in the latter. This microscopic description based on WFs enriches the description of activation proposed in terms of ABOs. In fact, the evolution of BOs as apparent from the redistribution of WCs upon substitution are consistently captured in the estimation of ABOs from MFH model.

In principle, the WFs calculated from first principles can be used to compute the parameters like hopping, the Hubbard term and onsite energy used in the MFH Hamiltonian. Estimation of BOs and ABOs from such a Hamiltonian would truly represent the exact picture of activation specific to the system as schematically described in Fig.6.10.

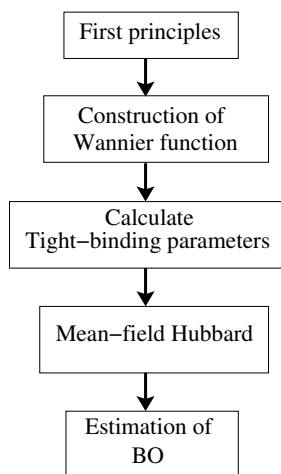


Figure 6.10: Scheme of BO calculation.

6.3.2.4.1 Activation of B in the neighborhood of C@B : As per our scheme of estimation of sub-shell filling and atomic charge based on WCs adopted in our work [sec.2.4.1.1] the shell of neighboring B atoms around C@N[Fig.6.9(c)] has complete sub-shell filling, whereas, at C@B [Fig.6.9(e)], the next nearest B atoms fall short by one electron from completing their sub-shell filling. These B-atoms can also complete sub-shell filling upon adsorption if assisted by charge transfer from the neighborhood. Such possibilities of charge transfer have indeed been suggested recently [24] although have not been conclusively linked to the activation of B-sites. However, we find the exact microscopic pathway of charge transfer to be from C@B to N and N to B. In the process, C@B and N both completed their sub-shell filling, although N loses its charge neutrality. This is a rare occurrence of N to B charge transfer in an attempt to complete sub-shell filling of B. Therefore it is either C@B or the B at next nearest neighborhood can be chemically active. In principle, such activation B in the neighborhood of C@B should be strongest in the immediate shell of B atoms around C@B but should also be possible for further shell of B atoms with decreasing propensity.

With $n_B = n_N$, formation of C=C π -bond [Fig.6.9(f)] completely quenches activation of C and thereby of B atoms in the vicinity as well, due to complete suppression of correlation in the absence of an unpaired electron, which also results into retention of charge neutrality and shell-filling in the rest of hBN. These conclusions are consistent with the energetics[sec.6.3.1] and description of activation based on ABOs[sec.6.3.2.1]. Thus the WFs based picture of activation also suggests active sites exist only at the zigzag edges of Gr-island in hBN made of $n_B \neq n_N$.

6.3.3 Catalytic activity

The active sites(C@N, C@B or B) are expected to chemisorb radicals in general. In this part, we focus on their ability to adsorb O_2 and facilitate their complete reduction which is ORR. Following similar principles, this active sites can also evolve O_2 form H_2O which is known as OER. We study the effectiveness of this active sites in playing the role of catalytic host for ORR and OER in the environment of atomic H as available in acidic medium.

6.3.3.1 Adsorption of O_2

As evident from Fig.6.11 molecular O_2 adsorbs in two configurations, either on a single active C or B or as a bridge on two active C or B atoms, or as a bridge on two active C and/or B atom. Owing to the triplet ground state of O_2 in the gas phase, calculation of its adsorption energy is nontrivial, since the ground states before and after adsorption can have different magnetic moments. Energetics of adsorption of molecular oxygen(O_2) is calculated using Eq.6.2, where the total energetics are estimated within LSDA. The energetics of adsorption of O_2 on a variety of configurations of substitution by C, as summarized in Fig.6.11, is consistent with our expectation of stronger binding on C@B site than on C@N site as per the ABO analysis in sec.6.3.2.1.

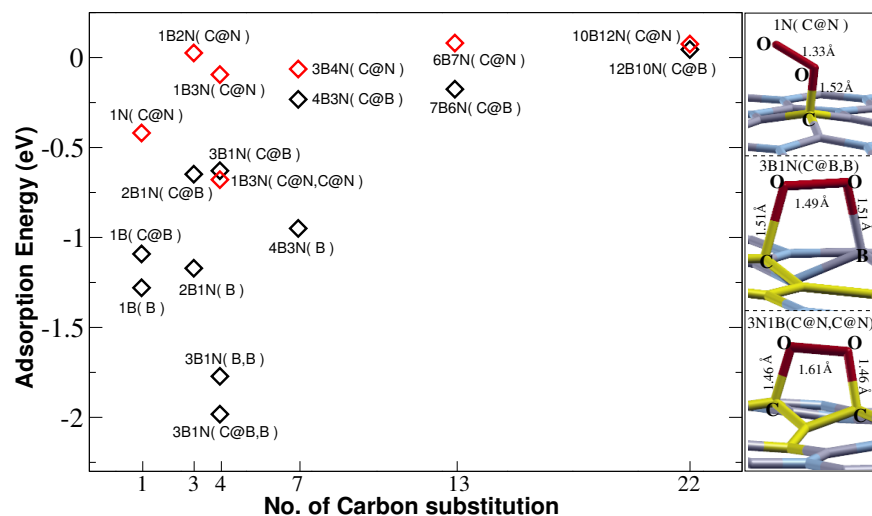


Figure 6.11: Adsorption energy of O_2 for different doping configurations mentioned consistently with Fig. 6.3. A site(s) of adsorption is mentioned in parenthesis. Three classes of O_2 adsorption configurations have shown.

WCs plotted in Fig. 6.12 implies that O_2 adsorbs on active C through a single bond and restores charge neutrality and sub-shell filling of the C doped hBN motif to that of pristine hBN. WC based estimate of charge per atom (0.5e per bonding WC, 1e per atomic WC) suggest chemisorption [Fig. 6.12(a,d)] of O_2 as a dipole with +0.5e charge on the O bonded to the active site and -0.5e on the outer O, in an attempt to achieve complete sub-shell filling. Notably, O_2 has a triplet ground state with O-O single bond and an unpaired electron per atom, implying incomplete sub-shell filling of both O atoms. In adsorbed O_2 , the O-O bond is of order 1.5, consistent with its length of 1.33Å [Fig. 6.11], which is approximately the average length of O-O double and single bonds. O_2 adsorbs in the same configuration on active B [Fig. 6.12(d)], with the corresponding O-O bond being 1.35Å. On the other hand, O_2 adsorbs as neutral bridge with O-O single bond on two active C and/or B or one each of them.

As evident in [Fig. 6.11] the adsorption of O_2 on active B site is stronger than that on C@B implying that upon substitution by C on a single B-site six B-sites around it

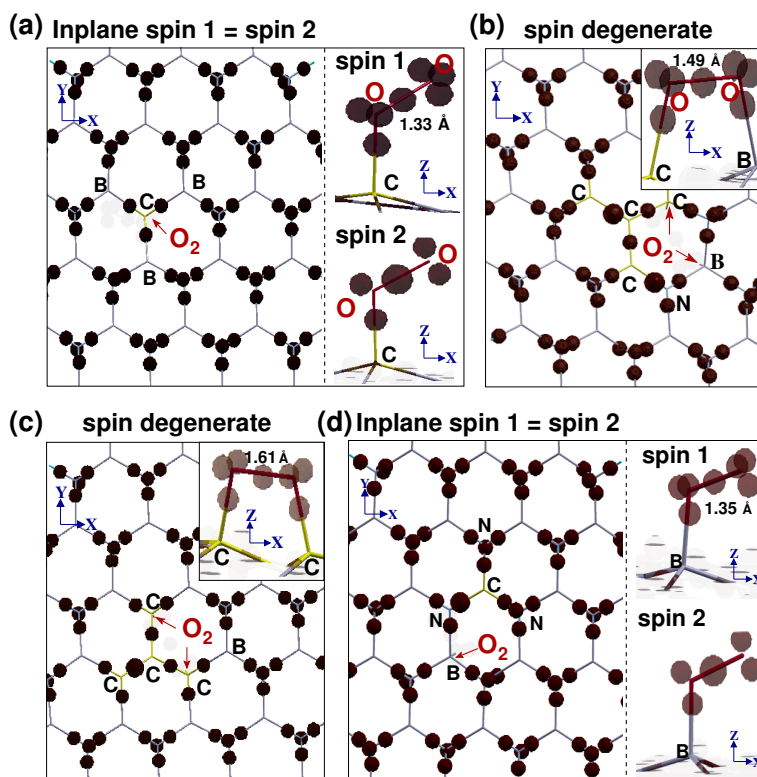


Figure 6.12: In-plane(C doped hBN) and out of plane(associated with O_2) Wannier centers, represented by brown translucent spheres for O_2 adsorbed on: (a)1N(C@N), (b)3B1N(C@B,B), (c)1B3N(C@N,C@N), (d)1B(B). The smaller(bigger) sphere represents one(two) WC(s) each representing one electron.

will become active for adsorption of O_2 , which actually increases the entropy of the process thus opening scopes for lowering of free energy. As also evident in [Fig.6.11], the strength of adsorption of O_2 systematically reduces with increasing size of Gr-island in hBN. Particularly, beyond islands with size of few nm^2 the strength of adsorption of O_2 on C@B and C@N are almost similar as apparent for 22C(12B10N and 10B12N) in Fig.6.11. We will rationalize latter[sec.6.3.3.2] that for workable operating voltages adsorption of O_2 on the cathode should indeed be weak.

6.3.3.2 Oxygen Reduction Reaction(ORR)

With uptake of four H^+ from electrolyte, and four electrons from the lead, which is connected to the anode through external load, complete reduction of O_2 to $2H_2O$ at cathode occurs proceeds in two different pathways depending on the strength of binding of atomic O on active site vis-a-vis the strength of O-O Bond in the adsorbed configuration.

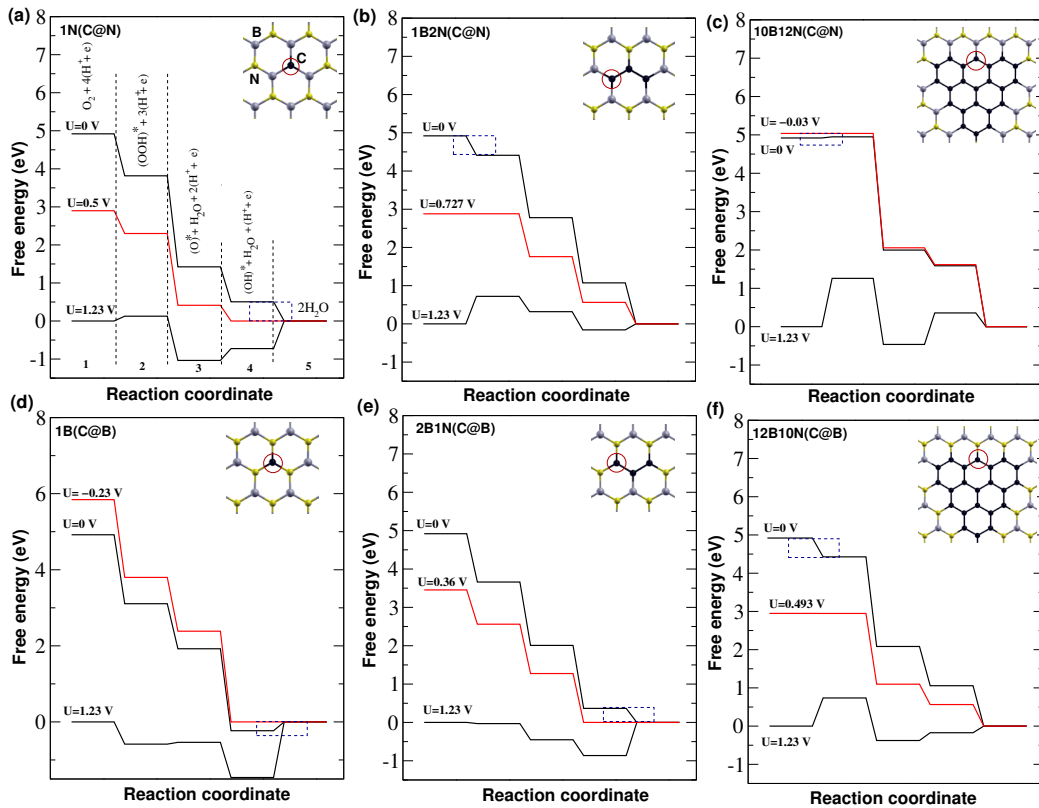
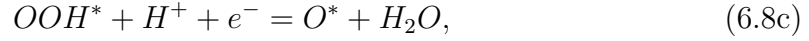


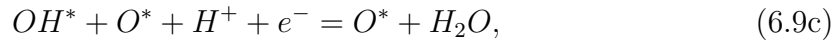
Figure 6.13: Free energy diagram of ORR in acidic condition on different configurations of substitution by C(inset): C@N for (a)1N, (b)1B2N, (c)10B12N and C@B for (d)1B, (e)2B1N, (f)12B10N. Blue boxes pointing out the rate limiting steps and red circle represents the catalytic site. Free energy pathway for maximum operating voltage(U_{ORR}) is shown here in red.

For O_2 adsorbed on active C, whether on a single C atom or on a bridge reduces

through formation of -O-O-H as shown in the following pathway [Eq.6.8a-6.8e].



where ‘*’ denotes the substrate and X^* denotes chemisorbed $X : O_2, OOH, O, OH$. However, if adsorption of O_2 involve an active B site the strong binding of O on B leads to dissociation of O-O bond upon availability of atomic H resulting in two adsorbed OH, which can be simultaneously reduced and released as H_2O following the steps:



Such H assisted complete dissociation of O_2 can be spontaneous if there is no uphill step in free energy along the entire pathway. However, free energy G , calculated as per Eq.6.3 needs to incorporate the contribution from potential energy(U) of electrons at cathode as

$$G(U) = G - neU. \quad (6.10)$$

Notably, U is the potential energy available to drive current through the external load and thus the operating voltage of the fuel cell.

Theoretically, the maximum possible voltage output of any single fuel cell unit is 1.23 V [42], sourced at the free energy available to each of the four electrons upon complete reduction of one O_2 molecule. Thus in the ideal scenario, the cathode potential should be 1.23 V higher than the anode maintained at the standard hydrogen electrode potential by the acidic electrolyte. But inevitably part of the available free energy is required to overcome uphill steps in course of complete reduction of O_2 , implying lower operating voltage than 1.23 V.

With sequential uptake of H^+ and e^- , the number of electrons n decreases from 4 to 0 in course of complete reduction of O_2 . The maximum value of operating voltage (U_{ORR}) for which there will be no uphill step in the entire ORR pathway is thus given by the minima of free energy steps [Fig. 6.13(a-f)] :

$$U_{ORR} = \text{Min} \{ \Delta G_i \}, \quad (6.11)$$

where $\Delta G_i = G_i(0) - G_{i-1}(0)$, i being the reaction coordinate index 2 to 5 as shown in Fig. 6.13(a) and defined above from 6.8b) to 6.8e). The potential which thus remains unavailable to the external load, is the overpotential:

$$\eta_{ORR} = 1.23 - U_{ORR}. \quad (6.12)$$

Therefore overpotential more than 1.23 V would mean a loss of functionality of the fuel cell since an external voltage would be required to complete the reduction process of O_2 .

As apparent from Fig. 6.13(a-f), the height of free energy steps are sensitive to the difference in strength of binding of -OX(-OOH/-O/-OH) in the successive steps.

For example, stronger binding of $-OX_i$ in the i -th step than that of $-OX_{i-1}$ in the $(i-1)$ -th step, would increase magnitude of the free energy step ($G_i(0) - G_{i-1}(0)$). This increases the maximum U allowed for that particular ORR step to remain downhill.

Thus the reaction coordinates 2 to 5 in Fig. 6.13(a), or steps Eq. 6.8b to 6.8d and 6.9b to 6.9d, suggests that ΔG_i is determined by the relative strength of binding of the product with respect to that of the reactant, which has been suggested as a marker of efficiency of catalysis as per Sabatier [43] principle.

As evident from Fig. 6.13(a-c) and Fig. 6.13(d-f) with increasing size of Gr-islands, the rate limiting steps, which determines the overpotential, shifts from the last reaction step, which is desorption of O-H, to the first reaction step which is reduction of O_2 to OOH or (OH + O). However, for from $n_N=1$ to larger N-site rich islands the general moderation of activation as discussed in sec. 6.3.2.1 leads to reduction in the operating voltage from positive to negative value implying overpotential more than 1.23 V. Whereas from $n_B=1$ to larger B-site rich islands the moderation of activation of C@B sites implies evolution of the operating voltage from negative to positive. Therefore as per Sabatier principle, there will be different descriptors for ORR catalysis on isolated substitution ($n_B=n_N$) and for larger Gr-islands.

6.3.3.3 Oxygen Evolution Reaction(OER)

Oxygen evolution reaction is the reverse mechanism of ORR that take place at anode. In OER, evolution of O_2 through oxidation of water in presence of acidic electrolyte

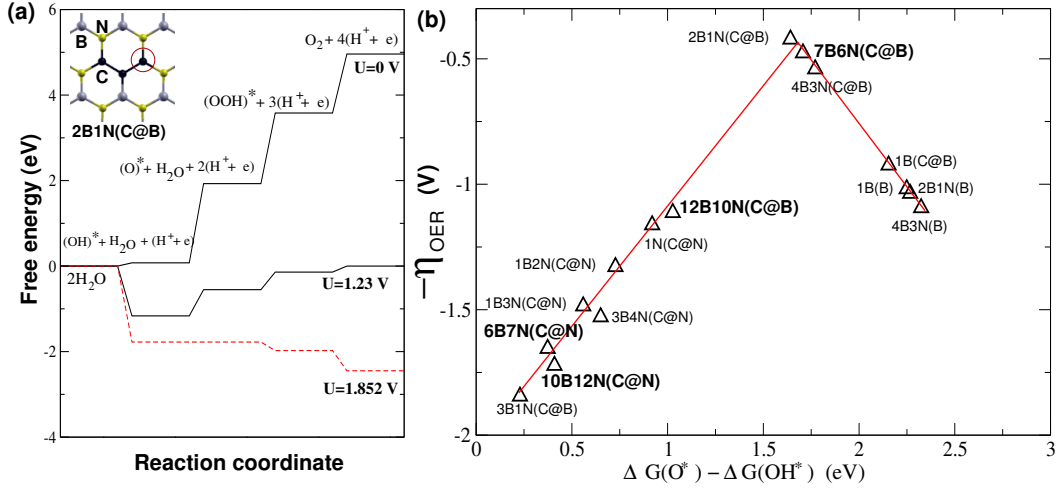
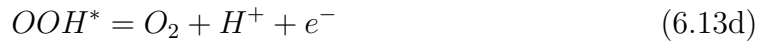
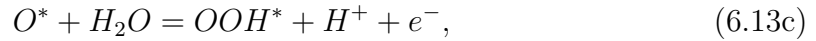
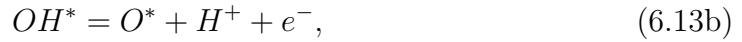
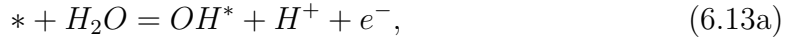


Figure 6.14: (a) Free energy diagram of OER in acidic condition for the configuration with least overpotential and (b) Volcano plot for OER w.r.t descriptor $\Delta G(O^*) - \Delta G(OH^*)$ [44]. Red dotted line in (a) corresponds to optimum operating voltage U and the red circle pointing out the catalytic site. Bigger Gr-islands have been highlighted in bold at plot (b)

proceeds as,



As evident from Eq. 6.13a-6.13d [Fig. 6.14(a)] for OER, conversely we have [45]:

$$U_{OER} = \text{Max} \{ \Delta G_i \} \quad (6.14)$$

and therefore, overpotential for OER

$$\eta_{OER} = U_{OER} - 1.23 \quad (6.15)$$

implying that to drive OER an overpotential is essential. As evident from volcano plot[Fig.6.14(b)] for OER, where the second step[Eq.6.13c] is consistently the rate limiting for Gr-islands of different sizes, there is a clear trend that active C@B sites are strongly preferred up to an optimal size of Gr-islands. Therefore for OER catalysis, smaller Gr-islands are preferred over bigger islands. This is expected as the stronger binding of -OX intermediates, will make it easier to cleave the O-H bond of water and thus lesser will be the required overpotential. Fig.6.14(b) also imply that the relative binding of -OH over that of -O is preferred to be of about 1.5 eV, in order to minimize the overpotential value.

6.3.3.4 Non-magnetic graphene island

In previous sections[sec.6.3.3.2, 6.3.3.3] all discussions are based on magnetic Gr-islands of various sizes. Alongside, the non-magnetic Gr-islands, covering an equal number of B and N-sites are also energetically favorable[Fig.6.3]. We have analyzed the catalytic activity of two such Gr-islands (6C and 16C) embedded within hBN. As evident from Fig.6.4(c), all the sites irrespective of C@B or C@N for both 6C and 16C have comparable activation.

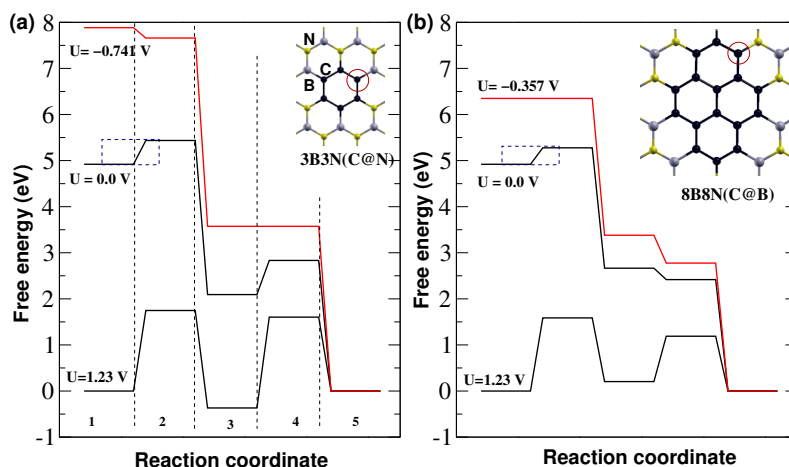


Figure 6.15: Free energy diagram of ORR in acidic condition on different non-magnetic configurations of substitution by C(inset): C@N for (a)3B3N(C@N), (b)8B8N(C@B). Dotted boxes pointing out the rate limiting steps and red circle represents the catalytic site. Free energy pathway for maximum operating voltage is shown here in red.

The study of ORR reaction pathway in these Gr-islands shows an uphill step at the first reaction step[Eq.6.8b][Fig.6.15(a,b)]. Therefore the corresponding operating voltage becomes negative, which implies high overpotential and its non-effectiveness as a cathode material. Similarly for OER[sec.6.3.3.3] overpotential is also high for these non-magnetic Gr-islands.

This systematic analysis of all representative configurations considering magnetic as well as non-magnetic Gr-islands, thus suggests magnetic Gr-islands embedded within hBN as a suitable candidate for ORR and OER, particularly the B-site rich large Gr-islands for ORR and smaller B-site rich Gr-islands for OER, which is clearly evident from Fig.6.16.

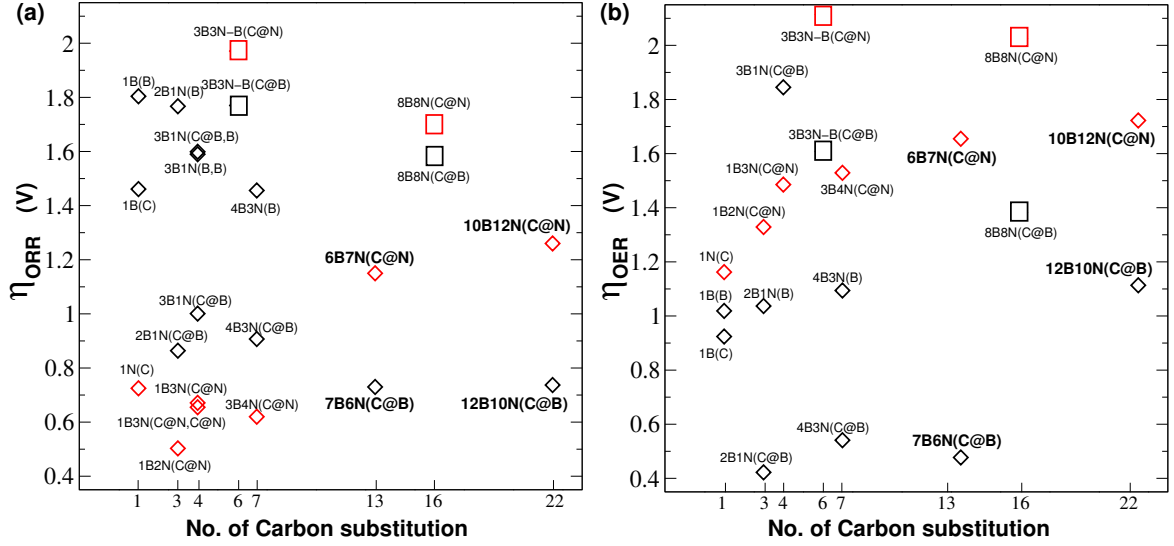


Figure 6.16: Overpotential of all C-substituted hBN configurations (a) for ORR and (b) for OER. For magnetic Gr-islands, \blacklozenge and \blacklozenge represents the N-site rich and B-site rich configurations with catalytic site as mentioned within the parenthesis. For non-magnetic islands, \square and \square respectively represents C@N and C@B catalytic site. Bigger magnetic islands are highlighted in bold.

6.3.4 Transferability of electrons

The other important aspect, which is vital for effective electrocatalysis is transferability of electrons from the leads to the active sites. This is anticipated to be hindered in hBN based systems due to its insulating nature. A possibility to overcome this problem emerges, as we find that if the active magnetic Gr-islands form H-K hybrid super-lattices, then they can be a half-metal or a metal [sec. 5.5]. For example in Fig. 6.17(a) we have shown H-K super-lattice, where honeycomb lattice is formed by 13C island and kagome lattice is formed by single C substitution $n_B=1$. Without intermediate C, 13C islands show anti-ferromagnetic order with weak exchange interaction between the islands. Substitution by C-atom between two neighboring 13C islands open a scope for p_z electron of the magnetic island in the honeycomb lattice to become itinerant and allow transport of electrons as evident from DOS of

Fig.6.17(b) in room temperature. These mechanisms have been described in detail in Chapter 5 [46].

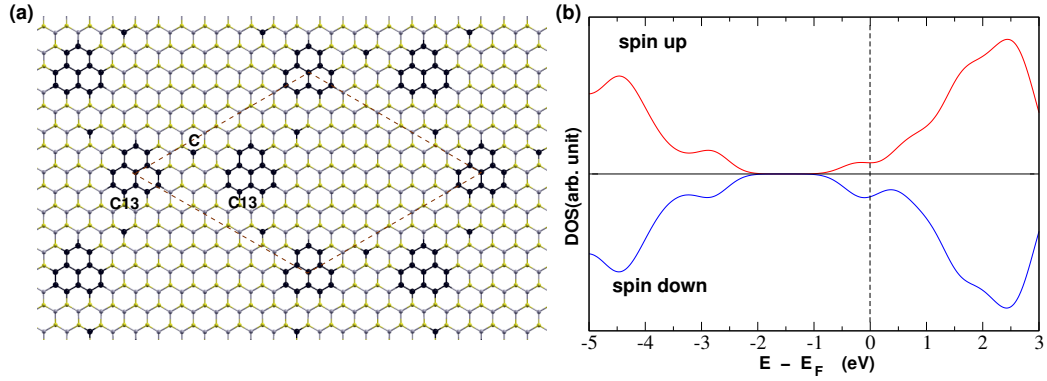


Figure 6.17: (a) Graphene-hBN hexagonal-Kagome hybrid system with ^{13}C Gr-island at hexagonal site and single $\text{C}@B$ at Kagome sites. Dotted line represents the hexagonal-Kagome supercell, (b) spin-polarized DOS for the same.

Bibliography

- [1] V. Georgakilas *et al.*, *Chem. Rev*, 112, (2012).
- [2] H. T. Wang, *Nano Lett*, 12, (2012).
- [3] T. Sainsbury *et al.*, *J. Am. Chem. Soc*, 134, (2012).
- [4] J. Yin *et al.*, *small*, 12(22), (2016).
- [5] X. Wei, M.-S. Wang, Y. Bando, D. Golberg, *ACS Nano*, 5, (2011).
- [6] H. Wang, T. Maiyalagan, X. Wang, *ACS Catal.*, 2, (2012).
- [7] Y. Zheng, Y. Jiao, L. Ge, M. Jaroniec, S. Z. Qiao, *Angew. Chem.*, 125, (2013).
- [8] S. Navalon, A. Dhakshinamoorthy, M. Alvaro, H. Garcia, H. *Chem. Rev*, 114(12), (2014).
- [9] G. Elumalai, H. Noguchi, K. Uosaki, K. *Phys. Chem. Chem. Phys*, 16, (2014).
- [10] Z. -H. Sheng, H. -L. Gao, W. -J Bao, F. -B. Wang, X. Xia, *J. Mater. Chem*, 22, (2012).
- [11] Y. Jiao, Y. Zheng, M. Jaroniec, S.Z. Qiao *J. Am. Chem. Soc.*, 136, (2014).
- [12] M. Favaro, *ACS Catal.*, 5, (2015).
- [13] J. Bhattacharjee, *J. Phys. Chem. Lett.*, 6(9), (2015).

- [14] L. Yang *et al.*, *Angew. Chem*, 123, (2011).
- [15] Y. Zhao *et al.*, *J. Am. Chem. Soc*, 135, (2013).
- [16] C. Zhu, S. Dong, *Nanoscale*, 5, (2013).
- [17] S. Wang *et al.*, *Angew. Chem., Int. Ed*, 51, (2012).
- [18] A. Goriachko *et al.*, *Langmuir*, 23, (2007).
- [19] L. Ci *et al.*, *Nature Mat.*, 9, (2010).
- [20] G. H. Han *et al.*, *ACS Nano*, 7, (2013).
- [21] Z. Liu *et al.*, *Nature Nanotech.*, 8, (2013).
- [22] G. Kim *et al.*, *Nano Lett.*, 15(7), (2015).
- [23] J. Zhao, Z. Chen, *J. Phys. Chem. C*, 119 (47), (2015).
- [24] M. Gao, M. Adachi, A. Lyalin, T. Taketsugu, *J.Phys.Chem.C*, 120 (29), (2016).
- [25] J. P. Perdew, K. Burke, M. Ernzerhof, *Phys. Rev. Lett*, 77, (1996).
- [26] N. Berseneva, A. V. Krasheninnikov, R. M. Nieminen, *Phys. Rev. Lett* 107, 035501, (2011).
- [27] J. K. Nørskov, J. Rossmeisl, A. Logadottir, L. Lindqvist, J. R. Kitchin, T. Bligaard, H. J ónsson, *J.Phys.Chem.B*, 108, (2004).
- [28] M. W. Chase Jr., NIST-JANAF Thermochemical Tables, 4th ed., Monograph 9, *J.Phys.Chem*, Ref.Data; NIST: Gaithersburg, MD,(1998).
- [29] I. Mayer, *J Comput Chem*, 28, (2007).
- [30] C. A. Coulson, *Proc, Roy. Soc. (London)* A169, (1938).

- [31] R. Hoffmann, *J. Chem. Phys.*, 39, (1963).
- [32] R. Pariser, R. G. Parr, *J. Chem. Phys.* 21, (1953).
- [33] I. Mayer, *Chem. Phys. Lett.*, 97, (1983).
- [34] Thomas A. Manz, *RSC Adv.*, 7, 45552, (2017).
- [35] R. S. Mulliken, *J. Chem. Phys.* 23, (1955).
- [36] D. R. Armstrong, P. C. Perkins, J. J. P. Stewart, *J. Chem. Soc. (Dalton)*, 838, (1973).
- [37] Padeleimon Karafiloglou and Katerina Kyriakidou, *International Journal of Quantum Chemistry*, 114, (2014).
- [38] Hiroshi Suzuki, *Electronic Absorption Spectra and Geometry of Organic Molecules: An Application of Molecular Orbital Theory*, Academic Press,(1967).
- [39] S. Tang *et al.*, *Scientific Reports* 3, 2666, (2013).
- [40] M. Kim *et al.*, *Nano Lett.* 13(3), (2013).
- [41] Q. Sun, C. Sun, A. Du, S. Dou, Z. Li, *Nanoscale*, 8, (2016).
- [42] J. K. Nørskov *et al.*, *J.Phys.Chem.B*, 108, (2004).
- [43] T. Bligaarda *et al.*, *Journal of Catalysis*, 224(1) ,(2004).
- [44] M. Li *et al.*, *Journal of Catalysis*, 314, (2014).
- [45] I. C. Man *et al.*, *Chem Cat Chem*, 3, (2011).
- [46] Rita Maji, Joydeep Bhattacharjee arXiv:1809.08270.

Conclusions

The central theme of this thesis has been to systematically study the interplay of spin and charge degrees of freedom of itinerant $2p_z$ electrons. These studies have led to a synergistic understanding of magnetism as well as chemical activation and catalysis of three coordinated systems made of 2p-block elements. The key ingredient has been the tuning of competing interactions in these systems through reversible and irreversible inhomogeneity.

In the first part, computational studies of inhomogeneously biased graphene nanoribbons have been presented. There the main observation was the emergence of localization driven nearest neighbor(n-n) ferromagnetic(FM) order at weak coupling limit in graphene nanoribbons irrespective of edge configurations. A comprehensive analysis from mean-field Hubbard model and first-principles using density functional theory(DFT) explain this bias controlled n-n FM ordering as a generic property of inhomogeneously biased bipartite systems. The key mechanism is to allow localization of electrons in positively biased region while allowing minimal increase in Coulomb potential and kinetic energy leading to different degrees of localization of electrons with opposite spins primarily at positively biased sites. The consequent n-n FM order lift spin degeneracy which leads to ferromagnetic metal or half-metallic phases. In zig-zag nanoribbons(ZGNRs), the contest of inherent inter edge anti-ferromagnetic(AFM) ordering and n-n FM ordering due to inhomogeneous biasing,

leads to systematic emergence of half-metallic window across Fermi energy. This work thus demonstrates the possibility of bias controlled emergence of n-n ferromagnetism and spin polarized transport of electrons in layered bipartite systems.

In the next chapter, the influence of chemical inhomogeneity in hybrid structures of graphene and hBN in tuning physical properties primarily magnetism has been investigated. The spatial separation of back transferred electrons of opposite spins at B and N sites in the vicinity of local moments due to magnetic graphene islands is found to be the primary mechanism of propagation of anti-ferromagnetic order between local magnetic moments embedded in hBN. Such a mechanism proposes spin dependent hopping as a key parameter in exploring the correct magnetic ground states within a tight-binding framework. Magnetic ordering between two local moments can be switched from anti-ferromagnetic to ferromagnetic if the pathway of anti-ferromagnetic ordering is interjected by a third moment of arbitrary strength. Accordingly, inter-penetrating hybrid kagome super-lattices of magnetic graphene islands in hBN have been proposed as a metal free route of ferromagnetic semiconductor and half-metal at room temperature.

In the sixth chapter we have investigated chemical activation and catalytic efficiency of graphene islands in hBN in correlation with their magnetic properties. We have introduced average bond order(ABO) of an atom as a measure of their chemical activation which can be computed based on localized orbitals obtained from first principles. The catalytic efficiency of active sites in these hybrid systems has been demonstrated in the light of oxygen reduction and oxygen evolution reactions which are central to acid based fuel cells. Our results reveal the effectiveness of graphene and hBN hybrid systems with practicably large graphene islands to be a suitable candidate for cathodes free of precious metals.

In conclusion, we hope our work will sharpen the focus on graphene and hBN

hybrid systems in particular and heterostructure made of 2p block elements in general for application in active as well as spintronic devices in one hand and filtration and catalysis on the other hand both of which are suitable for futuristic applications from the point of view of managing electronic waste and securing non-fossil energy resources.

Future Scope

In this chapter, I describe future scope of my thesis work, which are essentially extension of works reported in the different chapters of the thesis. Some of these extension works are already in progress which I present below.

Extension of work presented in Chapter 4 :

1. Space charge in presence of inhomogeneous bias

We recall that in Fig.4.7(b)[sec.4.2.3] the bands near the Fermi energy, which are marked by the green dots, as also shown in Fig1(a) are parabolic in nature implying presence of nearly free electrons in one dimension. Spin density profile[Fig1(b,c)] at a particular sawtooth potential [sec.4.2.3] shows accumulation of space charge above and below the biased region. As evident in Fig1(c),

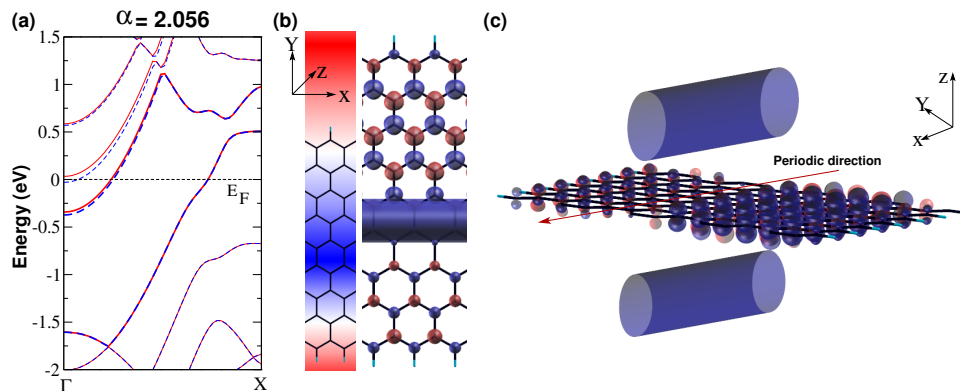


Fig1 : (a)band structure, (b)applied sawtooth potential profile and spin density, (c)space charge distribution across the zigzag ribbon in out of plane view.

the space charge is spin polarized within a range of sawtooth potential amplitude. Spin polarization of space charge coincide with the emergence of nearest neighbor(n-n) ferromagnetic(FM) order, which lead to similar spin polarization of zigzag ribbon edges[Fig1(b)] as discussed in Chapter 4. In Chapter 4, we have only described the evolution of in-plane spin polarization as a function of bias voltage. In the immediate future, we plan to explore in details the possibility of manipulation of space charge in facilitating spin-polarized conduction of electrons. We envisage that the bias induced space charge will allow free electron like transport with confinement in one or two directions.

2. Localization induced tunable magnetism in flakes and sheets of graphene

The emergence of n-n FM order and its impact on transport properties of graphene nanoribbon motivates us to explore the effect of inhomogeneous bias on finite graphene segments, known as graphene nanoflakes and 2D graphene sheet. Notably, in Chapter 4 the emergence of n-n FM order in graphene nanoribbon has been explored. Finite magnetic moment in this nanoflakes is hosted by sub-lattice asymmetry. Some results for hexagonal and triangular graphene nanoflakes have been discussed here. We have considered two types of bias coverage, one in which the biased site covers equal number of sites from two sub-lattices, defined as non-magnetic gate, and another, in which the biased site covers unequal number of sites from two sub-lattices, defined as magnetic gate. We have plotted total and absolute magnetization as a function of U and gate voltage V_g .

2.1. Hexagonal graphene nanoflake

First, we consider magnetic[Fig2(a)] and non-magnetic[Fig2(c)] bias within a hexagonal graphene nanoflake. Magnetic moment of hexagonal graphene

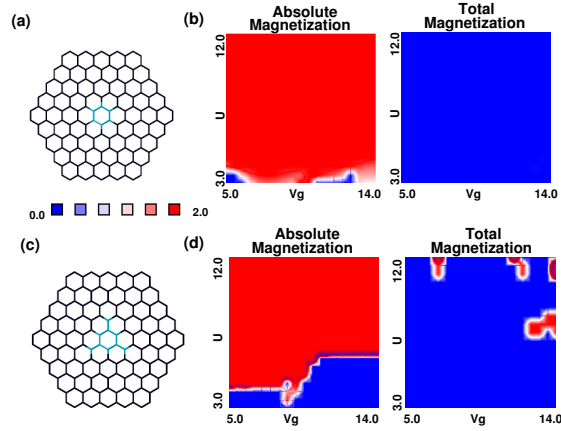


Fig2 : Representation of bias coverage on graphene nanoflake and variation of total magnetization and absolute magnetization w.r.t onsite Coulomb repulsion U and applied gate voltage V_g in hexagonal graphene nanoflake for (a,b)6-site and (c,d)9-site bias coverage. Bias coverage has been shown in blue color within the hexagonal flake.

nanoflake is zero since it is constituted with equal number of sites from two sub-lattices. As evident from variation of total magnetization [Fig.2(b,d)] the non-magnetic bias coverage does not lead to n-n FM order [Fig3(a)] within weak to moderate coupling limit, whereas with magnetic gate coverage n-n FM order does emerge at a high V_g , before complete quenching of magnetism as also implied in Fig3(b).

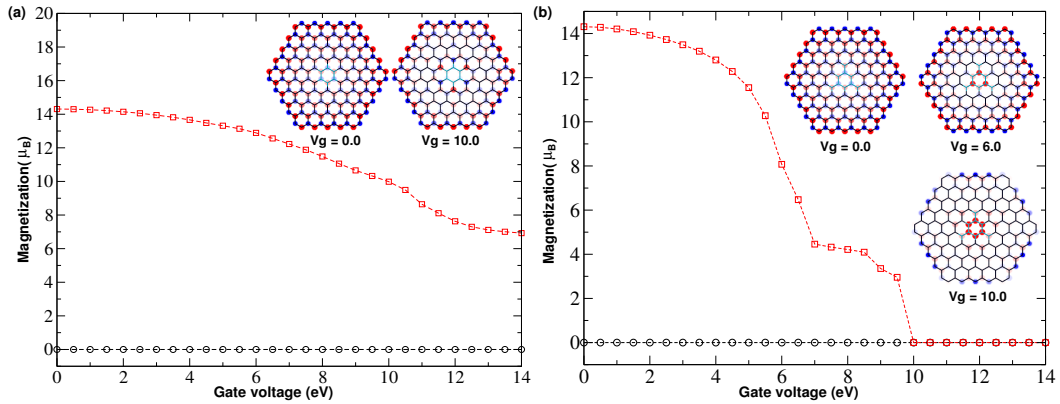


Fig3 : Variation of total (black circle) and absolute (red square) magnetization w.r.t gate voltage V_g for (a) non-magnetic, and (b) magnetic bias coverage at $U=5.0$ eV. Corresponding spin density has been shown in the inset.

2.2. Triangular graphene nanoflake

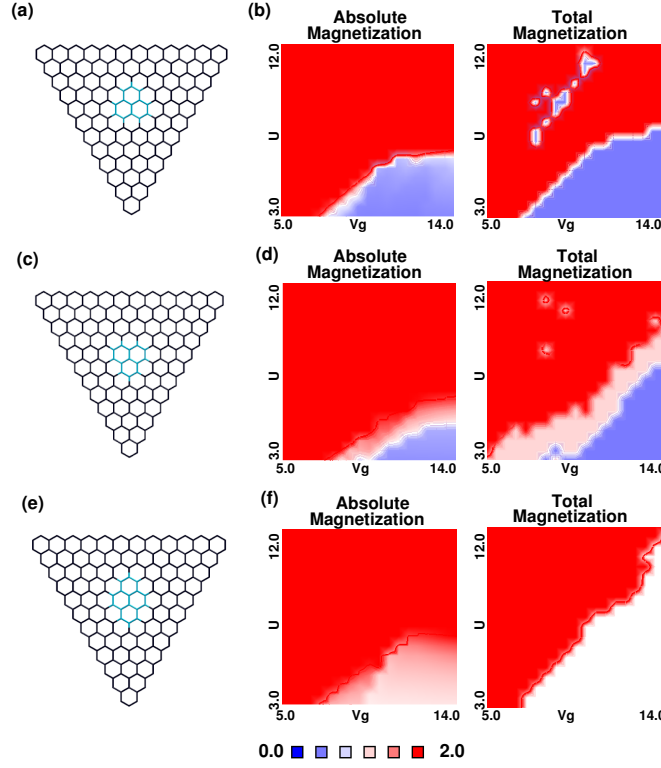


Fig4 :Representation of bias coverage on graphene nanoflake and variation of total magnetization and absolute magnetization w.r.t onsite Coulomb repulsion U and applied gate voltage V_g in triangular graphene nanoflake for (a,b)13-site up-triangle, (c,d)13-site down triangle and (e,f)16-site non-magnetic bias coverage. Bias coverage has been highlighted in blue color within the triangular flake.

Next, we consider magnetic and non-magnetic gate in triangular graphene nanoflake. Magnetic moment of this triangular nanoflake is $11\mu_B$ due to difference in number of sites from two sub-lattices. As Fig4(a-f) suggests, tunability of magnetization for this triangular graphene nanoflake is indeed possible through both, non-magnetic and magnetic bias coverage and is sensitive to the orientation of the biased site vis-a-vis that of the flakes. With increasing V_g , the interplay between inherent anti-ferromagnetic(AFM) ordering in magnetic triangular nanoflake and n-n

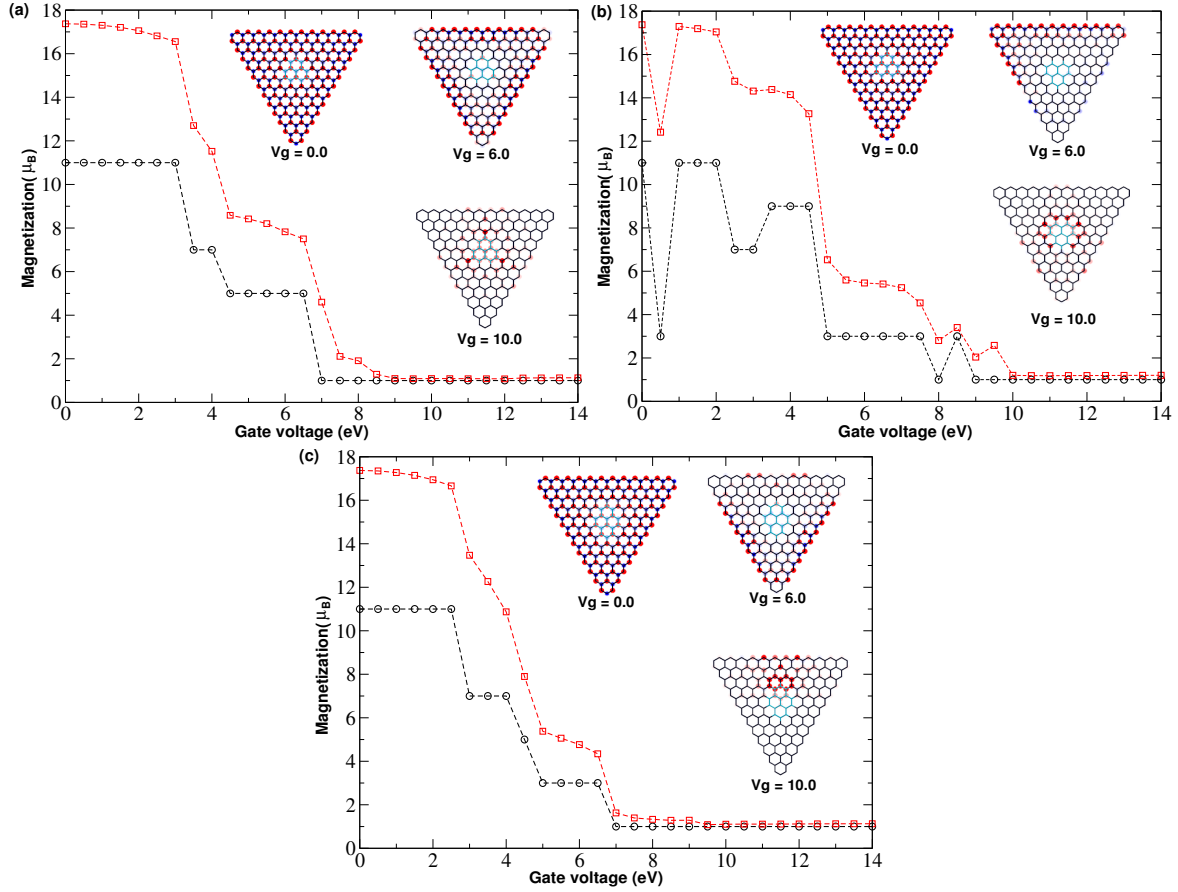


Fig5 : Variation of total(black circle) and absolute(red square) magnetization w.r.t gate voltage V_g for (a,b)13-site up-triangle, (c,d)13-site down triangle and (e,f)16-site non-magnetic bias coverage at $U=3.0$ eV. Corresponding spin density has been shown in the inset.

FM ordering in the biased region leading to systematic manipulation of magnetization[Fig5(a-c)].

2.3. Graphene sheet

We consider application of bias over a finite region in a graphene sheet in order to study the evolution of magnetism in presence of bias without the interference of edges. We next explore the possibility to induce interacting magnetic islands through application of bias in two regions in proximity within graphene sheet. As depicted in Fig.6(a) and Fig.7(a)

n-n FM order is induced within a single biased region even at weak coupling [Fig7(a,b)] above a threshold value of V_g . With two biased region Fig6(c-f) and Fig7(b,c) the magnetic ordering between two biased regions is function of their mutual orientation. If the two regions cover more site from different sub-lattices, then their interaction will be always of anti-ferromagnetic or ferrimagnetic ordering [Fig7(c) and Fig6(e,f)] depending on their relative sizes. However, if both the islands covers more of the same sub-lattice, then it is possible to have FM ordering between the two islands[Fig7(b), Fig6(c,d)] This systematic manipulation of magne-

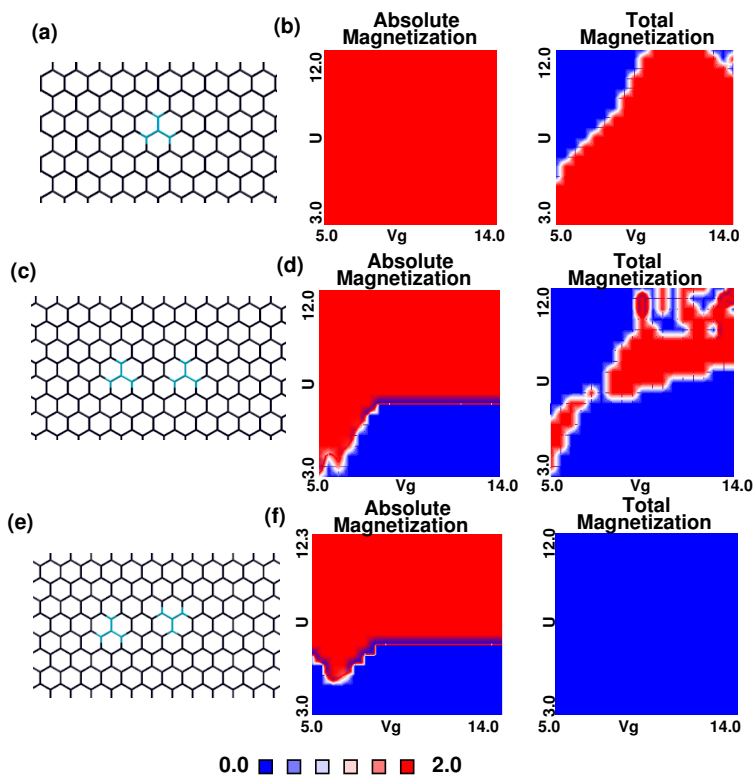


Fig6 : Representation of bias coverage on graphene supercell and variation of total magnetization and absolute magnetization w.r.t onsite Coulomb repulsion U and applied gate voltage V_g for (a,b) 4-site, (c,d) two 4-site symmetric triangle and (e,f) two 4-site asymmetric triangle coverage for bias sites. Bias coverage has been shown in blue color within the graphene supercell.

tization also holds within periodic geometry of gate coverage, as evident

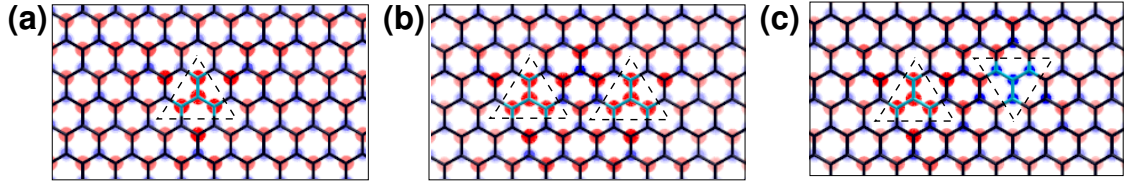


Fig7 : Spin density for (a) single 4-site bias coverage, and two 4-site bias coverage with (b)symmetric ,(c) asymmetric configurations. Bias coverage has been pointed out with dotted triangle at $V_g=6.0$ eV and $U=6.0$ eV

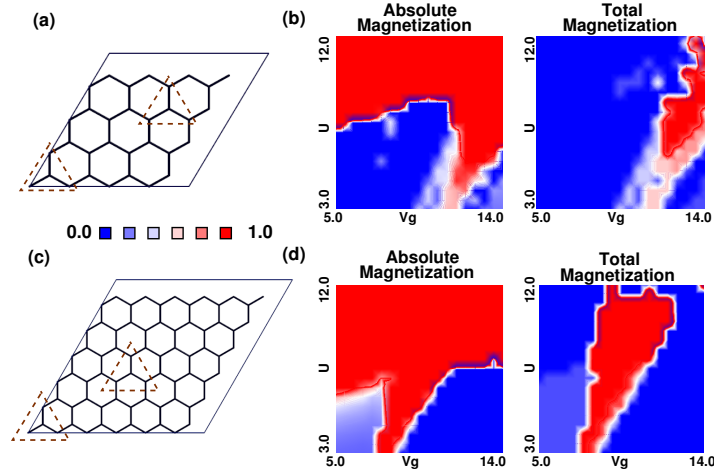


Fig8 : Representation of bias coverage on graphene sheet and variation of total magnetization and absolute magnetization w.r.t onsite Coulomb repulsion U and applied gate voltage V_g for (a,b) 4×4 , (c,d) 6×6 graphene supercell. Dotted triangle corresponds to the bias sites.

in[Fig8(a,b), Fig8(c,d)], which suggests hexagonal lattice of ferromagnetically ordered gated islands at weak coupling[Fig9]. Therefore, by designing arrays of triangular or similar gated regions each with unequal coverage of the two sub-lattices, it is indeed possible to induce controlled magnetism in graphene through application of bias. More detail calculations of transport properties and magnetism in super-lattices of gated graphene are in progress.

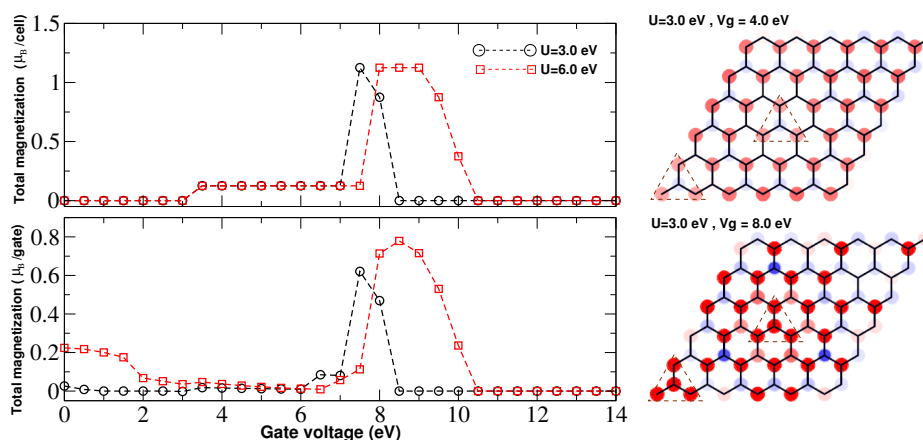


Fig9 : Variation of total magnetization w.r.t gate voltage V_g and spin density of graphene sheet in presence of bias.

Extension of work presented in Chapter 6 :

3. Electrocatalysis in boron doped graphene

In the series of low dimensional materials based metal free electrodes, functionalized graphene have an important impact like graphene-hexagonal boron nitride hybrids as discussed in this thesis. Recently the synthesis stability [1, 2] of boron(B) substituted graphene makes it more important towards understanding its chemical activity. First principles analysis predicts that multi boron substitution within close proximity is energetically favorable in comparison with isolated substitution. The local electronic distribution due to hole doping and the mechanical strain induced from inequivalent C-C and C-B bond lengths facilitates its activation. On the realm of electrocatalytic activity, primarily for oxygen reduction and evolution reaction (ORR, OER) we have done some preliminary analysis. Different degree of hydrogen adsorption [3] in B substituted graphene also motivate us to investigate the mechanism of hydrogen evolution reaction (HER) in different B doped configurations.

4. Reduction of NO_x through hydrogenation

As a follow up of our work on ORR catalysis of C-doped hBN we envisage the effectiveness of the same platform for filtration of NO_x . We have also looked for boron/nitrogen doped graphene as NO_x filter. As evident from reaction pathway simulated from first principles [Fig10]] experimentally accessible tri-boron doped graphene[Fig10(a)] can possibly adsorb and reduce NO to NH_3 in an acidic environment. Similar functionality has been shown [Fig10(b)] for carbon doped hBN. Detail calculation and analysis are envisaged in near future.

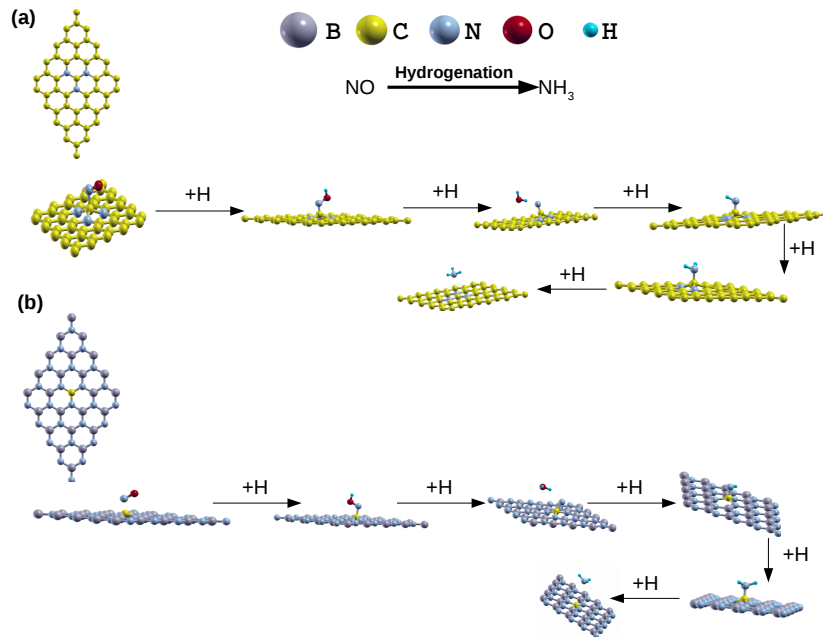


Fig10 : Production of NH_3 through hydrogenation of NO at two different catalytic surface (a)nitrogen doped graphene and (b) carbon doped hexagonal boron nitride following the pathway : $sub(*) + NO \rightarrow NO^* \rightarrow (NOH)^* \rightarrow N^* + H_2O \rightarrow (NH)^* \rightarrow (NHH)^* \rightarrow * + NH_3$.

Bibliography

- [1] J. Gebhardt *et. al* Physical Review B 87, 155437 (2013).
- [2] Ruitao Lv *et. al* PNAS, 112(47), 14527-14532, (2015).
- [3] R H Miwa, T B Martins and A Fazio, Nanotechnology, 19,15, (2008).